Universidade de Aveiro Departamento de Química
2021

Márcio Miguel da Silva Soares

Nº 84232

Modelação molecular do reconhecimento e transporte transmembranar de cloreto por recetores sintéticos derivados de hidrazona

Molecular modelling of chloride recognition and transmembrane transport by hydrazone-based synthetic receptors

Dissertação

2020/2021

Universidade de Aveiro Departamento de Química
2021

Márcio Miguel da Silva Soares

Nº 84232

Modelação molecular do reconhecimento e transporte transmembranar de cloreto por recetores sintéticos derivados de hidrazona

Molecular modelling of chloride recognition and transmembrane transport by hydrazone-based synthetic receptors

Dissertação apresentada à Universidade de Aveiro para cumprimento dos requisitos necessários à obtenção do grau de Mestre em Bioquímica Clínica, realizada sob a orientação científica do Doutor Vítor Manuel Sousa Félix, Professor Associado com Agregação no Departamento de Química da Universidade de Aveiro, e do Doutor Igor Oliveira Marques, investigador no grupo de Modelação Molecular e Biofísica Computacional da Universidade de Aveiro.

Dissertação

2020/2021

o júri

presidente

Professor Doutor Brian James Goodfellow
professor assistente, Universidade de Aveiro

Professor Doutor Paulo José Garcia de Lemos Trigueiros de Martel
professor assistente, Universidade do Algarve

Professor Doutor Vítor Manuel Sousa Félix
professor associado com agregação, Universidade de Aveiro

agradecimentos

Ao Professor Vítor Félix, por todo o apoio, orientação e disponibilidade demonstrada, assim como pela confiança depositada em mim ao longo deste período. A sua motivação, atenção e cumplicidade foram fundamentais. Os meus mais sinceros agradecimentos.

Ao meu coorientador Doutor Igor Marques, pela infindável paciência que teve comigo, pela capacidade de criar um ambiente de trabalho como nenhum outro, e por me ensinar tudo o que sei hoje da melhor forma possível. Um gigante obrigado de um poeta, por este ano indescritível, com uma orientação inesquecível.

To Dr. Hennie Valkenier from Université Libre de Bruxelles (ULB), Engineering of Molecular NanoSystems, Ecole Polytechnique de Bruxelles, Avenue F.D. Roosevelt 50, CP165/64, B-1050 Brussels, Belgium, for providing the experimental data that made this work possible.

palavras-chave

canalopatias, fibrose quística, recetores sintéticos, transporte transmembranar de aniões, simulações de dinâmica molecular, modelação molecular, reconhecimento de aniões

resumo

O transporte de espécies iónicas através de membranas biológicas, frequentemente mediado por um conjunto complexo proteínas, é crucial em inúmeros processos fisiológicos. Posto isto, qualquer defeito nesta complexa cascata celular está associado a diversas canalopatias, como a fibrose quística, caracterizada pelo transporte deficiente de cloreto através do canal CFTR. Atualmente, o tratamento destas doenças foca-se principalmente na atenuação dos seus sintomas, fomentando a necessidade de terapias alternativas, como as terapias de substituição de canal No entanto, o design destes fármacos ainda não é inteiramente compreendido, uma vez que depende de um delicado equilíbrio entre a afinidade de ligação do transportador e a sua lipofilia.

Este trabalho estudou o impacto da adição de um grupo funcional em transportadores aniónicos já caracterizados, com unidades de ligação comuns como N−Hs ácidos (ureias, tioureias ou esquaramidas). Assim sendo, uma família de tioureias funcionalizada com grupos acilhidrazona e derivados foi minuciosamente estudada experimental e computacionalmente. Os estudos teóricos reportados neste trabalho consistiram em cálculos quânticos e simulações de dinâmica molecular baseadas em campos de força clássicos.

As análises ao transporte de cloreto sugerem que uma unidade de ligação adicional se traduz num efeito prejudicial na capacidade de transporte dos recetores derivados de tioureias, uma vez que interações adicionais entre a unidade de ligação secundária e os fosfolípidos da membrana impedem o transporte de aniões. Esta hipótese é suportada pelo estudo das orientações dos transportadores na membrana, bem como pelas suas interações, como observado nas simulações de dinâmica molecular.

keywords

channelopathies, cystic fibrosis, synthetic receptors, anion transmembrane transport, molecular dynamics simulations, molecular modelling, anion recognition.

abstract

The transport of ionic species across biological membranes, often mediated by embedded proteins, is vital for numerous biological processes. The slightest malfunction on this complex cellular cascade is associated with several channelopathies, such as cystic fibrosis, characterised by a deficient chloride transport through the cystic fibrosis transmembrane conductance regulator (CFTR) protein channel. Current treatments mainly focus on attenuating the diseases' symptoms, instigating the need for alternative therapies, such as channel replacement therapies (CRTs), based on the development of synthetic receptors. However, the design of these small drug-like molecules is still not fully understood, as it depends on a perfect balance between the transporter's binding affinity and lipophilicity.

This work aimed to obtain theoretical insights into the anion chloride recognition and transport properties of thiourea-based acylhydrazones. As such, a family of thioureas functionalized with acylhydrazones and related functional groups undergone thorough experimental and computational studies. The receptors' affinity for chloride was evaluated by DFT calculations while the interaction and the passive diffusion of receptors and their chloride complexes were investigated through molecular dynamics (MD) simulations based on classical force fields.

The experimental chloride transport studies suggest that the additional binding motif has a detrimental effect of the transport ability of the thiourea-based receptors, as additional interactions between the secondary binding unit and the membrane phospholipids inhibit the anion transport. This hypothesis is strongly supported by the orientation of the transporters in the membrane and respective interactions, as observed MD simulations.

Index

INDEX **1**

FIGURES INDEX **2**

TABLES INDEX **4**

SCHEMES INDEX **5**

ABBREVIATIONS **6**

CHAPTER I. **8**

INTRODUCTION 8

I.1. Biological membrane *9*

I.1.1. Transport across the membrane *10*

I.2. Cystic Fibrosis *12*

I.2.1. Cystic Fibrosis Transmembrane conductance Regulator (CFTR) *13*

I.2.2. Therapeutic Approaches *13*

I.2.3. Synthetic Ionophores *14*

I.3. Molecular Dynamics *21*

I.3.1. Enhanced Sampling techniques *26*

I.3.2. Umbrella Sampling *27*

I.3.2.1. Variational Free Energy Profile *28*

I.3.3. MD simulation of phospholipid bilayers *28*

CHAPTER II. **32**

HYDRAZONE-BASED MOLECULES AS ANION RECEPTORS: MOLECULAR MODELLING BY DFT CALCULATIONS 32

II.1. Introduction *33*

II.2. Methods *36*

II.3. Results and Discussion *37*

II.4. Conclusions *45*

CHAPTER III. **46**

PASSIVE DIFFUSION OF HYDRAZONE-BASED RECEPTORS ACROSS PHOSPHOLIPID BILAYERS: A MOLECULAR DYNAMICS SIMULATION INVESTIGATION 46

III.1. Introduction *47*

III.2. Methods *48*

III.2.1. X-n2-ns-X reparameterization *48*

III.2.2. Membrane MD simulations *51*

III.2.3. MM interaction energies *53*

III.2.4. Umbrella Sampling MD simulations *54*

III.3. Results and Discussion *55*

III.3.1. Diffusion of the transporters within the membrane *55*

III.3.2. Energetic analysis *62*

III.3.3. Structural impact on the bilayer *64*

III.3.4. Constrained MD simulations *66*

III.4. Conclusions *73*

CHAPTER IV. **74**

CONCLUSIONS & FUTURE WORK 74

IV.1. Conclusions *74*

IV.2. Future Work *76*

REFERENCES **77**

APPENDIX **85**

Figures Index

Figure I-1. Schematic illustration of the biological bilayer, with the phospholipids represented in yellow, a peripheric protein in blue, an integral protein in green, a peripheric glycoprotein in orange and its carbohydrate moiety in red. Resources from: Servier Medical Art by Servier. 9
Figure I-2. Schematic representation of the transport mechanisms associated with protein membranes. Resources from: Servier Medical Art by Servier. 11
Figure I-3. Visual representation of the synthetic transporters' carrier and channel mechanisms, respectively. 16
Figure I-4. Visual representation of the relay mechanism. 17
Figure I-5. 2D schematic representation of the periodic boundary conditions. 26
Figure II-1. DFT-optimized structures of the 1:1 chloride complexes 1, 2, 4, 7, 8, and 9. The N−H···Cl⁻ hydrogen bonds at the thiourea binding sites are drawn in blue, while the N−H···Cl⁻ and C−H···Cl⁻ interactions at the acylhydrazone binding unit are drawn in red. 38
Figure II-2. DFT-optimized structures of the 1:2 chloride complexes of 3, 5, 6, and 10. Remaining details as given in Figure II-1. 38
Figure II-3. Distributions of the electrostatic potential of 1, 2, 4, 7, 8, and 9, mapped on their molecular surfaces (0.001 e Bohr^{-1} contour). The surface colour ranges from -30 (blue) to 70 kcal mol^{-1} (red). The location of the $\boldsymbol{V_{S,max}}$ in front of the thioureas is shown with a black sphere, while the location of the highest value of $\boldsymbol{V_S}$ in front of the acylhydrazone is show with a pink one. Corresponding structures are presented below. 40
Figure II-4. Distributions of the electrostatic potential of 3, 5, 6, and 10. Remaining details are given in Figure II-3. 41
Figure III-1. Schematic identification of the A, B and C reference points, illustrated for the aromatic rings of 5. The vectors $\boldsymbol{AB}$, $\boldsymbol{SC}$ and $\boldsymbol{NH}$, used to assess the α, β and γ angles with the bilayer normal, are also illustrated for this molecule. 56
Figure III-2. Snapshots of MD runs of transporters 1, 3, 5, and 9, illustrating the orientations acquired at the water/lipid interface. Water molecules, aliphatic protons, and ions are omitted for clarity. 56
Figure III-3. Evolution of the relative position of the A, B and C (red, blue and magenta lines, respectively) reference points in illustrative MD runs in the $\boldsymbol{\mathcal{A}}$ (left) and $\boldsymbol{\mathcal{B}}$ (right) scenarios. The plotted green lines correspond to the evolution of the total number of N−H···Cl⁻ hydrogen bonds. The black line at z = 0 Å represents the water/lipid interface. 57
Figure III-4. Frequency profiles showing the distribution of the α (red line), β (blue line) and γ (magenta line) angles, assessed during the sampling period of the MD simulations of 1-4. Data were smoothed using Bézier curves. 58
Figure III-5. Average number of thiourea hydrogen bonds vs. the relative position of the centre of mass of 1, 2, and 3 (left for the thiourea and right for the acylhydrazone motif). The following colour scheme is used for the interactions with the water molecules (blue), chloride ions (green), ester groups (magenta for the *sn*-1 chains and purple for the *sn*-2 chains) and POPC head groups (orange). The black line at z = 0 Å represents the water/lipid interface. Data were smoothed using Bézier curves. 61
Figure III-6. MD snapshot illustrating the interaction of both thiourea binding units of 10 with two POPC phosphate head groups. 61
Figure III-7. Electron density profiles of transporters 1-6, with the full system plotted in black, phospholipids in green, water in blue, phosphorus atoms in orange, and the transporter in red. The free membrane profile is also shown as a magenta line. The transporter's profiles are scaled 5 times. The core of the POPC bilayer corresponds to z = 0 Å. 65
Figure III-8. Electron density profiles of transporters 7-10. Remaining details are given in Figure III-7. 66
Figure III-9. Average number of thiourea (left) and acylhydrazone (right) hydrogen bonds vs. the relative position of the centre of mass of 1, 3, and 5. Remaining details are given in Figure III-5. 67
Figure III-10. 2D histogram created from the α (top) and β (bottom) angle values monitored along the z coordinate positions of complex 1, throughout 41 independent US windows. The colour ranges from white (no occurrence) to red (200 occurrences). 68

Figure III-11. 2D histogram created from the α (top), β (middle), and γ (bottom) angle values monitored along the *z* coordinate positions of complex 3, throughout 41 independent US windows. The colour ranges from white (no occurrence) to red (200 occurrences)..... 69
Figure III-12. Molecular Mechanics interaction energies (kcal mol^{-1}) from the 41 independent US simulation windows, between the phospholipids and complexes 1 and 3, with the total energy (black), and van der Waals (blue) and electrostatic (red) contributions along the *z* coordinate. 70
Figure III-13. The equilibration and convergence of the US simulation windows were evaluated in 10 ns intervals (coloured accordingly), of which the last 50 ns were used to calculate the PMF of complexes 1 and 3. 71
Figure III-14. PMF of complexes 1 (red) and 3 (blue) as a function of the *z* coordinate throughout the sampling period of 41 independent US simulation windows..... 72
Figure III-15. PMF of complexes 1 and 3 as a function of the *z* coordinate throughout the sampling period of 41 independent US simulation windows. The error bars correspond to the bootstrap errors computed from 100 random data sets of equal size..... 72

Tables Index

Table I-1. Common lipid force fields used in MD simulations of lipids, from 2010 onwards. 29
Table II-1. Lipophilicity (log P values), chloride binding constants (K_a), intravesicular chloride at 300 s ($[Cl]^-_{in}$ at 300 s), and relative chloride transport activity (RTA) of receptors 1-10. Adapted from reference [120]. 35
Table II-2. Hydrogen bond dimensions (distance in Å; angles in °) for the N−H···Cl^- interactions in the thiourea binding site and for the N−H···Cl^-, C_{hyd}−H···Cl^- and C_{ar}−H···Cl^- interactions in the hydrazone moieties, computed from the DFT optimised structures. 39
Table II-3. Relevant electrostatic potential values ($\boldsymbol{V_S}$, kcal mol^{-1}) computed on the electron density surface of the thiourea and hydrazone binding units. 42
Table II-4. Energy of the hydrogen bonds (E_{HB}, kcal mol^{-1}) at the bond critical points in the N−H···Cl^- or C−H···Cl^- interactions between the thiourea or hydrazone binding units and chloride, together with the E^2 stabilisation energies (kcal mol^{-1}), between the antibonding orbitals of the N−H or C−H binding units (Ω^*_{N-H} or Ω^*_{C-H}) and the lone pair orbitals of Cl^- (n_{Cl^-}). 43
Table II-5. Uncorrected electronic binding energies ($\boldsymbol{\Delta\varepsilon_0}$), Zero-Point Corrections ($\boldsymbol{\Delta ZPE}$) and thermal corrected binding energies ($\boldsymbol{\Delta E}$), in kcal mol^{-1}, for the chloride complexes of 1-10. 45
Table III-1. GAFF2's default parameters and the modified parameters used in this work (based on the X−n2−n2−X dihedral angle). 49
Table III-2. RMSD values (Å) ascertained between reference X-ray single crystal structures (XRD) or B3LYP/6-31G(d) optimised structures and the MM optimised structures with GAFF2's default and updated parameters for the X−n2−ns−X dihedral angle. 50
Table III-3. Average α, β and γ angles (°), with their standard deviations, assessed for the cumulative sampling time in the MD runs of the different transporters. 59
Table III-4. Molecular Mechanics interaction energies (kcal mol^{-1})[a] between the phospholipids and compounds 1-10, listed together with their relative transport ability marks. 63
Table III-5. Comparison between the area per lipid, bilayer thickness, and root-mean-square error (RMSE) of the transporters' MD simulations sampling time and a free membrane system (100 ns of sampling). 64

Schemes Index

Scheme I-1. Structures of well-known natural ionophores. 15
Scheme I-2. Examples of recent synthetic compounds able to promote the transmembrane transport via a channel mechanism. 18
Scheme I-3. Examples of recent synthetic anion carriers. 19
Scheme I-4. Examples of synthetic ion transporters able to promote the ion transport through a relay mechanism. 20
Scheme I-5. Six examples of phospholipids supported by Lipid14 force field.[79] 30
Scheme II-1 34
Scheme II-2 35
Scheme III-1 49
Scheme III-2. Structures of the compounds mentioned in Table III-2, with the corresponding refcodes. 51
Scheme III-3. Representation of simulations' starting scenarios $\mathcal{A}$ and $\mathcal{B}$. 52

Abbreviations

Item	Definition
ABCC7	ATP-Binding Cassette Transporter
ADP	Adenosine Diphosphate
AMBER	Assisted Model Building with Energy Refinement
AMP	Adenosine Monophosphate
ATP	Adenosine Triphosphate
CF	Cystic Fibrosis
CFTR	Cystic Fibrosis Transmembrane Conductance Regulator
ClC	Chloride Channel
COM	Centre of Mass
C-PCM	Conductor-like Polarizable Continuum Model
CRT	Channel Replacement Therapies
CSD	Cambridge Structural Database
DCL	Dynamic Combinatorial Libraries
DFT	Density Functional Theory
DLiPC	1,2-dilinoleoyl-*sn*-glycero-3-phosphocholine
DLPC	1,2-dilauroyl-*sn*-glycero-3-phosphocholine
DLPE	1,2-dilauroyl-*sn*-glycero-3-phosphorylethanolamine
DLPG	1,2-dipalmitoyl-*sn*-glycero-3-phosphoglycerol
DMPC	1,2-dimyristoyl-*sn*-glycero-3-phosphocholine
DMPG	1,2-dimyristoyl-*sn*-glycero-3-phosphoglycerol
DMSO	Dimethyl Sulfoxide
DOPC	1,2-dioleoyl-*sn*-glycero-3-phosphocholine
DOPE	1,2-dioleoyl-*sn*-glycero-3-phosphoethanolamine
DOPG	1,2-dioleoyl-*sn*-glycero-3-phosphoglycerol
DOPS	1,2-dioleoyl-*sn*-glycero-3-phosphoserine
DPPC	1,2-dipalmitoyl-*sn*-glycero-3-phosphocholine
DPPE	1,2-dipalmitoyl-*sn*-glycero-3-phosphoethanolamine
DPPG	1,2-dipalmitoyl-*sn*-glycero-3-phosphoglycerol
DSPG	1,2-distearoyl-*sn*-glycero-3-phosphoglycerol
E^2	Second-order perturbation theory stabilization energies
ECFS	European Cystic Fibrosis Society
EHB	Energy of the Hydrogen Bonds
FDA	Food and Drug Administration
FES	Free Energy Surface
fs	Femtosecond
GAFF	Generalized AMBER Force Field
GPU	Graphics Processing Unit
IR	Infrared
LUV	Large Unilamelar Vesicle
MBAR	Multistate Bennet Acceptance Ratio Method
MD	Molecular Dynamics

MetaD	MetaDynamics
MM	Molecular Mechanics
NBDs	Nucleotide Binding Domains
NBO	Natural Bond Orbital
NMR	Nuclear Magnetic Resonance
NPT	Isothermal-Isobaric Ensemble
NVE	Microcanonical Ensemble
NVT	Canonical Ensemble
PBC	Periodic Boundary Conditions
PC	Phosphatidylcholine
PE	Phosphatidylethanolamine
PEPC	1-palmitoyl-2-elaidoyl-*sn*-glycero-3-phosphocholine
PKA	Cyclic AMP dependent Protein Kinase
PME	Particle Mesh Ewald
PMF	Potential of Mean Force
POPC	1-palmitoyl-2-oleoyl-*sn*-glycero-3-phosphocholine
POPE	1-palmitoyl-2-oleoyl-*sn*-glycero-3-phosphoethanolamine
POPG	1-palmitoyl-2-oleoyl-*sn*-glycero-3-phosphoglycerol
QTAIM	Quantum Theory of Atoms in Molecules
R	Regulatory Domain
REMD	Replica-Exchange Molecular Dynamics
RESP	Restrained Electrostatic Potential
RMSD	Root-Mean-Square Deviation
RMSE	Root-Mean-Square Error
RTA	Relative Transport Activity
SM	Sphingomyelin
SMD	Steered Molecular Dynamics
SOPC	1-stearoyl-2-oleoyl-*sn*-glycero-3-phosphocholine
TBACl	Tetrabutylammonium Chloride
TMDs	Transmembrane Domains
UI	Umbrella Integration
US	Umbrella Sampling
UWHAM	Unbinned Weighted Histogram Analysis Method
vFEP	Variational Free Energy Profile
V_S	Electrostatic Potential
WHAM	Weighted Histogram Analysis Method
XRD	X-Ray Diffraction single crystal structures
ZPE	Zero-Point Energies
ε_0	Electronic Energies

Chapter I.
Introduction

Summary

This chapter starts by giving an overview on the biomembrane constitution and function as trafficking mediator between the cell and its environment. Subsequently, diseases derived from ion channel defects – channelopathies, such as Cystic Fibrosis – are approached, with special interest on deficient chloride transmembrane transport. A brief presentation of the recent development on synthetic transporters is presented, as potential channel replacement therapies. Finally, this chapter gives a succinct description on the basic concepts of Molecular Dynamics simulations, which will be used on this work as powerful tool to obtain a deep understanding how the synthetic transporters, at the atomistic level interact with a POPC membrane model.

I.1. Biological membrane

Cell membranes are essential to the cell's life and proper functioning.[1] The plasmatic membrane surrounds the cell, defining its boundaries, acting as a semipermeable barrier, and differentiating the cytosolic and extracellular environments.[1, 2]

The composition of a membrane heavily dictates its function, a feature that also applies to the cell's organelles (*e.g.*, nucleus, lysosomes, endoplasmic reticulum, mitochondria).[3] The general structure common to biological membranes consists of two thin films of lipids assembled in a bilayer by hydrophobic interactions (*vide infra*).[1, 2] This supramolecular assembly also contains several embedded proteins, responsible for facilitating the regulated transport of several solutes and allowing cell signalling.[2] Moreover, these components are arranged according to the fluid mosaic model, a two-dimensional solution of membrane proteins. In addition, the structural integrity of the membrane is dynamic and fluid, allowing lipids to switch between layers, giving different lipidic compositions to the cytosolic and extracellular membrane interfaces.[2] An illustration of the membrane composition is presented in **Figure I-1**.

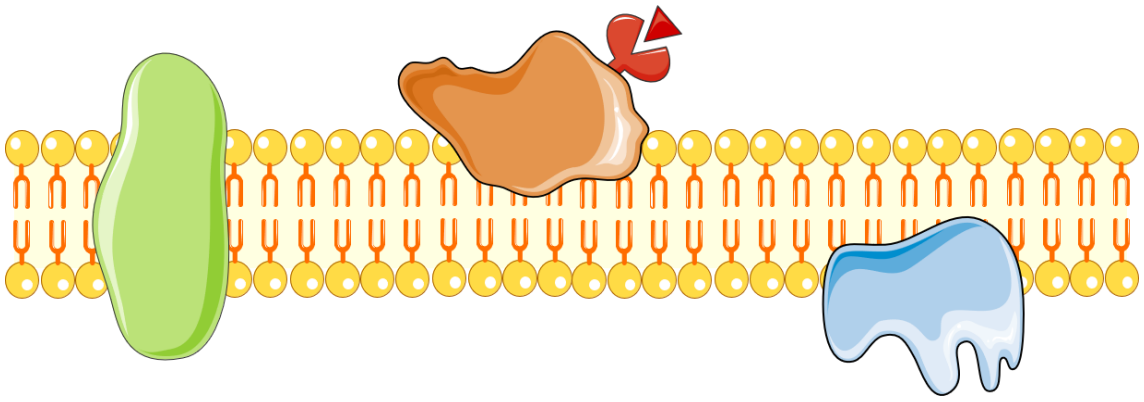

Figure I-1. Schematic illustration of the biological bilayer, with the phospholipids represented in yellow, a peripheric protein in blue, an integral protein in green, a peripheric glycoprotein in orange and its carbohydrate moiety in red. Resources from: Servier Medical Art by Servier.

Beyond the phospholipids, biological membranes incorporate other basic structural units, such as sphingolipids and steroids (cholesterol and its derivatives).[1, 2] Phospholipids are amphipathic molecules composed of a hydrophilic head (polar), in contact with the aqueous medium, and hydrophobic tails (nonpolar).[1, 2] These molecules self-assemble as

bilayers or micelles, due to van der Waals interactions between the aliphatic tails and electrostatic interactions between the head groups.[1, 2] While cholesterol is evenly distributed across the inner and outer leaflets, most sphingolipids and phosphatidylcholine (PC) lipids are found in the outer layer. On the other hand the phosphatidylethanolamine-based (PE) molecules are typically in the inner layer.[1, 2]

I.1.1. Transport across the membrane

Small molecules are transported through the cellular membranes by passive or active transport.[3] The former can occur through simple or facilitated diffusion, without energy spending. On the other hand, active transport comes with an energetic cost.[3]

In simple diffusion, gases such as CO_2 and O_2, small uncharged polar molecules such as water and glycerol, and hydrophobic molecules like steroid hormones can move across the membrane without assistance, down their concentration gradient. The diffusion rate is dependent on the concentration, size, and hydrophobicity of the molecule, intrinsically related with partition coefficient, among other factors.[1, 2] On the other hand, the simple diffusion of charged entities only allows transport rates lower than needed to fulfil the cell's needs, as their diffusion is energetically hindered by their charge and degree of hydration.[1] In other words, these charged species prefer to rest in the membrane water phase.

Overall, the diffusion of small molecules across biological membranes is operated by a complex machinery of proteins, including carrier proteins, channels, and ATP-powered pumps.[1] Carrier proteins are integral proteins responsible for the transport of small neutral or ionic species across the membrane, as these molecules bind to the protein on one side of the membrane and are released to the other.[1, 3] Within carrier proteins, there are *uniporters*, that transport molecules down their concentration gradient, and coupled transporters, which act similarly but moving other substances concomitantly. If the movement of the second solute is codirectional to the first, the protein is a *symporter* or *co-transporter*, whereas if the directions are opposite, the protein is called an *antiporter* or *exchanger*.[1] Channels facilitate the diffusion of water, some ions, or hydrophilic molecules across the membrane, according to their concentration gradient. They can be open at all

times, called *non-gated channels*, or close in response to electric or chemical stimuli, called *gated channels*.[1] These membrane proteins span the entire membrane and interact poorly with the transported molecule, allowing great transport rates.[2] On the other hand, as carrier proteins require conformational changes to obtain the alternative exposures of binding sites on each side of the membrane,[1] their transport rates are substantially lower than channels.[2] Alternatively, the movement of solutes against their electrochemical gradient can be mediated by *ATP-pumps* at the expense of metabolic energy, obtained from the hydrolysis of ATP to ADP.[3] This process is called active transport.[1, 3] A schematic illustration of all these transport mechanisms, briefly described, is presented in **Figure I-2**.

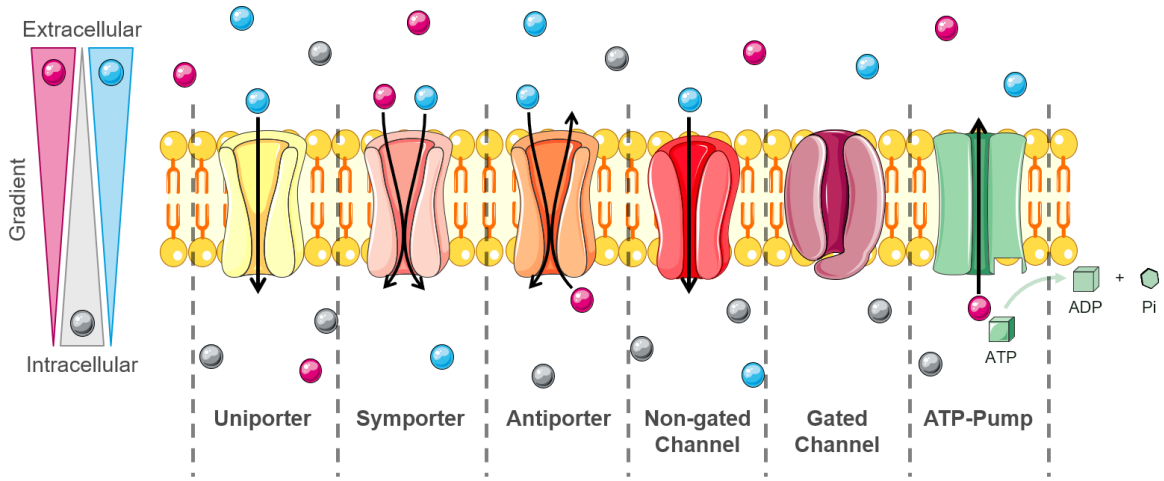

Figure I-2. Schematic representation of the transport mechanisms associated with protein membranes. Resources from: Servier Medical Art by Servier.

The malfunction of ion channels leads to many human diseases, so called channelopathies, the most common of which is Cystic Fibrosis (CF). This has been the driving force for the research and development of drugs to treat specific ion channel mutations, genetic therapy, and drug-like molecules for channel replacement therapies (CRT).

I.2. Cystic Fibrosis

CF is the most common lethal genetic disease in Caucasian populations.[4, 5] It affects over 70 thousand people worldwide,[6] of which 48 thousand are present in the 35 European countries covered by the European Cystic Fibrosis Society (ECFS).[7] Moreover, in the European Union, one in every 2000-3000 babies is diagnosed with CF at birth. Regarding patient mortality, according to ECFS's 2018 report, the most frequent age range at death is between 21 and 30 years, and very rare for small children.[7]

CF is a channelopathy caused by a mutation in the gene that encodes cystic fibrosis transmembrane conductance regulator (CFTR) protein – an ABC transporter (ABCC7) expressed in many epithelial and blood cells.[5, 8-10] There are more than 1700 known mutations,[7, 8] that produce a wide variety of effects on CFRT, classified in functional categories. Class I mutations prevent the synthesis of a functional protein, by premature stop codons or frame shifts,[5, 8-10] while Class II mutations lead to protein processing defects, retention or even degradation. Both mutations prevent an adequate CFTR Cl^- channel expression and can be associated with multiorgan diseases like infertility, progressive pulmonary disease, and pancreatic deficiency.[5, 8-10] Class III missense or deletion mutations are responsible for the biosynthesis of channels insensitive to cyclic AMP activation and regulation.[5, 8-10] Class IV mutant CFTR present normal expression and sensitivity to regulation, but reduced chloride conductance, generally associated with milder diseases.[8, 11] Class V mutations are responsible for a substantial reduction in the mRNA or protein, or both. At last, Class VI mutations revolve around substantial plasma membrane instability.[8]

The diagnosis of CF is a multistep process, composed by a new-born screening, a sweat test (measurement of the chloride concentration present in the patient's sweat), a genetic or carrier test (to verify if the patient carries a mutation of the CFRT gene), and a clinical evaluation.[6] Hence, it is of utmost importance to have an early diagnostic, with 75% of the CF patients being diagnosed by age 2, as CF is dominated by chronic lung disease, the main cause of morbidity and mortality.[7]

I.2.1. Cystic Fibrosis Transmembrane conductance Regulator (CFTR)

CFTR is an ATP-binding cassette (ABC) transporter that distinctively functions as an anion channel, located in the apical membrane of respiratory and intestinal epithelial cells.[12] In contrast to other ABC transporters, in which ATP-driven conformational changes drive substrate transport against their electrochemical gradient, CFTR gated channel allows for transmembrane flow of ions down this gradient.

The CFTR protein is composed by two transmembrane domains (TMDs) and regulated by two cytosolic nucleotide binding domains (NBDs) and one regulatory (R) domain, also located in the cytosol.[13] The gating of the CFTR channel is a two-way process: first, phosphorylation of the R domain by cyclic AMP dependant protein kinase (PKA) is required for channel activation; subsequently, pore gating of the phosphorylated channel is driven by binding and hydrolysing ATP in the NBDs.[13]

I.2.2. Therapeutic Approaches

To adequately find viable therapeutic strategies for CF, a clear understanding of the CFTR Cl^- channel dysfunction mechanisms is required. Based on the nature of these defects, small molecules were found to restore some activity to the mutant protein, thereby mitigating disease manifestations.[14] CFTR potentiators were the first class of drugs to be successfully developed, small molecules that increase the opening probability of the mutant channel, improving the anion efflux across the plasma membrane.[15, 16] By contrast, CFTR correctors are responsible for the enhancement of the defective protein processing and trafficking.[14]

Effective CFTR modulators (small molecules designed to restore the activity of mutant CFTR) such as ivacaftor, an FDA approved drug to treat certain CF mutations,[17] can slow or prevent lung disease progression if administrated early enough.[18] The positive results provided by ivacaftor accelerated the development of CFTR modulators for more common mutations. However, the usage of a single CFTR modulator was found to be ineffective in Class II CFTR defects,[19] whilst the CFTR corrector-potentiator combination therapy proved to be efficient in some specific mutations (such as homozygous patients for p.Phe508del,[20] but not heterozygous).[21]

Besides CFTR modulators, novel small-molecule drugs are in development as alternative pharmacological treatments for CFTR mutations not yet covered, or to yield long-term benefits via gene replacement therapy.[22] Additionally, alternative Cl^- pathways have been suggested as a compensation, such as the voltage gated ClC family, cAMP-activated, Ca^{2+}-activated, and volume-regulated Cl^- channels.[11, 23] However, the requirement for specific target therapies present a burdensome challenge in the development of CF treatments.

To overcome the need for multiple therapies, low molecular weight synthetic ion transporters can be used to mimic the action of natural ion channels, exerting powerful effects on biological systems. These molecules also proved to be very valuable in the study of membrane transport, biochemistry, and physiology.[23] Moreover, synthetic transporters are promising CRTs, not only for CF but for channelopathies in general. Thus, this thesis focuses on this alternative with high potential.

I.2.3. Synthetic Ionophores

To date, significant efforts have been devoted in the design and development of a plethora of effective ionophores, aiming to facilitate the transport of ions across the lipid bilayer, in defective ion channels, using various mechanisms (*vide infra* – carrier, channel, or relay). An ionophore can be defined as *A compound which can carry specific ions through membranes of cells or organelles.*[24] This class of compounds typically has hydrophilic pockets that form specific ion binding sites, and an exterior surface to allow the complex to cross the lipidic membrane.[25] Ionophores can be naturally occurring compounds such as peptides, macrotetrolides, polyethers and cyclic depsipeptides, or small synthetic molecules.[26]

In contrast with cation ionophores, such as valinomycin and gramicidin A, natural anionophores are not as common. Natural occurring anion ionophores include duramycins, pamamycins, prodigiosins, and amphotericin B.[27] The different compounds are represented in **Scheme I-1**.

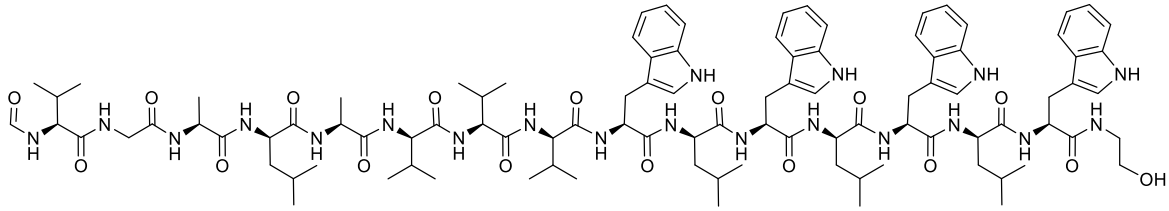

Gramacydin A

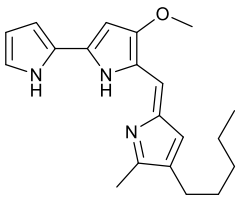

Prodigiosin

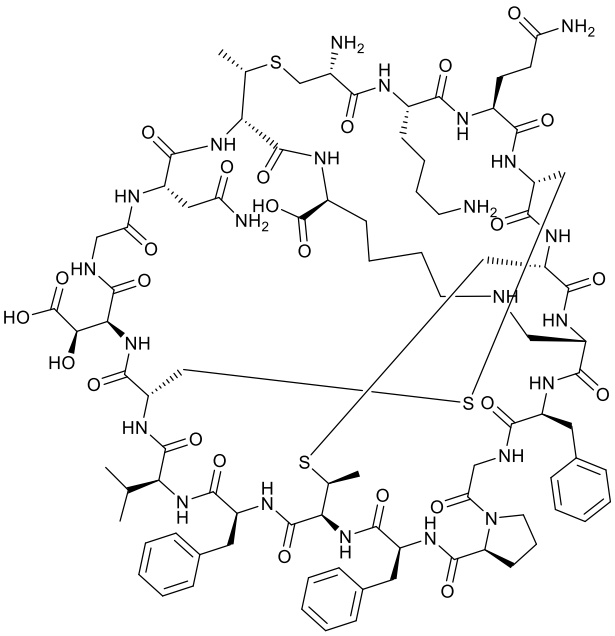

Duramycin

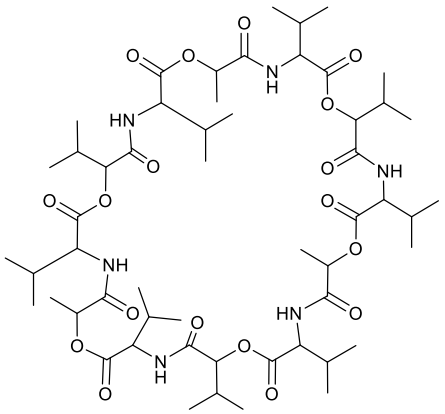

Valinomycin

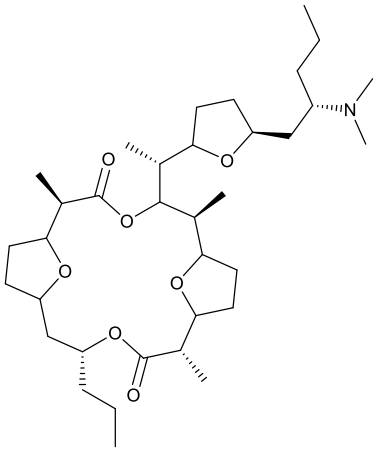

Pamamycin

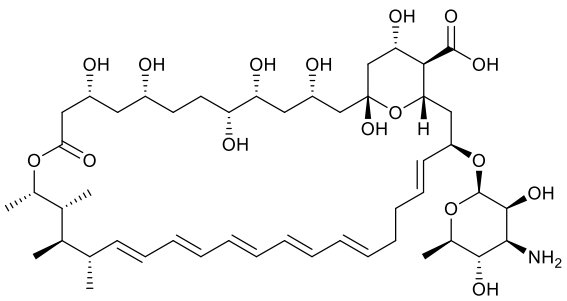

Amphotericyn B

Scheme I-1. Structures of well-known natural ionophores.

The lack of natural anionophores greatly impacted the study and development of novel synthetic anion transporters, molecules with potential as therapeutic agents in the treatment of channelopathies, aiming to replace deficient channels. Moreover, these studies brought new insights on the fundamentals of the ion transport processes.[28] To date, the number and diversity of synthetic transporters still continues to increase apace. Detailed reviews on the most recent advances on anion receptors and synthetic transporters can be found on references [23, 27-39].

Synthetic ion transporters that mimic the action of natural ion transporters can be classified as mobile carriers or ion channels, as illustrated in **Figure I-3**.

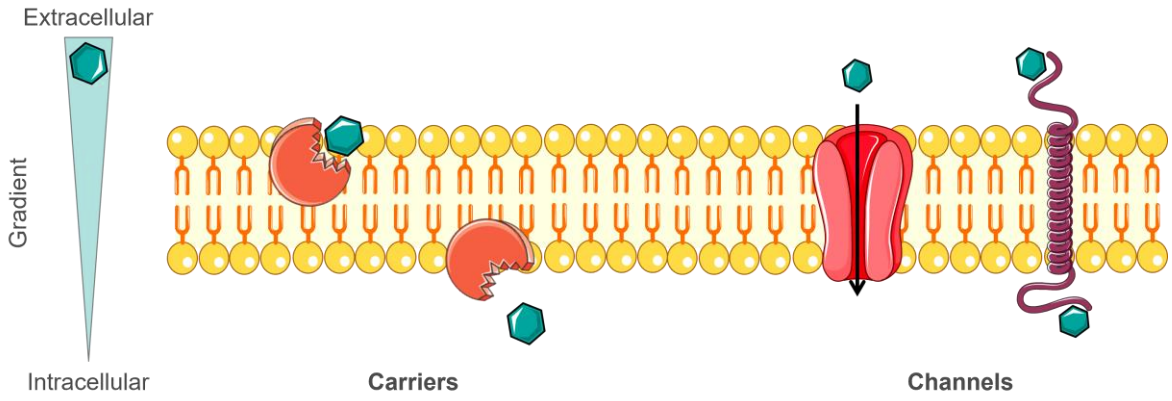

Figure I-3. Visual representation of the synthetic transporters' carrier and channel mechanisms, respectively.

As demonstrated in **Figure I-3**, synthetic transporters that form complexes with the ionic species, recognising it and carrying it in or out of the cell, are designated as carriers. This mechanism displays low rates of transport, but compensates with its high selectivity.[23] In contrast, ion channels span the entire bilayer, forming ion-conductance pathways that allow the flow of ions across the membrane, at high transport rates.[23] These structures can be composed by a single unit (monomeric channel), or several self-assembled molecular entities (self-assembled pores).[23] Moreover, the synthetic anionophores can also use the more unconventional relay mechanism to promote the transport of ions across the bilayer. In this mechanism, the receptor contains two binding motifs positioned in opposite sides of the membrane, which permits the sweeping of the anion between both leaflets of the bilayer, as illustrated in **Figure I-4**.

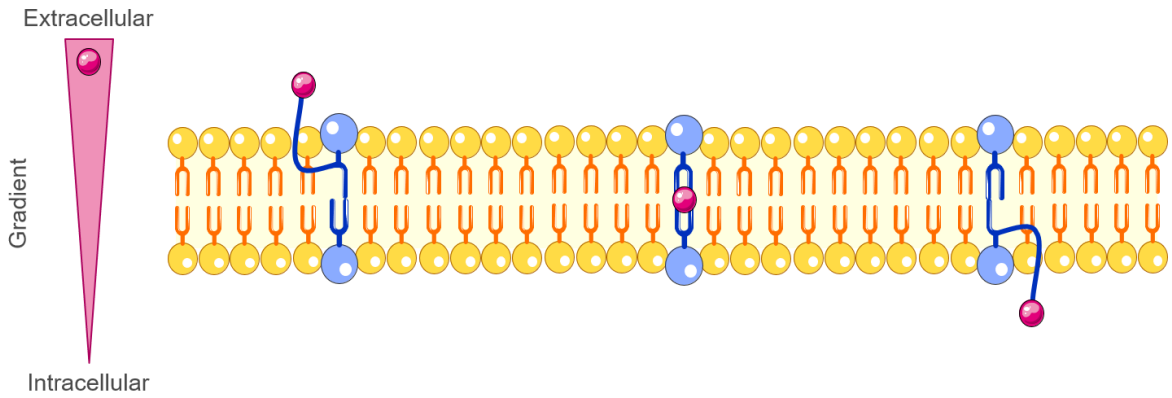

Figure I-4. Visual representation of the relay mechanism.

In the recent years, significant progress was made in the design of novel synthetic ion transporters. Saha *et al.* used small bis(diol) molecules to promote selective transmembrane transport of chloride ions, achieved by a supramolecular nanotubular assembly formation. Moreover, this system established an antiport mechanism with considerable chloride selectivity.[40] This group also studied three macrocycles decorated with different alkylated groups with varying chain-lengths up to 14 carbons, which are interesting scaffolds for the development of gated or responsive channels.[41] The intermediate dialkylated macrocycle (R_1 = tetradecane and R_2 = H) is of particular interest, due to its good balance between the hydrophobicity for insertion in the membrane, and hydrophilicity for anion transport, allowing for the formation of a synthetic ion channel. The above-mentioned molecules are illustrated in **Scheme I-2**.

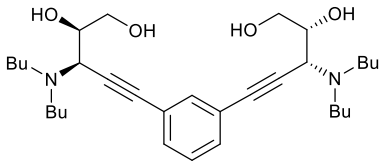

(2*R*,2'*R*,3*R*,3'*R*)-5,5'-(1,3-phenylene)bis(3-(dibutylamino)pent-4-yne-1,2-diol)

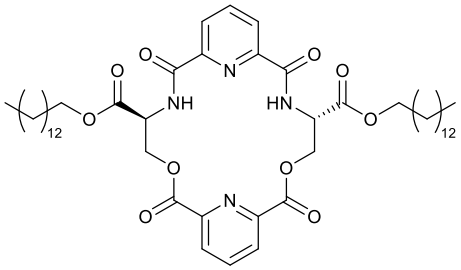

5,15-ditetradecyl (5S,15S)-2,7,13,18-tetraoxo-3,17-dioxa-6,14,23,24-tetraazatricyclo[17.3.1.1^{8,12}]tetracosa-1(23),8(24),9,11,19,21-hexaene-5,15-dicarboxylate

Scheme I-2. Examples of recent synthetic compounds able to promote the transmembrane transport via a channel mechanism.

Regarding carrier transporters, for instance, Quesada and co-workers developed a series of prodigiosin-inspired triazole based derivatives, capable of exchanging chloride with nitrate or bicarbonate in vesicle models.[42] Gale *et al.* recently explored the excellent anion-binding properties of squaramide receptors and transporters.[43] These squaramide derivatives undergone thorough *in silico* studies that provided a comprehensive elucidation of the transmembrane chloride transport mechanisms.[44] Reany and co-workers investigated the ion-transport properties of bambusuril-based receptors, one of which sketched in **Scheme I-3**. In spite of all these receptors being great anion binders, only semithiobabus[6]uril exhibited effective anion transport capabilities, by polarizing lipid membranes through selective anion uniport.[45] These are just some examples of the most recent work conducted on this field of Supramolecular Chemistry.

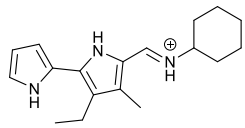

(*E*)-*N*-((3-ethyl-4-methyl-1*H*,1'*H*-[2,2'-bipyrrol]-5-yl)methylene)cyclohexanaminium

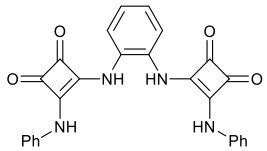

4,4'-(1,2-phenylenebis(azanediyl))bis(3-(phenylamino)cyclobut-3-ene-1,2-dione)

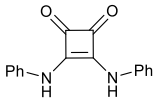

3,4-bis(phenylamino)cyclobut-3-ene-1,2-dione

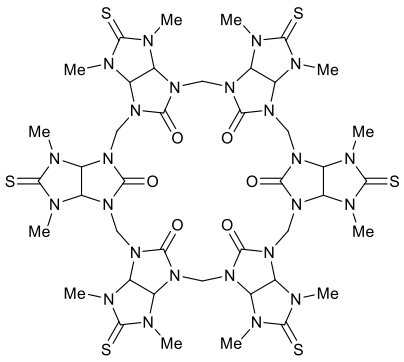

5,7,13,15,21,23,29,31,37,39,45,47-dodecamethyl-6,14,22,30,38,46-hexasulfanylidene-1,3,5,7,9,11,13,15,17,19,21,23,25,27,29,31,33,35,37,39,41,43,45,47-tetracosaazatridecacyclo[41.5.1.1^{3,9}.1^{11,17}.1^{19,25}.1^{27,33}.1^{35,41}.0^{4,8}.0^{12,16}.0^{20,24}.0^{28,32}.0^{36,40}.0^{44,48}]tetrapentacontane-49,50,51,52,53,54-hexone

Scheme I-3. Examples of recent synthetic anion carriers.

In 2008, the Smith group designed a series of phosphatidylcholine derivatives containing chloride recognition units, that promoted the transport of the anion across the lipid bilayer, by a relay mechanism. The structural similarity between these molecules and the phospholipids, provides a high compatibility with the membrane environment.[46] More recently, Wang *et al.* reported a new synthetic phospholipid receptor decorated with benzo-18-crown-6 macrocyclic binding motif (see **Scheme I-4**), which can perform cation ($Rb^+ \geq Cs^+ > K^+ > Li^+ \geq Na^+$)transport across the lipid bilayer, also using a relay mechanism.[47]

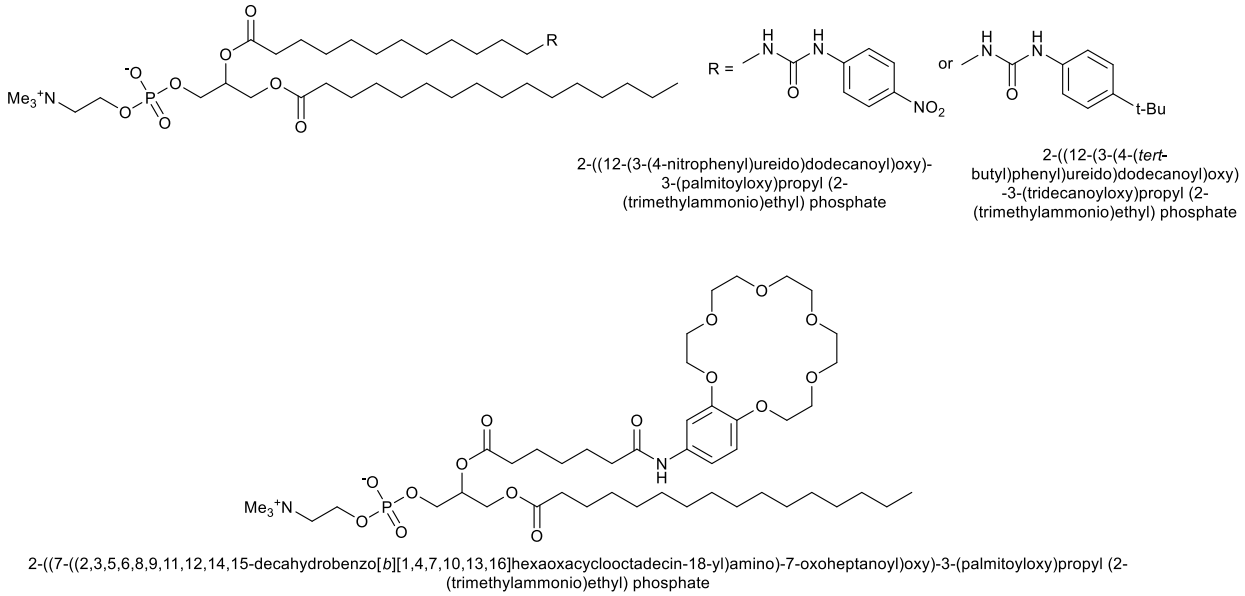

Scheme I-4. Examples of synthetic ion transporters able to promote the ion transport through a relay mechanism.

Typically, the ionophores anion recognition relies on hydrogen bonds or electrostatic interactions. This thesis will focus on the effectiveness of thiourea based receptors decorated with acylhydrazone binding motifs, allowing to evaluate the relevance of the acylhydrazone moieties as secondary binding units for anion recognition and transport.

A key factor that defines the performance of a synthetic receptor as a transmembrane transporter, is its binding strength. Indeed, the molecules of interests must have a delicate balance between strong binding constants (forming a strong complex with the anion, preventing its release after the diffusion) and weak binding constants (inhibiting the complexation with the solvated anion), to be potential transmembrane transporters.[48, 49]

The same balance is required regarding the lipophilic character of the molecules. LogP values (logarithm of the molecules' octanol/water partition coefficient) for higher anion effluxes to be achieved.[50] Moreover, the ability of a synthetic receptor to partition into the lipid bilayer (partition coefficient) can be fine-tuned by adding structural motifs with different lipophilicities, such as alkyl chains, and fluorinated units or aromatic groups.[27]

Therefore, a delicate equilibrium of lipophilicity and anion binding must be considered in the design of a synthetic anion transporter. With this is mind, molecular modelling methods have proven to be of extreme importance in the development of new synthetic anion transporters, allowing the prediction of several relevant properties as well as the study of the interaction between ionophores and lipid bilayers.[27, 39, 44, 50]

I.3. Molecular Dynamics

Molecular Dynamics (MD) is a computer simulation deterministic method that allows to follow the evolution of a given system's properties throughout time, by predicting its configurations while generating trajectories.[51-53] These trajectories can be determined by integrating Newton's equation of motion for the interacting particles, whilst their forces and potential energies are calculated using Molecular Mechanics (MM) force fields, giving the total energy as presented in **Eq. I-1**:[51]

$$E_{Total} = E_{Potential} + E_{Kinetic} \qquad \textbf{Eq. I-1}$$

The interval of time between each Newton's equation of motion integration during a MD simulation is called a "time step". The time step should sample the fastest vibration of the system (typically C-H, O-H, and N-H bonds) – generally 1-10 femtoseconds (fs) – considering its impact in the quality and cost of the MD simulation.[51-53] However, covalent bonds between the heavy atoms and hydrogens can be constrained to allow larger timesteps, typically 2 fs,[54] using well-known algorithms like SHAKE,[55] SETTLE[56] or LINCS.[57] Additionally, the trajectory recorded along a MD simulation can be used to determine macroscopic thermodynamic properties of the system, as long as it represents an ergodic system (*i.e.*, all accessible microstates are equiprobable over a long period of time).[51, 52]

Typically, MM force fields can be described in terms of the intra- and inter-molecular forces within the system, corresponding to bonded (bond lengths, bond angles and torsion angles) and nonbonded (van der Waals and electrostatic) interactions, respectively. Pre-determined functional are used to estimate these interactions, allowing to calculate the potential energy ($E_{Potential}$ or $\mathcal{V}(\boldsymbol{r}^N)$) of the system, typically as presented in **Eq. I-2**.[51, 58, 59]

$$\mathcal{V}(\boldsymbol{r}^N) = \sum_{bonds} \frac{k_i}{2}(l_i - l_{i,0})^2 + \sum_{angles} \frac{k_i}{2}(\theta_i - \theta_{i,0})^2 + \sum_{torsions} \frac{V_n}{2}(1 + \cos(n\omega - \gamma)) + \sum_{i=1}^{N}\sum_{j=i+1}^{N}\left(4\varepsilon_{ij}\left[\left(\frac{\sigma_{ij}}{r_{ij}}\right)^{12} - \left(\frac{\sigma_{ij}}{r_{ij}}\right)^{6}\right] + \frac{q_i q_j}{4\pi\varepsilon_0 r_{ij}}\right)$$ **Eq. I-2**

This equation denotes the MM potential energy of the system as function of the positions (**r**) of N atoms of the system. The first two terms represent the interaction between pairs of bonded atoms and valence angles in the molecule, respectively. These are modelled by harmonic potentials that give the energy penalty as the bond length (l_i) or angle (θ_i) deviates from its equilibrium value, $l_{i,0}$ and $\theta_{i,0}$, respectively. The third term is a torsional potential that describes the energy variations as a bond rotates. The fourth and final contribution represents the non-bonded interactions, calculated between all pairs of atoms (ij) that are in different molecules or separated by at least three bonds. Non-bonded interactions are usually modelled using Coulomb potential terms for electrostatic interactions and Lennard-Jones potentials for van der Waals interactions.[51, 58, 59]

The presented functional form is generally adopted by different atomistic force fields developed following equivalent methodologies but with different values for the parameters,[51, 58, 59] The parameterisation of the force field is carried out according to the desired property prediction that is expected from it. Therefore, it is not necessarily a failing if a force field is unable to predict a parameter that had not been included in the parameterisation process.[51] In the Generalized AMBER Force Field (GAFF), the equilibrium values for bond lengths and angles were taken from other AMBER force fields, *ab initio* calculations and crystal structures, and the corresponding force constants were estimated empirically.[58, 59] A second generation of the GAFF force field is currently in development (GAFF2), aiming to achieve improved performances, and its beta version has been available since *ca*. 2016/2017.[60]

For some systems, where high accuracy is required, it is desirable to develop a specific force field to predict a particular property of the system. However, usually it is preferable to have a given set of parameters able to model a series of related molecules.

This is called transferability of the functional form and parameters, and it is an important feature of force fields.[51] On the other hand, a force field suitable for modelling a given family of compounds is usually not fit to accurately model the properties of another one, which led to the development of specific force fields for proteins, nucleic acids, phospholipids, carbohydrates, as well as for ions and even water. On the other hand, the compatibility between force fields is of paramount importance in the simulation of complex systems composed by different types of molecules (e.g., the diffusion of a drug across a phospholipid bilayer), which necessarily requires requiring the combination of parameters of different force fields.

The distinction between atoms of the system is defined by their "atom types". The atom types property identifies the element, hybridisation state, and local environment of each atom. Furthermore, the charge distribution in a molecule is commonly represented by an arrangement of fractional point charges, reproducing its electrostatic properties.[51] When the charges are restricted to the nuclear centres they are called "partial atomic charges". These charges can be obtained through *ab initio* calculations, empirical or semi-empirical methods. The selected method to estimate the partial atomic charges must be consistent with charge derivatization method applied on the force field development. Thus, the Restrained Electrostatic Potential (RESP) charges are used in GAFF, estimated at the HF/6-31G* level of theory, following the Merz-Singh-Kollman scheme,[61-63] using six points per layer across four concentric layers.[64] However, in the case of large organic molecules, AM1-BCC charges can also be used together with the GAFF versions, as they were parameterised to reproduce the aforementioned RESP charges.[65, 66]

Force fields can be classified in three different types, in agreement with their atomistic detail: *all-atom*, *united atom*, and *coarse-grained* force fields. The first explicitly represent all atoms in the system, while *united atom* interatomic potentials treat nonpolar hydrogens and their heavy atom as one interaction centre (*e.g.*, methyl groups).[67] The latter uses larger particles to represent groups of atoms or functional groups, to increase computing efficiency by sacrificing structural information in larger systems and/or longer simulations.[51, 67] Additionally, since standard atomistic force fields do not realistically describe systems' polarization in high-dielectric mediums (such as water), due to the fixed atom-centred charges used to describe electrostatic interactions, *polarizable* force fields were introduced to account for the charge variations in dielectric environment.[68, 69]

In the most natural formulation, MD simulations are performed for an isolated system, called microcanonical ensemble (NVE, constant number of particles – N, volume – V and energy – E). For this, however, it is imperative to make sure the correct dynamic trajectories are preserved. Different thermostats and barostats can be employed to obtain static and thermodynamic properties, through thorough control of the temperature (thermostat) and pressure (barostats) of the system, as long as they produce the correct canonical ensemble (NVT, constant number of particles – N, volume – V and temperature – T) or isothermal-isobaric ensemble (NPT, constant number of particles – N, pressure – P and temperature – T).[51-53]

In classical MD simulations, the total energy is given by the sum of the potential energy of the particles (**Eq. I-2**) and their kinetic energy, associated with their motion and is dependent of the temperature (**Eq. I-3**):

$$\mathcal{K} = \sum_{i=1}^{N} \frac{|\boldsymbol{p}_i|}{2m_i} = \frac{k_B T}{2}(3N - N_c) \qquad \textbf{Eq. I-3}$$

Where $\boldsymbol{p}_i$ and m_i are the total momentum and mass of the particle i, respectively, k_B the Boltzmann's constant, and T the temperature of the system. In a MD simulation, the total linear momentum is often constrained to a value of zero, and so the number of constrains on the system (N_c) would be equal to three. Moreover, each particle in an equilibrium system contributes $k_B T/2$ to the kinetic energy, according to the theorem of the equipartition of energy. Therefore, for a system with N particles, moving across three dimensions, the kinetic energy is given by $3Nk_B T/2$.[51]

The virial theorem of Clausius is usually used to calculate the pressure in a MD simulation. It is defined as the sum of the products of the coordinates and forces acting on a given particle.[51] This theorem states that the virial is equal to $-3Nk_B T$.[51, 70] However, since the only forces in an ideal gas are derived from interactions between itself and the container, the virial equals to $-3PV$ in these cases. The total virial for a real system equals to the sum of the ideal gas and the interaction between the particles contributions, as given in **Eq. I-4**:

$$\mathcal{W} = -3PV + \sum_{i=1}^{N} \sum_{j=i+1}^{N} r_{ij} \frac{dv(r_{ij})}{dr_{ij}} = -3Nk_BT \qquad \textbf{Eq. I-4}$$

With the interactions between particles i and j being represented by $v(r_{ij})$.[51] If the derivative $dv(r_{ij})/dr_{ij}$ is written as the force acting between those two particles, f_{ij}, the pressure is given by **Eq. I-5**:

$$P = \frac{1}{V}\left[Nk_BT - \frac{1}{3}\sum_{i=1}^{N} \sum_{j=i+1}^{N} r_{ij} f_{ij}\right] \qquad \textbf{Eq. I-5}$$

Since the forces are routinely calculated during the MD simulation, the virial and the pressure of the system can be obtained with little computational effort.[51]

To be able to calculate macroscopic properties using a relatively small number of particles, the correct treatment of boundaries and boundary effects must be considered. In bulk phenomena studies, periodic boundary conditions (PBC) can be used, so that the particles may experience forces as if they were in a bulk fluid.[51, 71] This makes all particles in a simulation box independent of their distance to the edge. The box is replicated in all dimensions of the system, which is surrounded by 26 images of itself. When a particle leaves the box during a simulation, it is immediately replaced on the opposite side, maintaining the number of particles constant throughout the simulation,[51] as illustrated in **Figure I-5**. Besides the most common and simple cubic or orthorhombic cell shapes, there are others like the hexagonal prism, truncated octahedron, rhombic dodecahedron, and the elongated dodecahedron, that can be used depending on the geometry of the system in mind (e.g., if simulating spherical molecules like globular proteins, truncated octahedron and rhombic dodecahedron periodic cells requires fewer solvent molecules due to its shape, resulting in increased computational performance).[51]

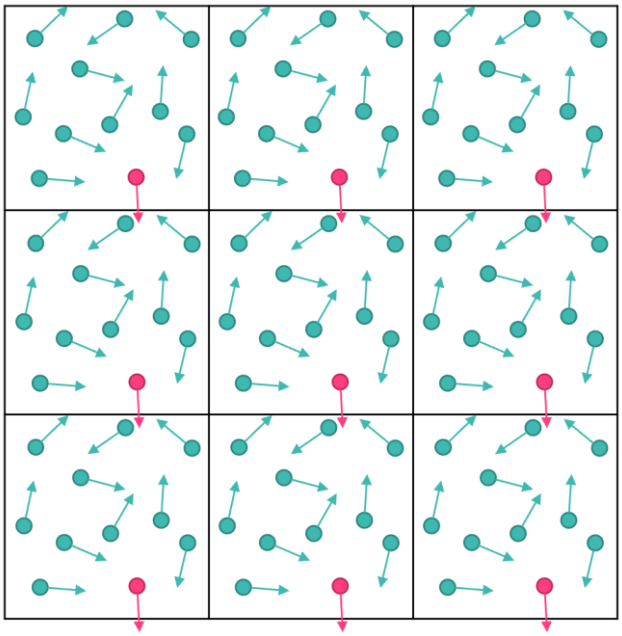

Figure I-5. 2D schematic representation of the periodic boundary conditions.

I.3.1. Enhanced Sampling techniques

Although MD simulations provide an adequate method for the study of the dynamic behaviour of a given system, stochastic MD simulations are likely to result in a poor dynamic characterisation, due to entrapment of the system in irrelevant free energy minima for a long time, thus impairing the sampling process.[72] In the case of transmembrane transport, channels and transporters suffer big conformational changes. These processes are too complicated and time-consuming for stochastic MD simulations, requiring the implementation of enhanced sampling algorithms.[72]

Some enhanced sampling methods are Umbrella Sampling (US),[73] Steered Molecular Dynamics (SMD),[74] MetaDynamics (MetaD),[75] and Replica-Exchange Molecular Dynamics (REMD),[76] of which US will be explained further below due to its application in this thesis. The mentioned techniques allow the calculation of the potential of mean force (PMF), which describes how the free energy varies along a given reaction coordinate ξ (such as the torsion of a bond, separation of two atoms, and more).[51]

I.3.2. Umbrella Sampling

The US technique aims to tackle the sampling problems in complex systems by segmenting the reaction coordinate along separate parallel "windows". Not only does this approach increase the efficiency of the overall simulation, as it is also possible to improve the sampling with intermediate windows or increased simulation time. In the US method, the system sampling is restricted around a given part of the reaction coordinate, on each window, defined by a harmonic restrain. The harmonic bias potential along the reaction coordinate $\omega(\xi)$ of strength k_i is given by:[51, 73]

$$\omega(\xi) = k_i\left(\xi - \xi_{i,0}\right)^2 \qquad \textbf{Eq. I-6}$$

In **Eq. I-6**, k_i defines the force constant that restricts the centre of the window i to the equilibrium position $\xi_{i,0}$. The overlap of sampling in adjacent windows is a crucial requirement for the calculation of the PMF, thus imposing a fine-tuning of the force constant and distance between windows for this purpose. The PMF is then calculated by combining the data from the different windows, with proper reweighting, and unbiased, as explained further below.[73] The two above-mentioned variables have a direct effect upon the probability distribution $P_i^b(\xi)$ of the biased system, usually attained through binning methods to generate a histogram. The PMF along the reaction coordinate (biased system) and for individual windows (unbiased system) are given by **Eq. I-7** and **Eq. I-8**, respectively.

$$A_i^b(\xi) = -\frac{1}{\beta}\ln\ P_i^b(\xi) \qquad \textbf{Eq. I-7}$$

$$A_i^u(\xi) = -\frac{1}{\beta}\ln P_i^b(\xi) - w_i(\xi) + F_i \qquad \textbf{Eq. I-8}$$

Where F_i constant varies between windows or biasing potentials,[77] is independent of ξ,[73] and cannot be directly attained from sampling.

Variational Free Energy Profile (vFEP)[78] was the preferred methodology for the reconstruction of the PMF of the synthetic transporters' transmembrane diffusion in this thesis.

I.3.2.1. Variational Free Energy Profile

A wide variety of methods have been developed to obtain free energy profiles from MD simulations, such as multistate Bennet acceptance ratio method (MBAR), umbrella integration (UI), weighted histogram analysis method (WHAM) and its unbinned derivate (UWHAM), and the vFEP method.[79] The vFEP is a methodology to attain an unbiased free energy surface/profile (FES) from a set of umbrella window simulations, biased by energetic restraints.[78, 79] Like the other methods, vFEP constructs an analytical representation of the global unbiased FES from the umbrella biasing potentials (restraints) and the time series of observed reaction coordinate values for each window.[79] Some important advantages mark a clear distinction between vFEP and the remaining methods, such as the ability to provide a robust analytical representation of the free energy profile with a smaller number of samples.[79]

I.3.3. MD simulation of phospholipid bilayers

MD simulations can currently model a wide variety of lipids, including saturated and unsaturated hydrocarbon chains, various head groups, sterols, and lipid linkages between the glycerol backbone and tail. These simulations often include membrane-bound proteins, peptides, ions, and a water model.[80]

Although membrane structure has been widely studied experimentally via X-ray and neutron scattering, IR/Raman, or NMR spectroscopy, resolution to the atomistic level can only be obtained by MD simulations. Its validity, however, is highly dependent of the potential energy function or force field that is used.[81] The need for a force field able to correctly describe bond distances, angles, and dihedral states, along with the intermolecular interactions required for the formation of self-assembled structures, instigated the development of lipid specific force fields in the recent years.[80, 81] **Table I-1** lists force fields that have been developed along the last decade.

Table I-1. Common lipid force fields used in MD simulations of lipids, from 2010 onwards.

Type	Force Field	Lipids
All-atom	CHARMM36 (2010)	DLPC, DMPC, DPPC, DOPC, POPC and POPE[82]
	GAFFLipid (2012)	DLPC, DMPC, DPPC, DOPC, POPC and POPE[83]
	SLipid (2012, 2013)	DOPC, POPC, SOPC, DLPE, DPPE, DOPE, POPE,[84] DLPG, DMPG, DPPG, DSPG, DOPG, POPG, DOPS, 16:0 SM and 18:0 SM[85]
	Lipid14 (2014)	DLPC, DMPC, DPPC, DOPC, POPC, POPE[81] and cholesterol[86]
	OPLS-AA (2014)	DPPC,[87, 88] POPC, DOPC, PEPC, and cholesterol[88]
United atom	TraPPE-UA (2013)	DPPC, DMPC, DLPC, DOPC, DOPS, DOPG, DMPG, DLPG, POPC and POPE[89]
	C36-UA (2014)	DMPC, DPPC, DOPC, POPC and cholesterol[90]
Coarse-grained	SDK (2010)	DPC, DMPC, DPPC, POPC and POPE[91]
	Dry MARTINI (2015)	POPC, DPPC, DMPC, DOPC, DLiPC, DOPE and cholesterol[92]
Polarisable	Drude (2013)	DPPC[69]

Regarding AMBER family force fields, despite GAFF being initially used to parameterize phospholipids in very specific cases,[80, 84, 93] only after a concerted effort of AMBER researchers, with the development of Lipid11 and GAFFLipid, it was possible to develop Lipid14,[81] a robust force field for lipid simulations that supports up to 32 different types of lipids, using combinations of parameterised fragments, developed for the lipids presented in **Scheme I-5**.[80, 81] Moreover. Lipid14 was able to reproduce the assembly of lipid bilayers from phospholipids randomly distributed in aqueous solution.[94] Previously, this was only available in less specific force field types, like united atoms or coarse-grained. Further parameterization work was carried out on negatively charged phospholipids head groups, which are now also supported in the recent Lipid17.[95] Noterworthy, these force fields are available in the AMBER package, [96-98] which permits the use of GPU acceleration to significantly increase the simulation's performance.[99, 100]

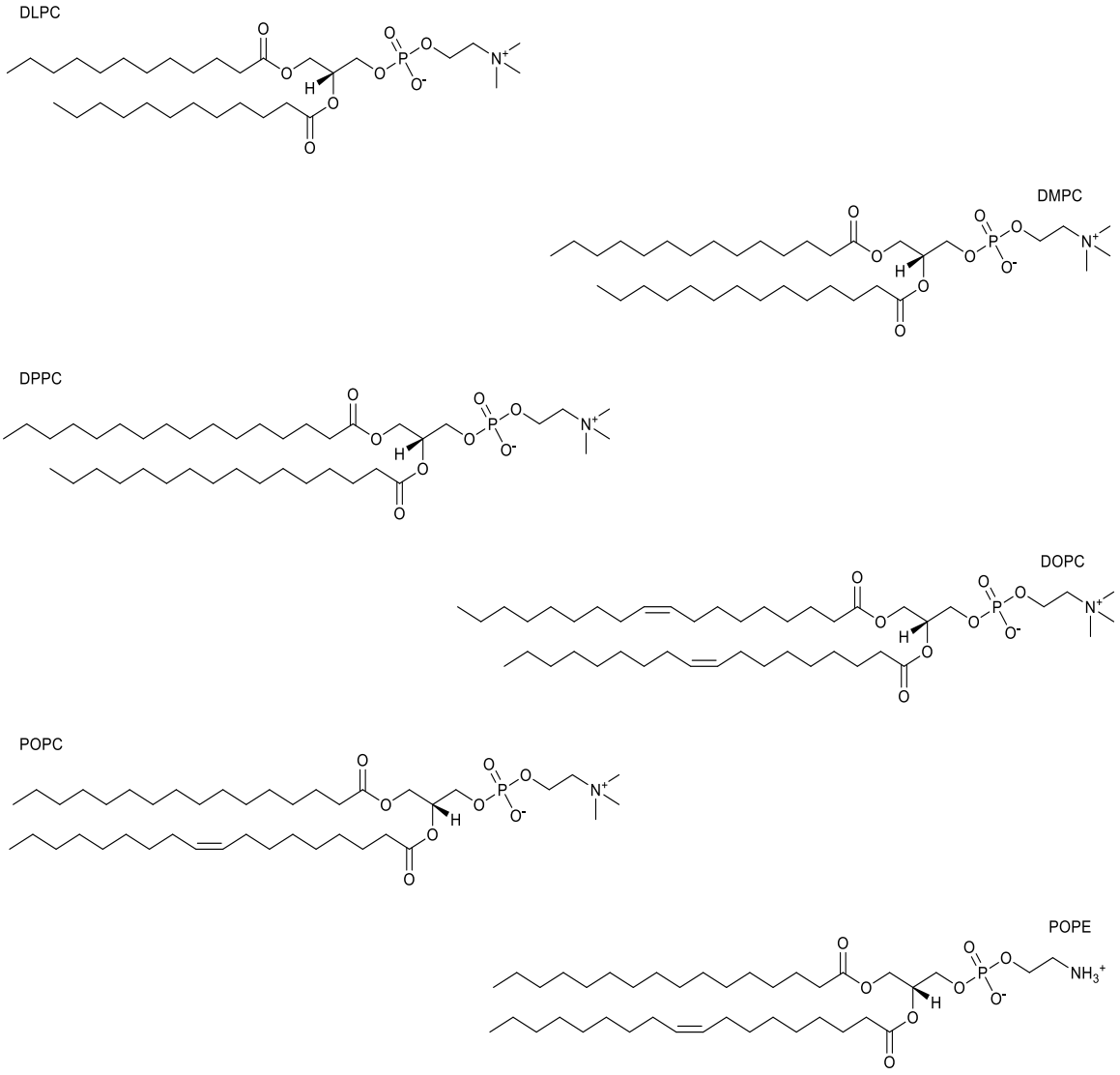

Scheme I-5. Six examples of phospholipids supported by Lipid14 force field.[81]

Finally, the simulated phospholipid bilayer must be validated according to experimental data. Structural properties like area per lipid, volume per lipid and bilayer thickness can be ascertained from MD simulations and compared with reference values, which give a good indication of whether the bilayer is in the correct phase at a given temperature.[81] The relative orientation of the acyl chain with respect to the bilayer normal may be determined by calculation of the order parameters (S_{CD}) and compared with the experimental NMR values.[81] Lastly, electron density profiles and scattering form factors can also be compared with experimental data to validate the results of the membrane simulation.[81]

Objectives

As the most lethal genetic disease in Caucasian population, it is of utmost importance, the development of a therapy that tackles not only specific mutations, but instead acts as a generalized viable solution for CF and other chloride channelopathies' patients. As such, this work focuses on a comprehensive theoretical study on the anion transport promoted by synthetic transmembrane transporters, as follows:

- Characterise the interaction between the synthetic anionophores and the phospholipid bilayers, at the atomistic level.
- Investigate the mechanisms of chloride transport by the transporters, together with the role of the acylhydrazone binding units.
- Evaluate the impact of the synthetic transporters' permeation with the lipid bilayer.

Finally, achieving the proposed objectives will grant a useful insight on the behaviour and properties of synthetic transporters with additional hydrazone-based functional groups, and allow for the development of more efficient anion transporters and potential channel replacement therapies.

The work reported in this thesis was developed within the scope of a collaboration between Professor Vitor Félix's Molecular Modelling and Computational Biophysics group (University of Aveiro) and Doctor Hennie Valkenier's Engineering of Molecular NanoSystems group (Université Libre de Bruxelles). The computational and the experimental work is already published as: L. Martinez-Crespo, L. Halgreen, M. Soares, I. Marques, V. Félix and H. Valkenier, *Org Biomol Chem*, **2021**, DOI: 10.1039/d1ob01279g.

Chapter II.

Hydrazone-based molecules as anion receptors: molecular modelling by DFT calculations

Summary

Over the last decades, channelopathies like CF have motivated the development of synthetic carriers for anion transport. The design of these molecules depends on a wide variety of factors, like the balance between the lipophilicity and binding affinity of the receptor. The binding affinity of thiourea-based synthetic anion receptors (**Scheme II-1**) for chloride were ascertained through DFT calculations performed at the PBE0-D3(C-PCM$_{DMSO}$)/Def2-TVZP theory level. The results of this comprehensive study are described in this chapter. It is demonstrated that receptors' multiple binding motifs, behave independently, with the thiourea one having a stronger binding ability for chloride when compared to the hydrazone binding unit.

II.1. Introduction

Recent studies on synthetic ion receptors gave considerable insights on the main structural properties that impact the activity of artificial receptors. These transporters can be either channels, spanning the entire membrane and permitting the efflux of ions, or mobile carriers, that facilitate the diffusion of ions throughout the bilayer by associating with the ion on one side of the membrane and releasing it on the other side.[101] A common strategy to obtain efficient anion mobile carriers is by developing receptors ureas, thioureas, and squaramides, which possess two polar N−H units able to bind chloride through convergent hydrogen bonding interactions.[102] Additionally, the synthetic receptors must be lipophilic enough to remain inside the bilayer and to form anion-receptor complexes able to diffuse through the membrane's hydrophobic core.[103-105] Very efficient mobile carriers often contain multiple urea or thiourea binding units organized in rigid structures that bind a single anion in a cooperative fashion, with the formation 1:1 complexes with high stability.[106-108] Furthermore, groups with acidic hydrogens, such as amides, sulphonamides, protonated imines, and pyrrole and indole rings, and even C−H units from benzo[b]thiophenes have been also combined in the development of efficient transporters with multiple binding units for anion recognition.[109-113]

Acylhydrazones are characterised by a polar N−H amide group, able to coordinate anions, adjacent to imine and carbonyl functional groups, and can be used in dynamic combinatorial libraries (DCL)[114-116] for the design of structurally complex anion receptors. Additionally, hydrazones can be conformationally manipulated with resort to photosensitivity or metalation.[117-119] A family of phenylthiosemicarbazones structurally related to acylhydrazones and thioureas have been reported as pH dependent chloride transporters.[120] However, the efficient binding and transport of the chloride anion was reliant on the protonation of the thiosemicarbazone group, limiting the interest on the development of complex transporters with multiple dynamic bonds. To the best of our knowledge, it is the first time acylhydrazone binding groups are used in the development of synthetic anion carriers.

The chloride binding affinity of mono-thioureas derivatives (**1**-**8**), acylhydrazone (**9**) and a bis-thiourea (**10**), presented in **Scheme II-1**, were experimentally assessed by ^{1}H-NMR titrations. The anion binding abilities of these molecules will be rationalised

throughout this chapter, with resort to DFT calculations and several quantum descriptors (*vide infra*).

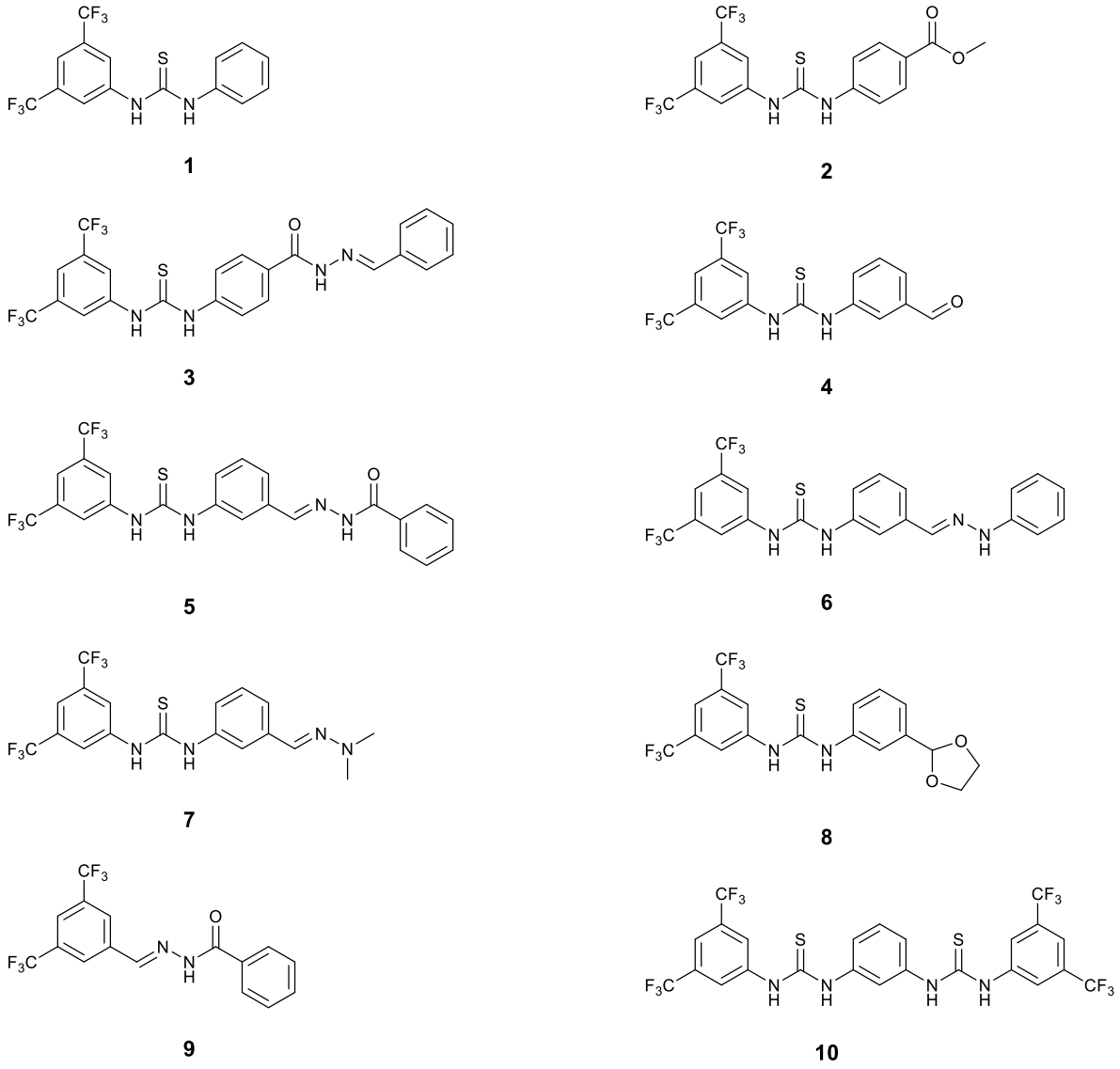

Scheme II-1

The chloride binding properties of receptors **1-10** were assessed by ^{1}H-NMR (typical protons of interest are illustrated for **5** in **Scheme II-2**) titrations with tetrabutylammonium chloride (TBACl) in dimethyl sulfoxide (DMSO) with 0.5% of H_2O.[121] The binding constants (K_a) were computed by fitting the experimental data to 1:1

or 1:2 receptor:anion models (see **Table II-1**).[121] Mono-thioureas **1-8** presented comparable binding constants for the 1:1 stoichiometry model (K_{11} ranging from 27 to 44 M^{-1}, *vide infra*). However, the acylhydrazone derivative **9**, with a single binding unit, showed an association constant one order of magnitude lower (K_{11} = 3.5 M^{-1}). Moreover, due to the rigidity of compound **10**, the titration data was directly fitted to the 1:2 model with each thiourea binding a chloride. The values of the K_{11} and K_{12}, are slightly higher than those for the hydrazone thiourea derivatives **3**, **5** and **6**.

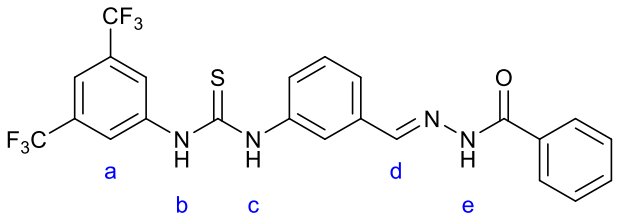

5

Scheme II-2

Table II-1. Lipophilicity (log P values), chloride binding constants (K_a), intravesicular chloride at 300 s ($[Cl]^-_{in}$ at 300 s), and relative chloride transport activity (RTA) of receptors **1-10**. Adapted from reference [122].

Molecule	Log P[a]	K_a (Cl^-) (M^{-1})[b]			$[Cl^-]_{in}$ at 300 s (mM)	RTA[c]
		1:1 model	1:2 model			
		K_{11} (M^{-1})	K_{11} (M^{-1})	K_{12} (M^{-1})		
1	5.5	31	–	–	23.5	Good
2	5.3	42	–	–	24.8	Good
3	6.8	–	44	7	0.8	Poor
4	5.2	37	–	–	24.7	Good
5	6.8	–	30	4	1.4	Poor
6	6.9	–	24	5	2.5	Poor
7	5.5	32	–	–	11.9	Moderate
8	5.3	32	–	–	8.9	Moderate
9	5.2	4	–	–	0.6	Poor
10	9.0	–	49	10	1.0	Poor

[a)] Values attained from ChemDraw 20.1.
[b)] Determined by ^{1}H-NMR titration in DMSO-d6:H_2O 99.5:0.5.
[c)] Relative Cl^- transport activity.

II.2. Methods

The structures of molecules **1**-**10** used in the quantum calculations were either directly obtained from the Cambridge Structural Database (CSD),[123] or produced by atomic manipulation of suitable X-ray single crystal structures of analogous compounds.

All quantum calculations were performed with Gaussian 16.[124] The chloride complexes **1**-**10**, as well as the corresponding free receptors, were geometry optimised by DFT with the PBE-0 functional, using Grimme's D3 empirical correction for dispersion,[125] along with the Def2-TZVP basis set. Additionally, to mimic the DMSO solvation effects, the Conductor-like Polarizable Continuum Model (C-PCM)[126, 127] was employed. Receptors with a single binding unit, such as **1**, **2**, **4**, **7**, and **8** were optimised with a chloride bonded to the thiourea moiety, or to the acylhydrazone in the case of **9**. In contrast, receptors **3**, **5**, **6**, and **10** were optimised with a chloride in each binding unit, in agreement with the 1:2 receptor:anion stoichiometry in line with the ^{1}H-NMR titration results . The optimised structures were found to correspond to relative minima, as no imaginary frequencies were found for the achieved geometries.

The energetic data were computed directly from the structures of the complexes, free receptors, and anion, DFT optimised in C-PCM DMSO model. The interaction energy (ΔE), given by $\Delta E = E_{complex} - (E_{receptor} + E_{anion})$, with $E_{complex}$, $E_{receptor}$ and E_{anion}, corresponds to the electronic energies of the optimised geometries of the complex, receptor and anion, including the Zero-Point Energies (ZPE) and Thermal corrections for 298.15 K.

The distribution of electrostatic potential (V_S) of **1**-**10** was assessed via single point energy calculations on the receptor's binding conformation within the complex (*i.e.*, the receptors' geometry upon anion(s) removal), at the same level of theory. The electrostatic potential created by the receptor's nuclei and electrons, at any given point r, is given by $V(r)$:

$$V(r) = \sum_{A} \frac{Z_A}{|R_A - r|} - \int \frac{\rho(r')\,dr'}{|r' - r|} \qquad \textbf{Eq. II-1}$$

where $\rho(r')$ is the electronic density of the receptor, and Z_A the charge of nucleus A located at R_A. The distribution of V_S was subsequently evaluated on the 0.001 electrons Bohr^{-3} molecular surface of each receptor, and its surface points (*e.g.*, $V_{S,max}$, the maxima) were obtained with resort to Multiwfn.[128]

The energy of the hydrogen bonding interactions between receptors **1**-**10** and chloride ions, in 1:1 or 1:2 binding stoichiometries, was calculated via the Quantum Theory of Atoms In Molecules (QTAIM)[129] analysis, using Multiwfn.[128] In this approach, topological curvature descriptors of density, along a given spatial position **r**, allow to locate a continuous bond path BP(r) between two distinct atoms A and B. In particular, the electron density along this bond path descends abruptly from each nucleus towards a distinctive bond critical point.[130] Moreover, the strength of these intermolecular interactions was also assessed via Natural Bond Orbital (NBO) analysis,[131] using NBO6,[132] in which transformed molecular orbitals are computed to arrange the ideal Lewis structure of a given molecule. This methodology grants insights regarding the interaction between donor Lewis type NBOs (bonding or lone pair), and acceptor non-Lewis NBOs (antibonding or Rydberg). The interaction energy between the acceptor and the donor in the NBOs was evaluated through Fock matrix's second-order perturbation theory analysis,[133] ascertaining the interaction strength. The stabilization energy E^2 is related to the delocalization between the donor (i) and acceptor (j) orbitals, given by

$$E^2 = \Delta E_{ij} = q_i \frac{{F_{(i,j)}}^2}{\varepsilon_i - \varepsilon_j} \qquad \textbf{Eq. II-2}$$

with q_i representing the donor orbital occupancy, $F_{(i,j)}$ the Fock matrix elements, and ε_i and ε_j the orbital energies.

II.3. Results and Discussion

The DFT geometry optimization of chloride complexes **1**-**10** provided useful insights of their anion binding affinity. The computed structures of 1:1 chloride complexes **1**-**9** are presented in **Figure II-1** while the optimised structures of 1:2 complexes are shown in **Figure II-2**.

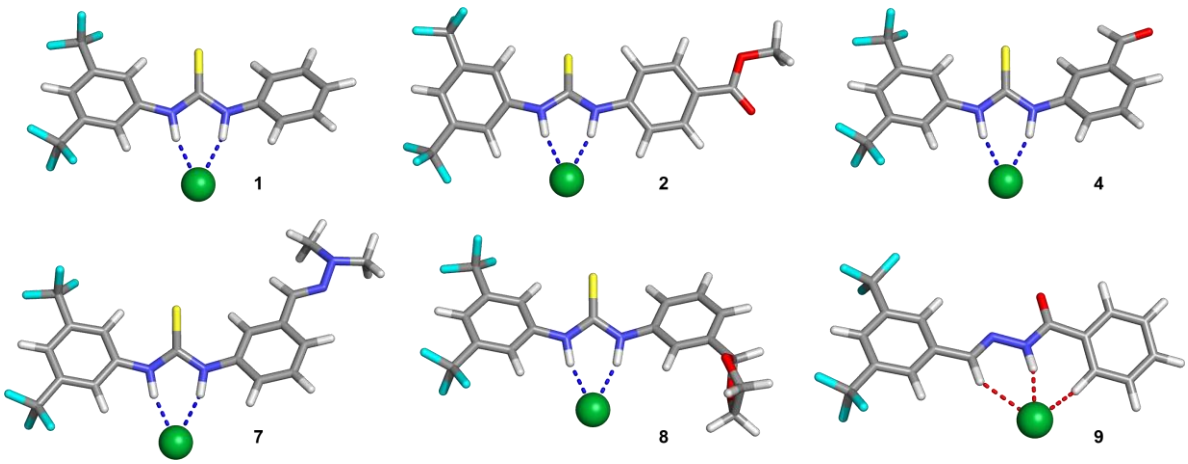

Figure II-1. DFT-optimized structures of the 1:1 chloride complexes **1**, **2**, **4**, **7**, **8**, and **9**. The N−H···Cl⁻ hydrogen bonds at the thiourea binding sites are drawn in blue, while the N−H···Cl⁻ and C−H···Cl⁻ interactions at the acylhydrazone binding unit are drawn in red.

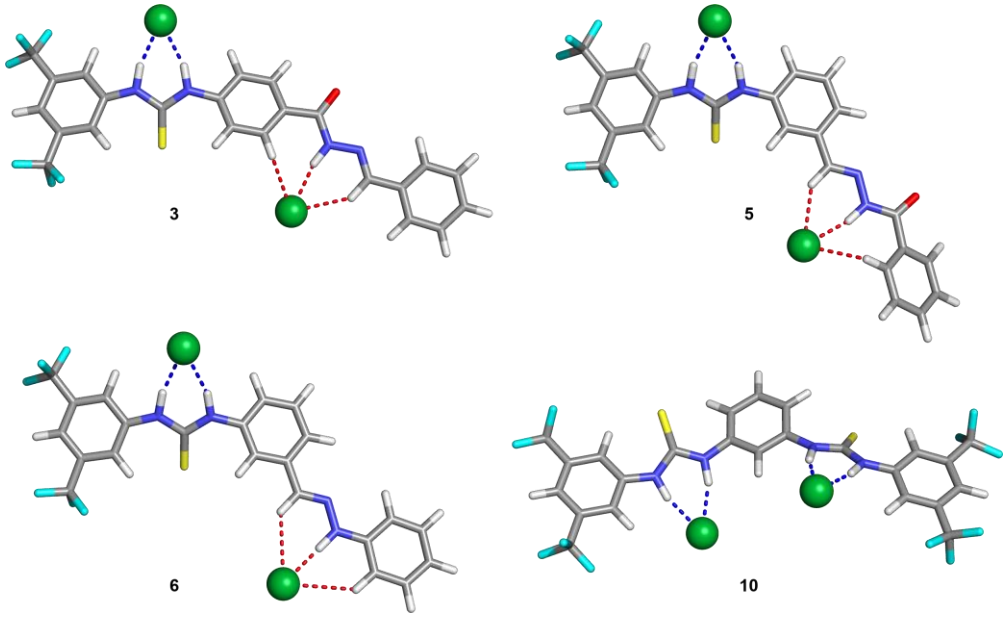

Figure II-2. DFT-optimized structures of the 1:2 chloride complexes of **3**, **5**, **6**, and **10**. Remaining details as given in **Figure II-1**.

The computed dimensions of the N−H···Cl⁻ and C−H···Cl⁻ hydrogen bonds in the optimised chloride complexes are gathered in **Table II-2**. Overall, the thiourea N···Cl⁻ distances and N−H···Cl⁻ angles, ranging between 3.15 and 3.20 Å and 161.6 and 165.3°, are comparable in associations of **1-8** and **10**. However, following the variations of the

resonances of protons *b* and *c* (**Scheme II-2**), observed along the ^{1}H-NMR titrations,[121] the distances computed between the N−H_b thiourea binding motif contiguous to the fluorinated ring and chloride are slightly shorter (*ca*. 0.04 Å) than the second thiourea binding unit (N−H_c), indicating that these two convergent hydrogen bonds have different binding strengths, as demonstrated further below, mainly through the QTAIM analysis.

In the isomeric complexes **3**, **5** and **9**, the chloride binding by the acylhydrazone motif mainly occurs through a N−H···Cl^- hydrogen bond (proton *e* in **Scheme II-2**), assisted by two convergent C−H···Cl^- supramolecular contacts established by the hydrazone proton (C_{hyd}-H, proton *d* in **Scheme II-2**) and by an aromatic proton (C_{ar}−H) adjacent to the acyl group (see **Figure II-1** and **Figure II-2**). The N−H···Cl^- hydrogen bonds display shorter distances and more linear angles than the C_{hyd}−H···Cl^- ones (3.26 ± 0.01 *vs*. 3.57 ± 0.01 Å and 166.5 ± 0.4 *vs*. 144.3 ± 0.5°, see **Table II-2**), demonstrating stronger hydrogen bonds, consistent with the variations on the chemical shifts of receptor **5**'s protons *e* and *d*, depicted in **Scheme II-2**.[121] In contrast, the dimensions of the C_{ar}−H···Cl^- hydrogen bonds (3.59 ± 0.01 Å and 142.9 ± 3.0°) present a similar bond strength to the C_{hyd}−H···Cl^- ones. Finally, while the N−H arylhydrazone binding unit of **6** has a binding strength equivalent to the acylhydrazone analogous, the C−H groups point to the anion at larger distances (*ca*. 0.3 Å), reflecting the absence of the acyl group electron-withdrawing effect.

Table II-2. Hydrogen bond dimensions (distance in Å; angles in °) for the N−H···Cl^- interactions in the thiourea binding site and for the N−H···Cl^-, C_{hyd}−H···Cl^- and C_{ar}−H···Cl^- interactions in the hydrazone moieties, computed from the DFT optimised structures.

Molecule	Stoichiometry	Thiourea		Hydrazone		
		N−H$_b$	*N−H$_c$*	*N−H$_e$*	*C$_{hyd}$−H*	*C$_{ar}$−H*
1	1:1	3.152; 164.9	3.195; 161.9	-	-	-
2	1:1	3.147; 164.8	3.180; 163.2	-	-	-
3	1:2	3.147; 165.1	3.191; 162.4	3.274; 166.5	3.584; 144.8	3.585; 145.4
4	1:1	3.149; 164.6	3.181; 161.9	-	-	-
5	1:2	3.152; 164.7	3.194; 161.7	3.259; 167.0	3.583; 144.5	3.586; 138.7
6	1:2	3.150; 165.3	3.201; 161.6	3.212; 179.2	3.890; 134.8	3.935; 135.0
7	1:1	3.151; 165.2	3.200; 161.6	-	-	-
8	1:1	3.157; 164.4	3.186; 162.3	-	-	-
9	1:1	-	-	3.248; 165.9	3.554; 143.6;	3.593; 144.6
10	1:2	3.151; 165.3[a]	3.193; 162.0[a]	-	-	-

[a)] The same distances and angles were observed in both binding units.

Having established the structures of the receptors in the chloride complexes, the distribution of electrostatic potential plotted onto their electron density surface (V_S) allowed to ascertain the binding ability of receptors **1-10**. The distribution of V_S is depicted in **Figure II-3** and **Figure II-4**, with the most relevant values of V_S gathered in **Table II-3**.

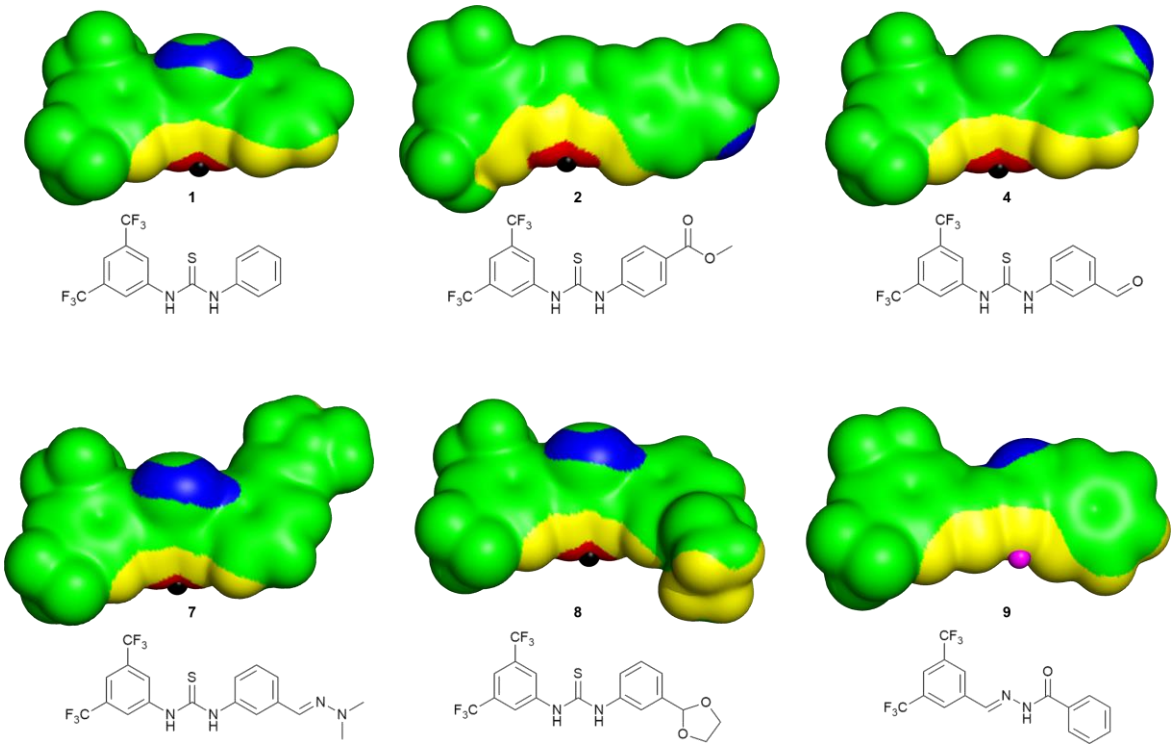

Figure II-3. Distributions of the electrostatic potential of **1**, **2**, **4**, **7**, **8**, and **9**, mapped on their molecular surfaces (0.001 e Bohr^{-1} contour). The surface colour ranges from -30 (blue) to 70 kcal mol^{-1} (red). The location of the $\boldsymbol{V_{S,max}}$ in front of the thioureas is shown with a black sphere, while the location of the highest value of $\boldsymbol{V_S}$ in front of the acylhydrazone is show with a pink one. Corresponding structures are presented below.

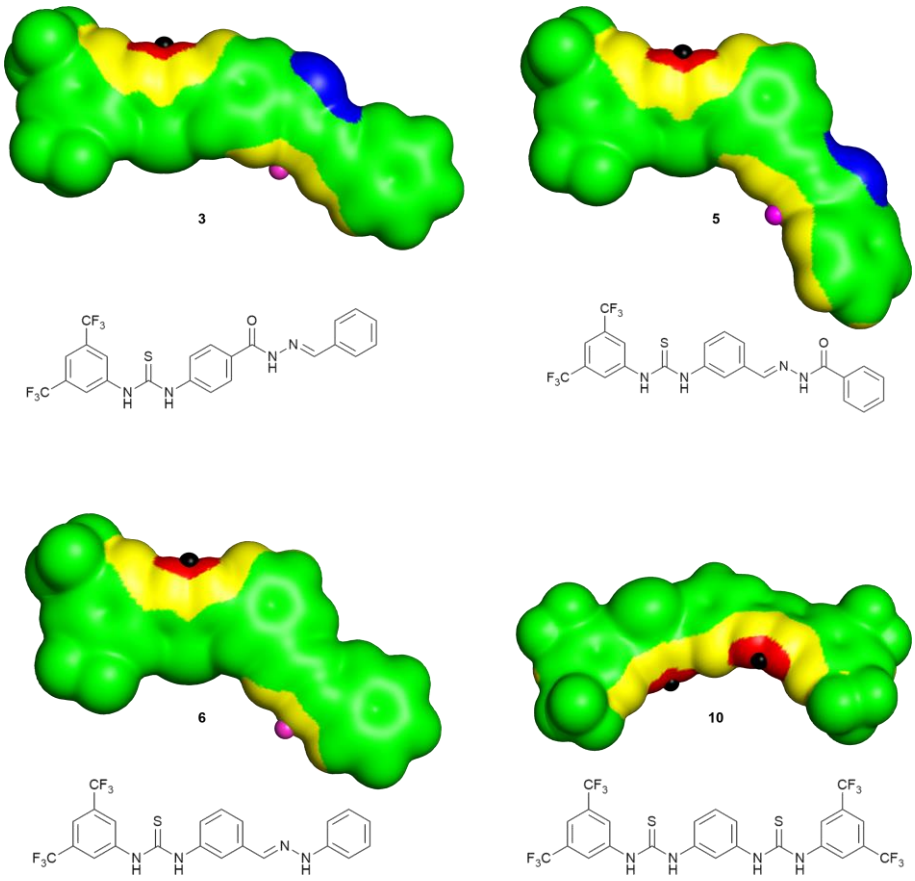

Figure II-4. Distributions of the electrostatic potential of **3**, **5**, **6**, and **10**. Remaining details are given in **Figure II-3**.

Table II-3. Relevant electrostatic potential values (V_S, kcal mol^{-1}) computed on the electron density surface of the thiourea and hydrazone binding units.

Molecule	Thiourea	Hydrazone		
	V_S	V_S		
	N−H	N−H$_e$	C$_{hyd}$−H	C$_{ar}$−H
1	91.7	-	-	-
2	97.0	-	-	-
3	96.7	61.1	53.6	54.9
4	99.3	-	-	-
5	95.4	60.0	52.8	54.1
6	92.9	51.0	42.7	41.7
7	89.7	-	-	-
8	90.0	-	-	-
9	-	71.5	65.2	64.5
10	100.3[a]	-	-	-

[a)] The V_S values for the two thiourea N−H binding units are undistinguishable.

Overall, the thiourea binding units of receptors **1-8** and **10** are enclosed in red areas of highly positive potential and with the most positive value of V_S ($V_{S,max}$) located in front of the N−H binding sites, as depicted in **Figure II-3** and **Figure II-4** by one (**1-8**) or two (**10**) black spheres. The $V_{S,max}$ values range between 89.7 kcal mol^{-1} for the *N*,*N*-dimethyl-hydrazone derivative **7** and 100.3 kcal mol^{-1} for **10**, with both thiourea motifs adjacent to a 3,5-bis(trifluoromethyl)phenyl electron withdrawing group. The hydrazone moieties of **3** and **5** are characterised by comparable values of V_S for the N−H binding sites (*ca*. 60 kcal mol^{-1}), and similar values of V_S for the C$_{hyd}$−H (*ca*. 53 kcal mol^{-1}) and C$_{ar}$−H (*ca*. 54 kcal mol^{-1}) binding sites. The replacement of a benzoyl fragment by an arylhydrazone leads to a significant decrease of V_S of the hydrazone binding motif, as given by the comparison between the values of **6** for N−H (51.0 kcal mol^{-1}), C$_{hyd}$−H (42.7 kcal mol^{-1}) and C$_{ar}$−H (41.7 kcal mol^{-1}) with the ones calculated for **3** and **5**. Receptor **9**, having the 3,5-bis(trifluoromethyl)phenyl and benzoyl electron-withdrawing groups, linked by an hydrazone bridge, naturally displays the highest V_S values for the N−H, C$_{hyd}$−H and C$_{ar}$−H binding sites of 71.5, 65.2 and 64.5 kcal mol^{-1}, respectively. This electrostatic potential analysis suggests a higher binding affinity of thiourea for chloride, although the V_S values estimated for the hydrazone binding units are consistent with the existence of 1:2 chloride species, as suggested by the fitting models assessed from the ^{1}H-NMR titration binding data.[121]

The energy of the hydrogen bonds (E_{HB}) interactions between **1**-**10** and Cl^- were evaluated using QTAIM as E_{HB} = ½V, with V being the potential energy of the critical point located between the hydrogen donor (N−H, C_{hyd}−H or C_{ar}−H binding site) and the anionic hydrogen acceptor. Alternatively, in the NBO approach, the strength of N−H···Cl^- and C−H···Cl^- hydrogen bonds were assessed through the second-order perturbation theory, with the E^2 values corresponding to the stabilisation energies between the antibonding orbitals of the N−H or C−H binding units (Ω^*_{N-H} or Ω^*_{C-H}) and the lone pair orbitals of Cl^- (n_{Cl^-}). The E_{HB} and E^2 energy values are gathered in **Table II-4**. These values follow a nearly linear relation (R^2 = 0.97), demonstrating the complementarity of both analyses for the chloride complexes **1**-**10**, despite the differing characterisations. Thus, the following discussion will be focused only on the E_{HB} energies.

Table II-4. Energy of the hydrogen bonds (E_{HB}, kcal mol^{-1}) at the bond critical points in the N−H···Cl^- or C−H···Cl^- interactions between the thiourea or hydrazone binding units and chloride, together with the E^2 stabilisation energies (kcal mol^{-1}), between the antibonding orbitals of the N−H or C−H binding units (Ω^*_{N-H} or Ω^*_{C-H}) and the lone pair orbitals of Cl^- (n_{Cl^-}).

Molecule	Thiourea				Hydrazone					
	E_{HB}		E^2		E_{HB}			E^2		
	N−H_b	N−H_c	N−H_b	N−H_c	N−H_e	C_{hyd}−H	C_{ar}−H	N−H_e	C_{hyd}−H	C_{ar}−H
1	-6.5	-5.4	20.8	16.4	-	-	-	-	-	-
2	-6.6	-5.8	21.2	18.2	-	-	-	-	-	-
3	-6.6	-5.5	21.3	17.0	-4.2	-2.0	-2.0	15.6	3.5	2.3
4	-6.5	-5.7	21.0	17.4	-	-	-	-	-	-
5	-6.5	-5.4	20.7	16.4	-4.5	-2.0	-1.8	16.8	3.5	1.6
6	-6.5	-5.3	21.1	15.9	-5.5	-0.9	-0.8	20.4	0.8	0.5
7	-6.5	-5.3	21.0	15.9	-	-	-	-	-	-
8	-6.3	-5.6	20.2	17.2	-	-	-	-	-	-
9	-	-	-	-	-4.6	-2.0	-1.9	17.2	3.7	2.1
10	-6.5[a]	-5.4[a]	21.1[a]	16.5[a]	-	-	-	-	-	-

[a] The thiourea binding units are undistinguishable.

In agreement with the computed hydrogen bonding dimensions for **1**-**8** and **10**, the thiourea's N−H_b, contiguous to the fluorinated ring, has the strongest interaction with chloride, followed by the N−H_c moiety, with average E_{HB} values of -6.5 and -5.5 kcal mol^{-1}, respectively. The chloride recognition by the acylhydrazone binding unit in receptors **3**, **5** and **9** is primarily driven by the N−H binding site, with a lower E_{HB} of -4.4

kcal mol^{-1}, with the C_{hyd}–H and C_{ar}–H binding units, respectively contributing only with -2.0 and -1.9 kcal mol^{-1}. The arylhydrazone motif in **6**, presented slightly higher E_{HB} for the N–H site (-5.5 kcal mol^{-1}), but marginal contributions from the C_{hyd}–H and C_{ar}–H binding units, with E_{HB} values around -1.0 kcal mol^{-1}. Thus, the global E_{HB} contributions at the thiourea binding unit amount to *ca*. -12.0 kcal mol^{-1}, followed by the acylhydrazones with *ca*. -8.3 kcal mol^{-1} and by the hydrazone binding unit in **6** with a global E_{HB} of *ca*. -7.3 kcal mol^{-1}, in line with the thiourea's binding unit experimental higher binding affinity for chloride. Noteworthy, the molecules with only a thiourea binding motif (**1**, **2**, **4**, and **7**, **8**), display a straightforward relation between the computed E_{HB} values and the experimental K_a values (R^2 = 0.95), regardless of their low values.

The interaction binding energies between receptors **1**-**10** and chloride were determined by $\Delta E = E_{Com} - (E_{Rec} + E_{Lig})$ (*vide supra*), as a global binding quantum descriptor. E_{Com} was obtained from the above-mentioned DFT optimised structures, E_{Lig} was obtained from a free chloride, and E_{Rec} was obtained by the removal of the anions from each chloride complex, followed by the optimisation of the free receptor. Moreover, for **3**, **5**, and **6**, to establish the independent contributions of the thiourea and hydrazone-based binding sites, two alternative binding scenarios with a 1:1 stoichiometry were optimised: *A*, with the thiourea hydrogen bonded to a chloride, or *B*, with the anion recognized by the acylhydrazone (**3** and **5**) or arylhydrazone binding motif (**6**). For **10**, only the *A* 1:1 additional scenario was necessary. The ΔE values determined for all anion associations are gathered in **Table II-5**. The average interaction energy ascertained for **1**-**2**, **4**, and **7**-**8** is *ca*. -14.4 kcal mol^{-1}, close to the value computed for the complexes of **3**, **5**, **6** and **10** in scenario *A*, with an average ΔE of -14.5 kcal mol^{-1}. In contrast, the interaction between the chloride and the acylhydrazone motif (scenario *B*) in **3** and **5**, results in ΔE values of *ca*. -8.3 kcal mol^{-1}, in agreement with the -8.7 kcal mol^{-1} assessed for **9**, with a single acylhydrazone binding unit. The arylhydrazone **6** presented a slightly lower ΔE of -7.2 kcal mol^{-1}. The sum of the individual energy contributions for the hydrazone derivatives **3**, **5**, **6** (scenarios *A* + *B*) and the bis-thiourea **10** (scenario *A* × *2*) leads to ΔE values comparable to those computed for the corresponding 1:2 associations, with an offset of *ca*. 1.0 kcal mol^{-1}. These energetic findings indicate that the thiourea and hydrazone binding motifs in **3**, **5**, **6**, and both thiourea motifs in **10**, recognise chloride non-cooperatively.

Table II-5. Uncorrected electronic binding energies ($\boldsymbol{\Delta\mathcal{E}_0}$), Zero-Point Corrections ($\boldsymbol{\Delta ZPE}$) and thermal corrected binding energies ($\boldsymbol{\Delta E}$), in kcal mol^{-1}, for the chloride complexes of **1**-**10**.

Molecule	Stoichiometry	Binding site	$\Delta\mathcal{E}_0$	ΔZPE	ΔE
1	1:1		-14.8	0.3	-14.2
2	1:1		-15.5	0.2	-14.9
3	1:2		-23.4	0.5	-22.1
3	1:1	thiourea	-15.4	0.2	-14.9
3	1:1	acylhydrazone	-9.0	0.3	-8.3
4	1:1		-15.2	0.2	-14.7
5	1:2		-23.0	0.5	-21.7
5	1:1	thiourea	-15.0	0.2	-14.4
5	1:1	acylhydrazone	-9.1	0.4	-8.3
6	1:2		-21.8	0.5	-20.4
6	1:1	thiourea	-14.8	0.3	-14.2
6	1:1	arylhydrazone	-7.9	0.3	-7.2
7	1:1		-14.7	0.3	-14.0
8	1:1		-14.9	0.2	-14.3
9	1:1		-9.5	0.3	-8.7
10	1:2		-29.1	0.4	-28.0
10	1:1	thiourea	-15.1	0.2	-14.5

II.4. Conclusions

Overall, the DFT calculations show a superior binding affinity of the thiourea binding unit for chloride, although the electrostatic potential values for the hydrazone motifs corroborate the existence of 1:2 receptor:chloride species, as indicated by the ^{1}H-NMR binding data. Through the QTAIM, NBO and energetic analyses, the DFT calculations also demonstrated that the binding units in receptors **3**, **5**, **6** and **10** recognized chloride in a non-cooperative independent manner.

Chapter III.

Passive diffusion of hydrazone-based receptors across phospholipid bilayers: a molecular dynamics simulation investigation

Summary

Having established the structures of the different chloride complexes, and ascertained the receptors' binding properties, this chapter focuses on the transport properties of **1**-**10**. According to the experimental chloride efflux studies approached in the previous chapter, the additional binding motif results in a decreased transport ability. Hence, it was suggested that the additional interactions with the membrane phospholipids, caused by the secondary binding site in receptors **3**, **5**, **6** and **10**, hinder the chloride transmembrane transport. In agreement, MD simulations show that the receptors position themselves below the water/lipid interface, driven by the interaction of the thiourea and of the acylhydrazone motifs with the phosphate head groups and water molecules. Additionally, the interaction energies calculated through MM demonstrate that the transporters with poorer transport capabilities have stronger interactions with the membrane phospholipids. Thus, the impact of the hydrazone functional groups on the transport ability was confirmed, and it is important to consider this kind of effect when designing new synthetic ionophores.

III.1. Introduction

The chloride transport properties of receptors **1-10** were experimentally assessed using the well-established lucigenin assay as follows: The POPC and cholesterol (7:3 ratio) large unilamelar vesicles (LUVs) were prepared with an encapsulated chloride sensitive dye (lucigenin).[121] The chloride influx was monitored *via* the quenching of the lucigenin's fluorescence over time. The chloride efflux into the vesicles was assumed to be compensated by the transport of NO_3^- out of the vesicles, maintaining the membrane potential (Cl^-/NO_3^- antiport).[121]

Compounds **1-10** were studied at a 1:100 transporter to lipid molar ratio (1 mol%), resulting in the transport ability presented in **Table II-1**. In these conditions, mono-thiourea **1** presented a good transport activity, whilst acylhydrazone **9** was almost inactive.[121] Although the functional groups of **2** and **3** (ester and acylhydrazone, respectively) have similar electronic effects on the aromatic ring (validated by the comparable K_a values for Cl^-), their transport activities were remarkably different. While the activity of transporter **2** was almost identical to **1**, compound **3** was nearly inactive, with a low transport activity. Receptor **5** possesses an acylhydrazone functional group, alike **3**, and showed an almost negligible transport, which contrasted with the much higher transport activity of its precursor aldehyde **4**.[121] Arylhydrazone **6**, lacking the acyl functional group, in comparison to **5**, showed a slightly better transport activity than the latter (**5**), although not significantly. In stark contrast, compound **7**, without acidic hydrazone N−H units, performed much better than structurally related receptors **5** and **6**. Moreover, receptor **8**, the acetal-protected version of compound **4,** presented a moderate transport activity, similar to **7**. Finally, bis-thiourea **10** showed a very low chloride transport ability, despite of the higher binding affinity of two thiourea binding units for chloride characterised by high binding constants. K_{11} and K_{12} of 49 and 10 M^{-1}, respectively.

As demonstrated with DFT studies presented in **Chapter II**, the thiourea and acylhydrazone binding units in receptors **3**, **5** and **6** are far away to cooperatively bind the same anion. A thiourea-based receptor, with a single binding unit, may interact with the phospholipid head groups and swap interaction to a competitor chloride anion that approaches the water/lipid interface, transporting it through the membrane. In stark

contrast, molecules with two binding sites (such as the hydrazone derivatives **3**, **5** and **6**, and bis-thiourea **10**) could bind to the anion with one motif, while the other is able to firmly bind with phospholipid head groups, which prevent the passive diffusion of the receptor across the phospholipid bilayer.

All these questions will be investigated by MD simulation studies in this chapter.

III.2. Methods

Molecular Dynamics (MD) simulations of the chloride complexes of **1**-**10** were carried out in a POPC membrane model. The transporters were described with GAFF2 force field parameters, the second iteration of the General AMBER Force Field (GAFF),[58, 59] and employing RESP charges,[64] calculated at the HF/6-31G(d) theory level, using 4 concentric layers per atom and 6 density points in each layer. Both charges and atomtypes were attributed using the antechamber software available in the AMBER suite.[134] MD simulations were performed using AMBER 18[98] with resort to GPU acceleration.[99, 100]

III.2.1. X-n2-ns-X reparameterization

Preliminary MM optimisations of acylhydrazone derivatives **3**, **5**, and **9** with default GAFF2 parameters for torsional terms and default atom types (see **Scheme III-1**), yielded structures distorted around the N−N central bond of the acylhydrazone fragment, with the C=N−N−C and C=N−N−H torsion angles (see the highlighted bonds in **Scheme III-1**) distant from the expected values, as follows. The MM minimised structures of **3**, **5**, and **9** presented C=N−N−C angles around ±70°, whilst CSD presented 797 structures with acylhydrazone moieties' C=N−N−C dihedral angle values ranging from 152.4° to 208.3° (normalised for the 0 to 360° range). Ten acylhydrazone derivatives, listed in **Table III-2**, were optimised in gas-phase at the B3LYP/6-31G(d) theory level, in agreement with the development of GAFF2's parameterization. The DFT computed structures resulted in torsion angles close to those observed in the solid state, in contrast to the MM optimised structures with default parameters. This preliminarily modelling studies revealed the need for the adjustment of the X−n2−ns−X (with ns being an amide N, attached to one hydrogen

atom) default force field parameters used in GAFF2 to describe the torsional energetic barriers around the N−N bond. These parameters were replaced by the torsional terms used for fragments described by the X−n2−n2−X dihedral term (with n2 being an aliphatic sp^2 N with two connected atoms), as given in **Table III-1**.

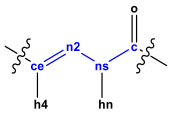

Scheme III-1

The MM optimisation of these ten structures, using the modified dihedral angle terms led to a significant improvement of the fitting between the MM structures, experimental structures and DFT ones, as shown by the root-mean-square deviation (RMSD) values given in **Table III-2**.

Table III-1. GAFF2's default parameters and the modified parameters used in this work (based on the X−n2−n2−X dihedral angle).

Dihedral Angles[a]	Scaling Factor	$V_n/2$ (kcal·mol^{-1})	γ (°)	Periodicity N
default parameters				
ce−n2−ns−c	2	0.800	0.000	2.000
ce−n2−ns−hn	2	0.800	0.000	2.000
modified parameters (based on X−n2−n2−X)				
X−n2−ns−X	1	3.000	180.000	-2.000
X−n2−ns−X	1	2.800	0.000	1.000

[a)] The n2 atom type corresponds to an aliphatic sp^2 N with two connected atoms, whilst the ns one corresponds to an amide N, with one hydrogen atom attached.

Table III-2. RMSD values (Å) ascertained between reference X-ray single crystal structures (XRD) or B3LYP/6-31G(d) optimised structures and the MM optimised structures with GAFF2's default and updated parameters for the X−n2−ns−X dihedral angle.

CSD Refcode	Ref.	default vs XRD	modified vs XRD	default vs B3LYP/6-31-G(d)	modified vs B3LYP/6-31-G(d)
HEFSUH	[135]	1.45	0.46	1.04	0.19
HOJCUG	[136]	1.16	0.20	1.28	0.17
IHINEV	[137]	1.39	0.70	1.38	0.72
IHINIZ	[137]	1.41	0.25	1.42	0.24
IHIPEX	[137]	1.18	0.32	0.95	0.14
LIFXIK	[138]	0.60	0.52	0.85	0.31
LUHFIE	[139]	1.24	0.34	0.93	0.20
QORSOG	[140]	1.59	0.64	1.40	0.36
VOVPOO01	[141]	1.14	0.26	1.28	0.08
VUHMOA02	[142]	1.03	0.20	0.91	0.13

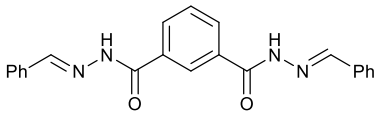
HEFSUH

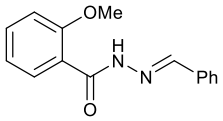
HOJCUG

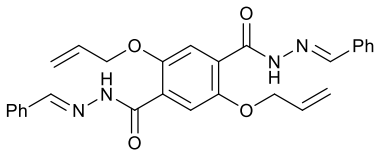
IHINEV

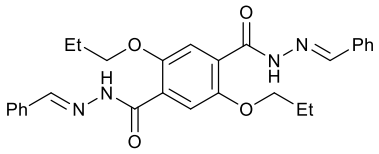
IHINIZ

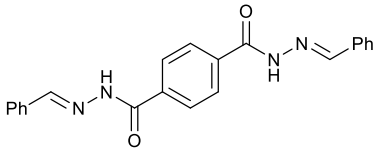
IHIPEX

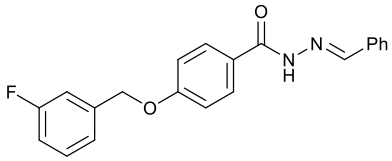
LIFXIK

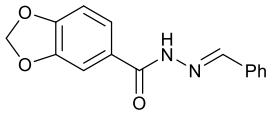
LUHFIE

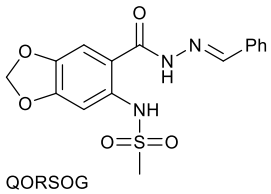
QORSOG

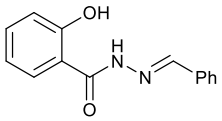
VOVPOO01

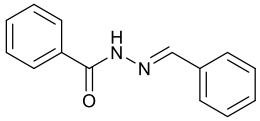
VUHMOA02

Scheme III-2. Structures of the compounds mentioned in **Table III-2**, with the corresponding refcodes.

III.2.2. Membrane MD simulations

The MD simulations were performed using the structures of the chloride complexes of **1**-**10** optimised by DFT in 1:1 or 1:2 receptor:anion stoichiometry. Two starting positions were considered: with the chloride complex immersed in the aqueous phase of a POPC membrane model (***A***), or in the core of the phospholipid bilayer (***B***), as shown in

Scheme III-3. These two alternative scenarios were built using Packmol,[143] from a previously equilibrated membrane model, composed by 128 phospholipids described with Lipid17,[95] 6500 TIP3P model water molecules,[144] and 18 Cl^- and 18 Na^+ ions (*ca.* 0.15 M). Suitable Lennard-Jones parameters were employed to describe the ions, using Li/Merz's 12-6 IOD set.[145] The systems' neutral net charge was achieved with the removal of one or two solvated anions from the system. Moreover, three (**1**, **2**, **4**, and **6**-**10**) or nine (**3** and **5**) independent MD runs were carried out for each starting scenario, which resulted in a total sampling time of 1.35 μs for the prior and 4.05 μs for **3** and **5** (*vide infra*).

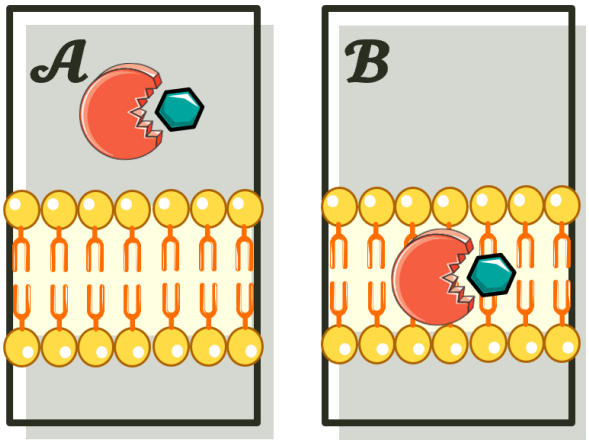

Scheme III-3. Representation of simulations' starting scenarios $\boldsymbol{\mathcal{A}}$ and $\boldsymbol{\mathcal{B}}$.

During the equilibration period of the MD simulations, the initial configuration of each system undergone 20000 steps of MM energy minimisation, of which the first half was carried out with the steepest descent algorithm and the second half with the conjugated gradient algorithm, with a 500 $kcal \cdot mol^{-1} \cdot Å^{-2}$ positional restraint was applied to the lipid molecules and chloride complex. Subsequently, the positional restrain was removed and the entire system was relaxed. Then, each system undergone a NVT ensemble run of 100 ps, heating from 0 to 303 K, with a positional restraint of 10 $kcal \cdot mol^{-1} \cdot Å^{-2}$ on the same residues as the initial minimisation. The systems went through an equilibration phase of 5 ns in the NPT ensemble, with a 5 $kcal \cdot mol^{-1} \cdot Å^{-2}$ positional restraint on the chloride complex. Afterwards, the positional restraint was removed, and each equilibrated system's simulation was extended for further 200 or 250 ns, in the $\boldsymbol{\mathcal{A}}$ and $\boldsymbol{\mathcal{B}}$ MD simulation scenarios, respectively. The long-range electrostatic interactions were described with the Particle Mesh Ewald (PME) algorithm,[146] using a real-space cut-off at 10 Å, the same cut-off as for Lennard-Jones interactions. The Langevin thermostat[147] was used to maintain the

bath temperature at 303 K, with a collision frequency of 1.0 ps^{-1}. The Berendsen barostat[148] preserved the pressure at 1 atm and compressibility of 44.6×10^{-6} bar^{-1}, with a relaxation time of 1.0 ps. The SHAKE algorithm[149] constrained the covalent bonds to hydrogen atoms, allowing a time step of 2 fs. Finally, the trajectory frames were saved every 10.0 ps of simulation, and posteriorly processed and analysed using *cpptraj*.[150]

III.2.3. MM interaction energies

The MM interaction energies between chloride transporters **1-10** and the phospholipids of the POPC phospholipid bilayer were calculated with the concatenated data of the last 50 ns of 3 MD runs carried out for each system, removing the water molecules, using **Eq. III-1**:

$$\Delta E_{MM} = \Delta E_{elec} + \Delta E_{vdW} + \Delta E_{INT} \qquad \textbf{Eq. III-1}$$

where ΔE_{elec} and ΔE_{vdW} correspond to the non-bonded electrostatic and van der Waals energy terms, while ΔE_{INT} corresponds to the sum of bond, angle, and torsion energies. The three individual MM energy components are given by **Eq. III-2** through **Eq. III-4**:

$$\Delta E_{elec} = E_{elec_{System}} - \left(E_{elec_{POPC}} + E_{elec_{Transporter}}\right) \qquad \textbf{Eq. III-2}$$

$$\Delta E_{vdW} = E_{vdW_{System}} - \left(E_{vdW_{POPC}} + E_{vdW_{Transporter}}\right) \qquad \textbf{Eq. III-3}$$

$$\Delta E_{INT} = E_{INT_{System}} - \left(E_{INT_{POPC}} + E_{INT_{Transporter}}\right) = 0 \qquad \textbf{Eq. III-4}$$

In the MM energy calculations, the POPC corresponds to the 128 POPC molecules, Transporter to the **1-10** isolated compounds, whilst the System corresponds to both (water molecules and ions are excluded from the calculations). The bonded term (ΔE_{INT}) amounts to zero, given that the individual terms $E_{INT_{System}}$, $E_{INT_{POPC}}$, and $E_{INT_{Transporter}}$ were calculated considering only MD simulations' "single-trajectories" where the transporters were already embedded and equilibrated into the membrane. Hence, according to **Eq. III-1**, the intermolecular interactions between the POPC membrane and the transporters were calculated using only the contributions from the non-bonded energy terms.

III.2.4. Umbrella Sampling MD simulations

The starting configurations required for the US simulations were obtained from MD simulations of the passive diffusion of the chloride complexes of **1** and **3** across phospholipid bilayer as follows: the final frame of the equilibration phase of both transporters, in starting scenarios $\mathcal{A}$ and $\mathcal{B}$, was used as the starting point for 200 ns long production phases, following the same protocol as the previous MD simulations (*vide supra*). The complex was preserved throughout MD simulation saving an harmonic restraint distance of 5 kcal·mol^{-1}·Å^{-2} and with the distance between the chloride and the nitrogen atoms of the thiourea binding units oscillating around 3.5 Å. Configurations with a spacing of *ca.* 1 Å between centres of mass (COM) of the receptors, completing a total of 42 evenly spaced starting points (from 0 to +41 Å along the *z* dimension/bilayer normal), were gathered from the restrained MD simulations of **1** and **3**. Noteworthy, only windows for one side of the membrane were simulated, as a symmetric behaviour would be expected in the remaining half (-41 to 0 Å along the *z* dimension/bilayer normal).

The US simulations were run using the collected configurations, with distance restraints of 5 kcal·mol^{-1}·Å^{-2} relative to the *z* dimension, between the COM of the heavy atoms of the receptor, and the COM of the phosphorous atoms of the lipid head groups and the terminal carbon atoms of the lipid tails. A harmonic restraint of 5 kcal·mol^{-1}·Å^{-2} was also used to maintain the receptor-chloride complex throughout the US simulations. Each independent US window was properly minimised and heated prior to the production phase, following the same protocol as the passive diffusion (*vide supra*), apart from the distance restraints. Although the production stage was composed of 120 and 130 ns (for complexes **1** and **3**, respectively), only the last 50 ns were considered as sampling time.

The vFEP method[78] was used to assess the free energy profiles from the US simulations of complexes **1** and **3**. Subsequently, the profiles were plotted with the bootstrap errors calculated from 100 random data sets of equal size.

III.3. Results and Discussion

III.3.1. Diffusion of the transporters within the membrane

The interaction and the passive diffusion of **1**-**10** were investigated at the atomistic level with MD simulations in a POPC membrane model. In accordance with the chloride efflux studies, the molecules were categorized as good – **1**, **2** and **4**; moderate – **7** and **8**; and poor transporters – **3**, **5**, **6**, **9** and **10**. Additional details are given in ***III.2. Methods*** section.

The diffusion of the synthetic transporters was monitored by assessing the relative distances between the COM of the aromatic rings (designated **A**, **B** and **C**, as shown in **Figure III-1**) and the water/lipid interface, which allowed to deduce the relative position and orientation of the transporters along the bilayer normal (*z* coordinate) throughout the MD simulation. The positive distances relative to the water/lipid interface (averaged from the *z* coordinates of the leaflet's 64 phosphorus atoms) suggest that the given molecular fragment is in the aqueous phase of the system (above the phosphorus), while negative values indicate that it is embedded in the POPC bilayer (below the phosphorus). The most representative run of the passive diffusion of transporters **1**-**10**, for each starting scenario, is depicted in **Figure III-3** and **Figure A1** to **Figure A3**, representing the relative position of the reference points and the total count of hydrogen bonds to chlorides. Overall, within the first ns of each MD simulation, the associated chloride is rapidly solvated and released to the water phase, regardless of the starting scenario. Moreover, transporters in scenario $\mathcal{A}$ diffuse in the water phase of the system prior to bilayer permeation, and despite the higher lipophilicity of the fluorinated aromatic ring (**A**), this fragment is not necessarily the first one to permeate the membrane. However, once the molecules are nested below the water/lipid interface and acquired their preferential orientations, the lipophilic fluorinated ring **A** (red line in in **Figure III-3** and **Figure A1** to **Figure A3**) is closer to the bilayer core, and the remaining aromatic rings **B** or **C** are found near the water phase (blue and pink lines, respectively). This preferential relative position for **1**, **3**, **5** and **9** is depicted with MD snapshots in **Figure III-2**. Having observed the ergodicity between the spatial disposition observed in the individual stochastic MD runs, relatively to the water/lipid interface, the MD sampling data (last 80 and 130 ns of each run for scenarios $\mathcal{A}$ and $\mathcal{B}$, respectively) were merged, affording 0.63 μs of sampling time for transporters **1**, **2**, **4**, and

6-10, and 1.89 μs for **3** and **5**. Hence, the following structural and energetic analyses of the synthetic transporters' MD simulations were performed with the concatenated data, except where otherwise stated.

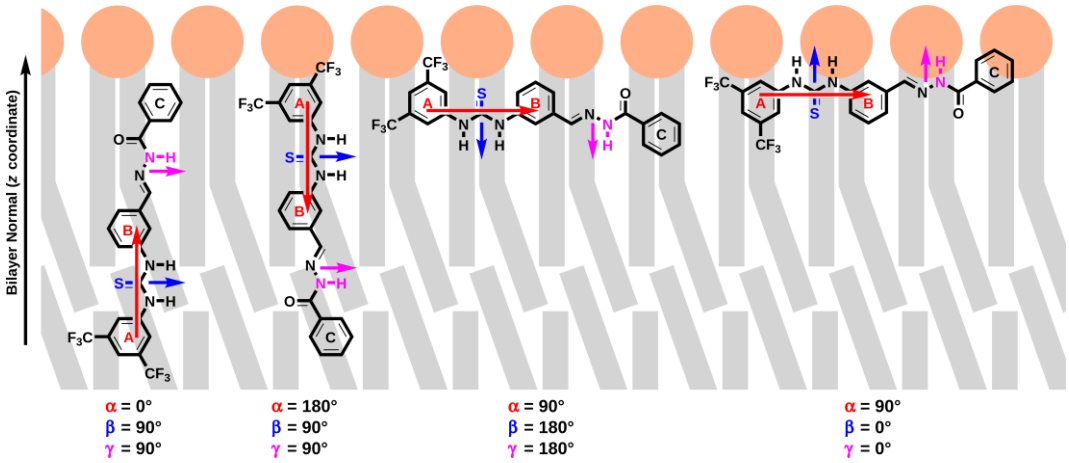

Figure III-1. Schematic identification of the **A**, **B** and **C** reference points, illustrated for the aromatic rings of **5**. The vectors $\overrightarrow{AB}$, $\overrightarrow{SC}$ and $\overrightarrow{NH}$, used to assess the α, β and γ angles with the bilayer normal, are also illustrated for this molecule.

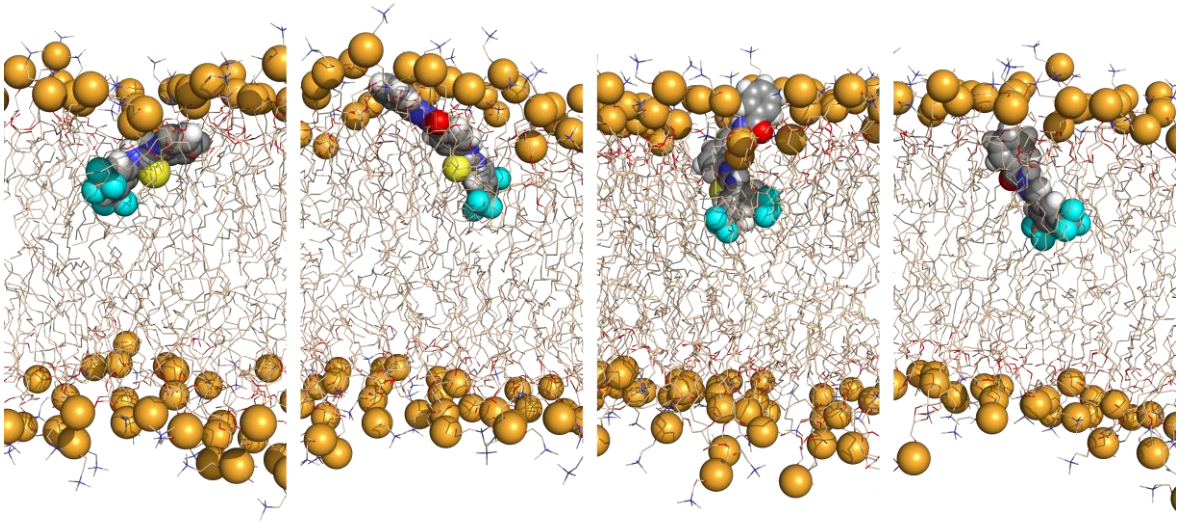

Figure III-2. Snapshots of MD runs of transporters **1**, **3**, **5**, and **9**, illustrating the orientations acquired at the water/lipid interface. Water molecules, aliphatic protons, and ions are omitted for clarity.

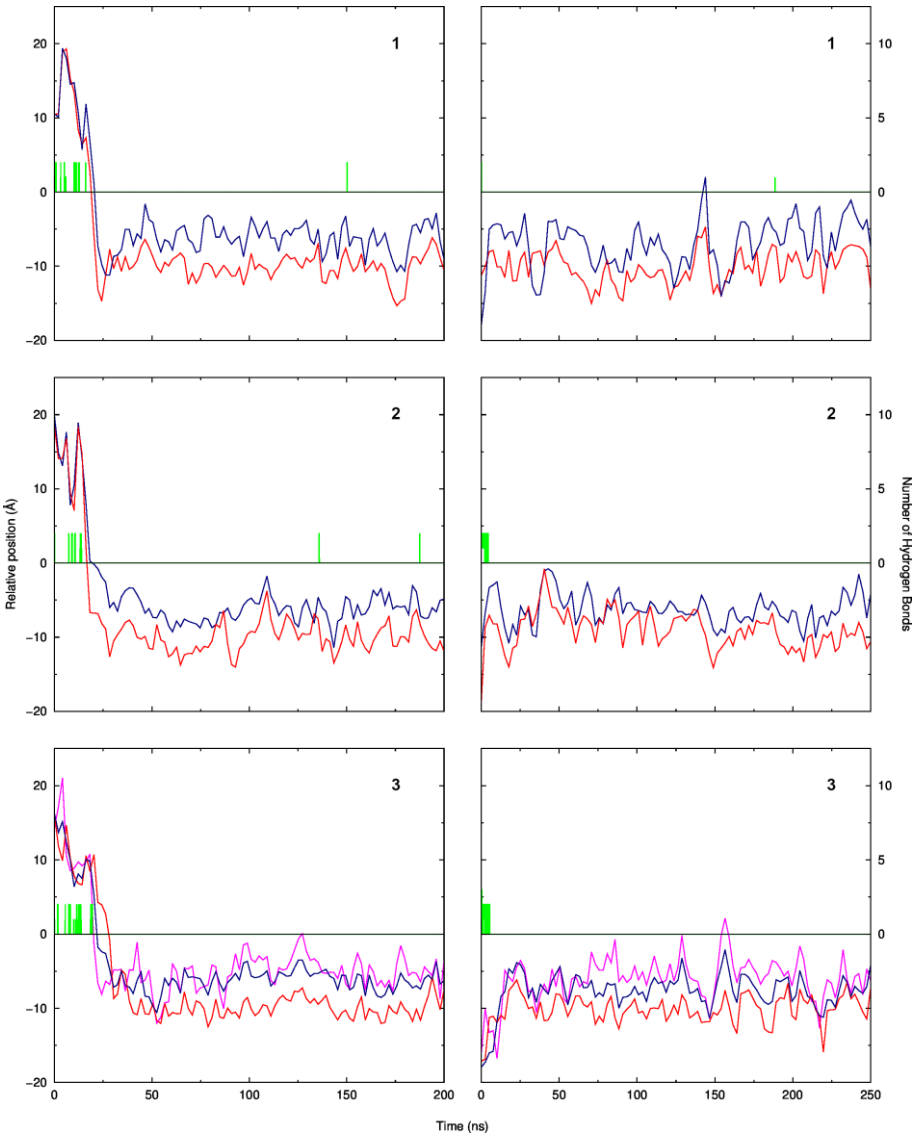

Figure III-3. Evolution of the relative position of the **A**, **B** and **C** (red, blue and magenta lines, respectively) reference points in illustrative MD runs in the ***𝒜*** (left) and ***ℬ*** (right) scenarios. The plotted green lines correspond to the evolution of the total number of N−H···Cl^- hydrogen bonds. The black line at z = 0 Å represents the water/lipid interface.

A more thoughtful and complementary approach to establish the preferential orientation of the different synthetic transporters towards the water/lipid interface is given by the α, β and γ angles, between the vectors $\overrightarrow{AB}$ (from aromatic ring **A** to **B**), $\overrightarrow{SC}$ (from the thiourea's sulphur atom to the adjacent carbon atom) and $\overrightarrow{NH}$ (the hydrazone N-H bond), and the z coordinate, as described in **Figure III-1**. For instance, an angle α of 0° is observed when a given transporter is parallel to the membrane normal, with the fluorinated aromatic ring (**A**) closer to the bilayer core, while an 180° angle indicates that it is near the

interface. By contrast, a 90° α angle is observed when the molecule is parallel to the interface. The β and γ angles give the orientation of both binding units, whether they point towards the water phase (~0°) or to the bilayer core (~180°). The histograms for the mentioned angle values are plotted in **Figure III-4**, and **Figure A4** to **Figure A5**, while their average values and corresponding standard deviations are listed in **Table III-3**.

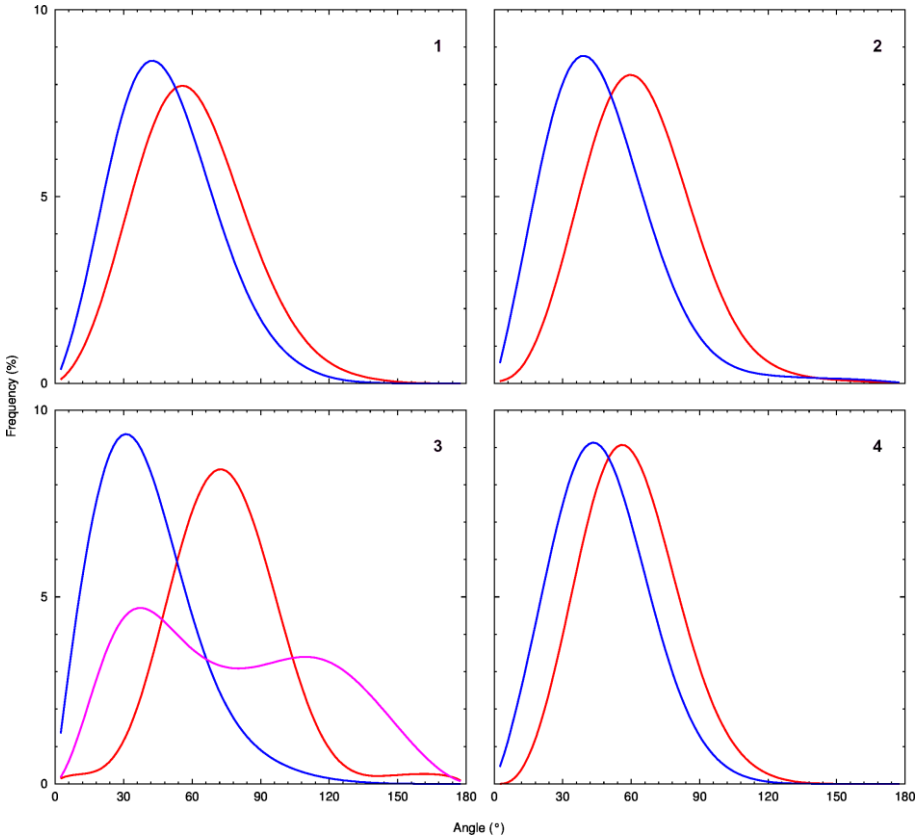

Figure III-4. Frequency profiles showing the distribution of the α (red line), β (blue line) and γ (magenta line) angles, assessed during the sampling period of the MD simulations of **1**-**4**. Data were smoothed using Bézier curves.

Table III-3. Average α, β and γ angles (°), with their standard deviations, assessed for the cumulative sampling time in the MD runs of the different transporters.

Molecule	Angle (°)		
	α	β	γ
1	58.8 ± 21.8	46.8 ± 19.9	-
2	62.3 ± 21.1	44.6 ± 22.7	-
3	73.9 ± 21.9	37.4 ± 20.1	77.1 ± 41.4
4	57.8 ± 17.4	44.8 ± 17.7	-
5	62.0 ± 21.6	44.9 ± 20.9	76.2 ± 37.1
6	66.8 ± 25.6	47.0 ± 24.5	41.5 ± 20.2
7	68.3 ± 21.5	44.4 ± 23.1	-
8	63.6 ±20.2	40.6 ±18.8	-
9	63.2 ± 21.3	-	38.7 ± 25.3
10 (Thiourea 1)	65.0 ± 25.2	55.4 ± 22.1	-
10 (Thiourea 2)	65.2± 26.7	56.1 ± 22.5	-

Overall, molecules **1**, **2**, **4** and **8** have average α angle values of 60.6 ± 20.9°, suggesting that these mono-thioureas frequently adopt oblique spatial dispositions, while the corresponding thiourea binding motifs are often pointing to the water phase, enabling them to interact with phosphate head groups, water molecules or solvated chloride ions (*vide infra*). The *N,N*-dimethyl-hydrazone derivative **7** adopted an equivalent orientation inside the POPC bilayer, given the profiles of the α and β angles with average values of 68.3 ± 21.5° and 44.4 ± 23.1°, respectively. The thiourea fragments of the acylhydrazones **3** and **5** are spatially oriented similarly to the mono-thioureas above-mentioned, as indicated by the comparability between the α and β angles. Regarding the γ angle values of the acylhydrazone fragment of **5**, they range from 0 to 180º, leading to a considerably large standard deviation of 41.4º, whilst the distribution profile for **3** presents two local maxima around 38 and 113º, as depicted in **Figure III-4**. Thus, the orientation of the acylhydrazone motif is variable, allowing it to easily interact with the phosphate head groups, water molecules, and with the ester groups of the *sn*-1 and *sn*-2 phospholipid chains. In contrast, the arylhydrazone derivative **6** presents a slighter variation of the γ angle values (38.7 ± 25.3°), suggesting a N−H binding unit with a well-defined orientation, pointing towards the water phase. The high variability on the orientation of the acylhydrazones can be attributed to the N−H unit's higher $V_{S,max}$ of molecules **3** and **5** in comparison to **6** (*vide supra*), giving them a higher propensity to alternate between different hydrogen bonding acceptors. Molecule **9**, in stark contrast to the other acylhydrazone derivatives, presents α

and γ angle average values of 63.2 ± 21.3° and 38.7 ± 25.3°, respectively, demonstrating that it is possible for a receptor with a single acylhydrazone moiety to have a clear orientation at the water/lipid interface. The bis-thiourea **10** displays well-defined α and β angle profiles for both thiourea fragments and their corresponding average values are comparable to the ones attained for the mono-thioureas. Additionally, the thiourea binding units are indistinguishable and equally able to independently recognise chloride ions, water molecules or phosphate head groups, at the water/lipid interface level, as shown in the overlap between the α and β profiles (see **Figure A5**).

The hydrogen bonding contacts between the thiourea or hydrazone-based binding units and water molecules, chloride ions or phospholipids were assessed throughout the entire MD simulation time of the different MD replicates carried out for each receptor. The total counting of these hydrogen bonds for **1**, **2** and **3**, as function of the *z* coordinate are plotted in **Figure III-5**, and in **Figure A6** and **Figure A7** for the remaining transporters. Overall, along the diffusion in the water phase, for scenario $\mathcal{A}$, the thiourea binding motif of molecules **1**-**8** sporadically recognises one of the eighteen solvated chloride ions. On the other hand, in starting scenario $\mathcal{B}$, the chloride hydrogen bonded to the thiourea binding motif is promptly solvated and released to the water phase. Afterwards, the chloride uptake events become occasional, as the number of N−H···Cl^- is close to zero. Regardless of the starting scenario, as the transporters reach the water/lipid interface (z = 0 Å), the hydrogen bonds between both thiourea N−H binding motifs and water molecules are partially replaced by interactions with phospholipids, primarily with the phosphate head groups and, to a smaller extent, with the *sn*-1 and *sn*-2 ester groups. The total number of hydrogen bonds between transporter **10** and the phospholipids naturally increases because of its two independent thiourea binding units being equally able to establish hydrogen bonds with phosphate head groups. Additionally, they were also found to occasionally be able to simultaneously bind two phosphate head groups throughout the MD simulations (see **Figure III-6**). Therefore, the great binding affinity of this bis-thiourea for phospholipids is possibly linked with its inability to promote the chloride transmembrane efflux.

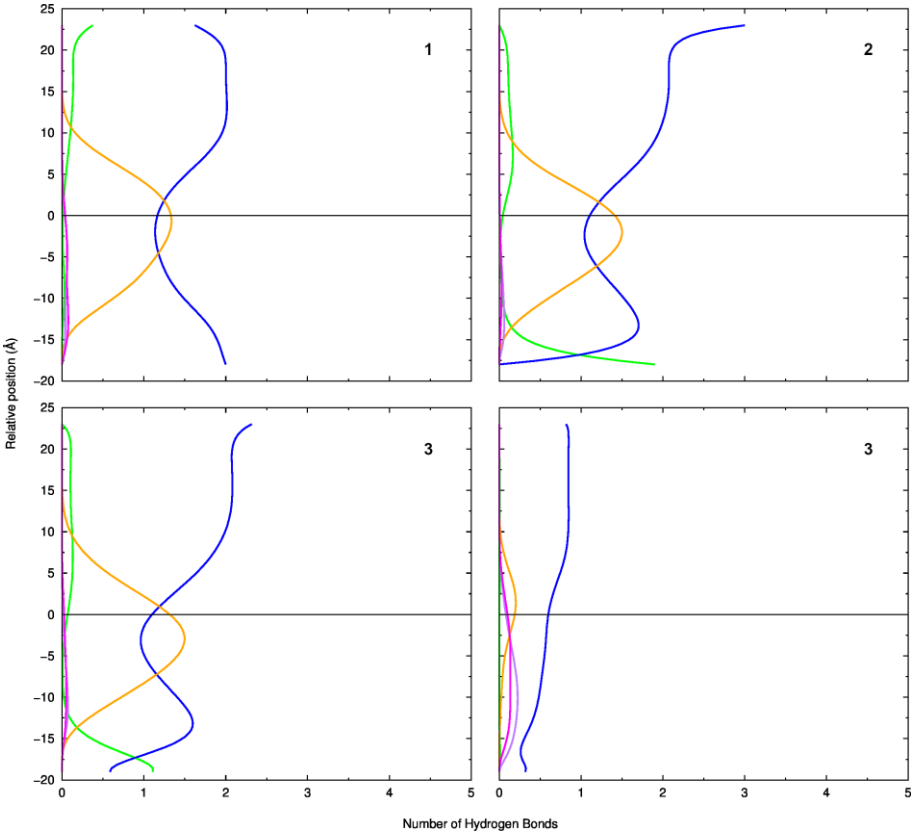

Figure III-5. Average number of thiourea hydrogen bonds vs. the relative position of the centre of mass of **1**, **2**, and **3** (left for the thiourea and right for the acylhydrazone motif). The following colour scheme is used for the interactions with the water molecules (blue), chloride ions (green), ester groups (magenta for the *sn*-1 chains and purple for the *sn*-2 chains) and POPC head groups (orange). The black line at z = 0 Å represents the water/lipid interface. Data were smoothed using Bézier curves.

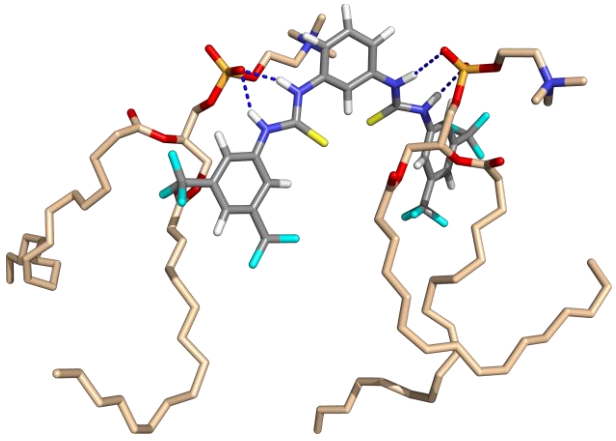

Figure III-6. MD snapshot illustrating the interaction of both thiourea binding units of **10** with two POPC phosphate head groups.

In contrast, and in agreement with the wide range of γ angle values and V_S values in the hydrazone binding units of **3** and **5**, the hydrogen bonds established by these motifs swap between water molecules, the phosphate head group, and *sn*-1 and *sn*-2 ester phospholipid groups, forming intermittent N−H···O hydrogen bonds, putatively assisted by C−H···O bonding contacts. Furthermore, **6** and **9** present comparable hydrogen bonding interactions, although the hydrazone moiety's orientation of these molecules is more consistent, as shown by the narrower deviation of the corresponding γ angles (see **Table III-3**). Regardless of the small extent of the presented hydrogen bonds, they have a substantial impact on the interaction of these hydrazone-based receptors with the POPC membrane model, as corroborated by the following energy calculations.

III.3.2. Energetic analysis

The interaction between transporters **1**-**10** and the phospholipids was assessed from the reported unrestrained passive diffusion MD simulations, *via* molecular mechanics (MM) gas-phase interaction energies, considering the last 50 ns of each MD run. The contributions of the non-bonded electrostatic (ΔE_{elec}) and van der Waals (ΔE_{vdW}) energy terms in relation to the MM interaction energy (ΔE_{MM}) were calculated as detailed in the ***III.2. Methods*** section and the average values obtained are listed in **Table III-4**. The of ΔE_{MM} values increase almost linearly with the ΔE_{elec} (R^2 = 0.93) and ΔE_{vdW} (R^2 = 0.93) values, the latter being the main contributors to the ΔE_{MM} values.

Table III-4. Molecular Mechanics interaction energies (kcal mol^{-1})[a] between the phospholipids and compounds **1**-**10**, listed together with their relative transport ability marks.

Molecule	RTA (Cl^-)[b]	ΔE_{MM}	ΔE_{elec}	ΔE_{vdW}
1	Good	-57.1 ± 11.3	-16.2 ± 10.7	-40.9 ± 3.0
2	Good	-63.5 ± 13.3	-17.1 ± 11.6	-46.4 ± 5.7
3	Poor	-87.8 ± 13.8	-28.6 ± 13.3	-59.2 ± 4.3
4	Good	-64.5 ± 12.5	-20.9 ± 12.1	-43.6 ± 3.3
5	Poor	-87.0 ± 15.1	-28.6 ± 13.9	-58.5 ± 4.8
6	Poor	-73.9 ± 10.4	-16.8 ± 9.7	-57.2 ± 3.7
7	Moderate	-66.7 ± 10.7	-15.1 ± 9.7	-51.6 ± 3.6
8	Moderate	-69.0 ± 12.6	-20.6 ± 11.7	-48.5 ± 4.0
9	Poor	-49.7 ± 6.9	-8.0 ± 5.3	-41.7 ± 3.3
10	Poor	-102.4 ± 15.6	-35.2 ± 15.6	-67.1 ± 4.2

[a] Energetic analysis based on 1500 frames (extracted every 200 ps), apart from **3** and **5**, for which 4500 frames were considered; [b] Relative transport ability.

The transport properties of the thiourea derivatives are largely dependent on the strength of the van der Waals interactions between the phospholipid and these transporters. Accordingly, the good transporters are smaller molecules like **1**, **2** and **4**, establish weaker vdw interactions with ΔE_{vdW} values of -40.9, -46.4, and -43.6 kcal mol^{-1}, respectively. These are followed by **7** and **8**, moderate transporters with intermediate vdw interactions with ΔE_{vdW} values of -51.6 and -48.5 kcal mol^{-1}. Larger receptors containing hydrazone moieties with equivalent lengths, such as **3**, **5** and **6**, present ΔE_{vdW} values around -58 kcal mol^{-1} corresponding to higher vdw interactions and have poor chloride transport ability. Stronger electrostatic interactions with the membrane also decrease the ability to promote the chloride efflux. Receptors with a single thiourea binding motif (**1**-**2** and **4** as good transporters, and **7**-**8** as moderate transporters) show equivalent ΔE_{elec} average values, ranging from -20.9 to -15.1 kcal mol^{-1}. On stark contrast, the binding ability of the hydrazone binding motif of **3** and **5** (evaluated with V_S) leads to increasingly stronger electrostatic interactions with the bilayer (*ca*. -28.6 kcal mol^{-1}), contributing to a poorer transport capability. The *meta*-phenylene bis-thiourea **10**, with two electron-withdrawing and highly lipophilic 3,5-bis(trifluoromethyl)phenyl groups is naturally a poor transporter, presenting the highest average values of -35.2 and -67.1 kcal mol^{-1}, for the ΔE_{elec} and ΔE_{vdW} terms, repectively. These electrostatic interactions mainly occur between the acid thiourea N−H binding unit and phosphate head groups, including hydrogen bonds. In fact, this molecule has the higher propension to establish these kind of interactions, as shown by

their $V_{S,max}$ values. Alternatively, poor transporter **9** has weaker interactions the bilayer, with ΔE_{elec} and ΔE_{vdW} average values of -8.0 and -41.7 kcal mol^{-1}, respectively. However, **9** is composed of a single acylhydrazone binding motif, with a low chloride affinity, as indicated by DFT calculations and ^{1}H-NMR titration binding data.

III.3.3. Structural impact on the bilayer

The structural impact of the transporters **1-10** onto the membrane was assessed throughout the MD sampling data. This was carried out by comparing structural parameters such as the area per lipid, bilayer thickness, electron density profile and order parameters $|S_{CD}|$ with a free membrane model. The average values for the area per lipid, bilayer thickness and root-mean-square error (RMSE) between the order parameters of the free bilayer and the systems with **1-10** are gathered in **Table III-5**, whilst the density profiles are plotted in **Figure III-7** to **Figure III-8**. The structural parameters attained from the MD simulations are comparable to the free membrane without transporters, with the small deviations being attributed to the nesting of the transporters at the water/lipid interface level, indicating that the impact of this series of small molecules has a marginal impact on the POPC bilayer.

Table III-5. Comparison between the area per lipid, bilayer thickness, and root-mean-square error (RMSE) of the transporters' MD simulations sampling time and a free membrane system (100 ns of sampling).

Molecule	Area per lipid (Å^2)	Bilayer thickness (Å)	$\|S_{CD}\|$ RMSE		*N*
	Avg ± SD	Avg ± SD	*sn*-1	*sn*-2	
Free Membrane	67.63 ± 1.21	37.23 ± 0.52	-	-	10000
1	67.98 ± 1.26	37.19 ± 0.55	0.0023	0.0022	63000
2	68.13 ± 1.14	37.12 ± 0.52	0.0018	0.0024	63000
3	68.05 ± 1.21	37.17 ± 0.53	0.0020	0.0022	189000
4	67.88 ± 1.25	37.21 ± 0.56	0.0019	0.0026	63000
5	68.10 ± 1.25	37.15 ± 0.56	0.0020	0.0019	189000
6	67.68 ± 1.12	37.32 ± 0.49	0.0036	0.0032	63000
7	68.00 ± 1.22	37.18 ± 0.54	0.0020	0.0027	63000
8	67.89 ± 1.23	37.23 ± 0.54	0.0038	0.0029	63000
9	67.95 ± 1.17	37.19 ± 0.51	0.0025	0.0026	63000
10	67.65 ± 1.19	37.01 ± 0.60	0.0030	0.0024	63000

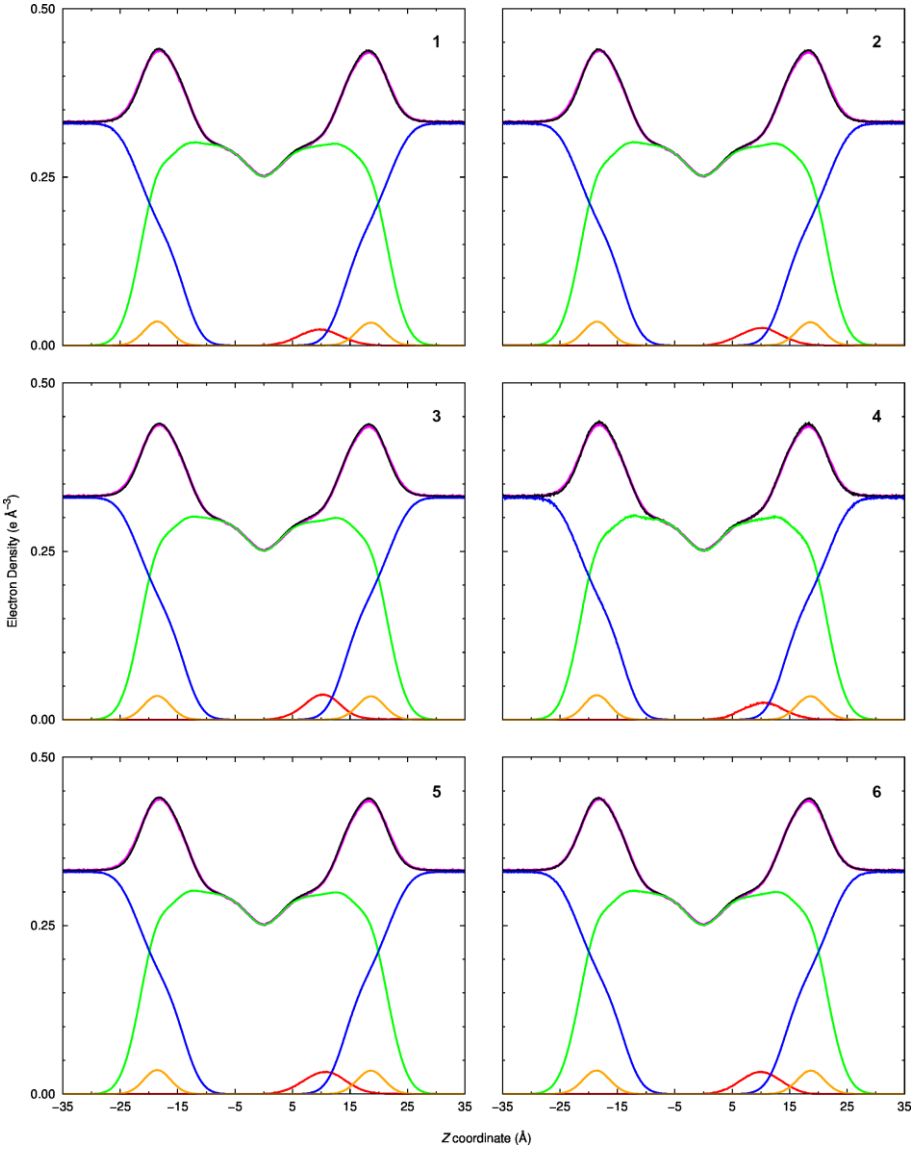

Figure III-7. Electron density profiles of transporters **1-6**, with the full system plotted in black, phospholipids in green, water in blue, phosphorus atoms in orange, and the transporter in red. The free membrane profile is also shown as a magenta line. The transporter's profiles are scaled 5 times. The core of the POPC bilayer corresponds to z = 0 Å.

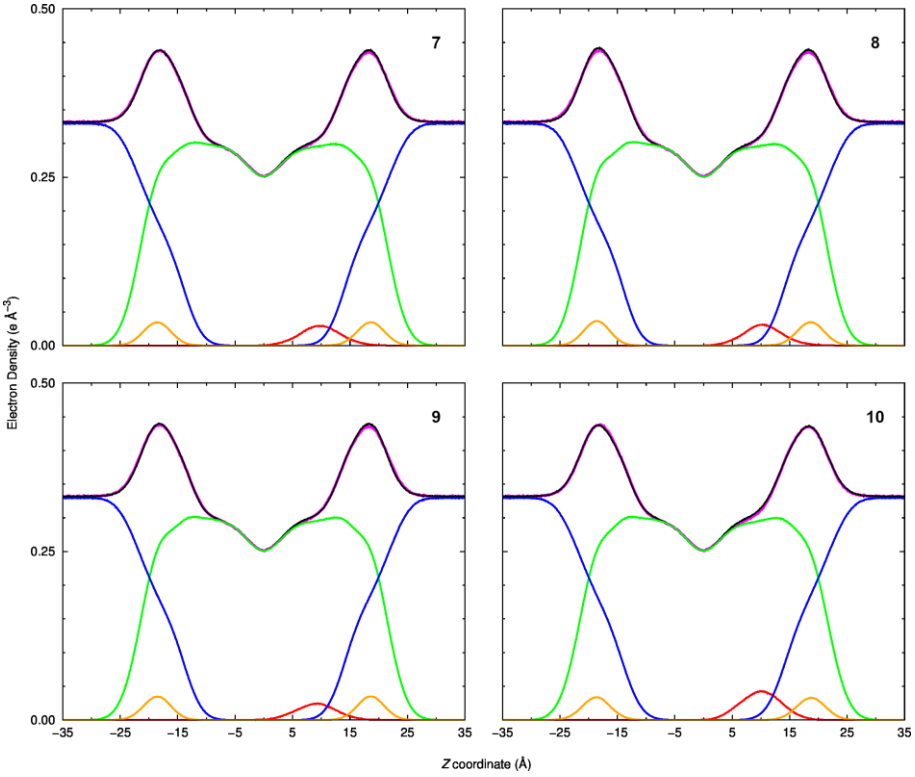

Figure III-8. Electron density profiles of transporters **7-10**. Remaining details are given in **Figure III-7**.

III.3.4. Constrained MD simulations

Further structural insights in the anion transport ability of receptors **1**, **3** and **5** were obtained through constrained MD simulations of their thiourea bound chloride complexes.

These MD simulations with distance constraints to the chloride yielded results in conformity to the passive diffusion, for the receptor orientation characterised by the angles α, β and γ (depicted in **Figure A8**) and for the hydrogen bonds to the binding units, as would be expected. In spite of the thiourea motif being occupied with a chloride anion for the entirety of the restrained simulation, the acylhydrazone motif presented a behaviour similar to the passive diffusion MD simulations, as shown in **Figure III-9** consistent with its weak interaction with phosphate phospholipid head groups.

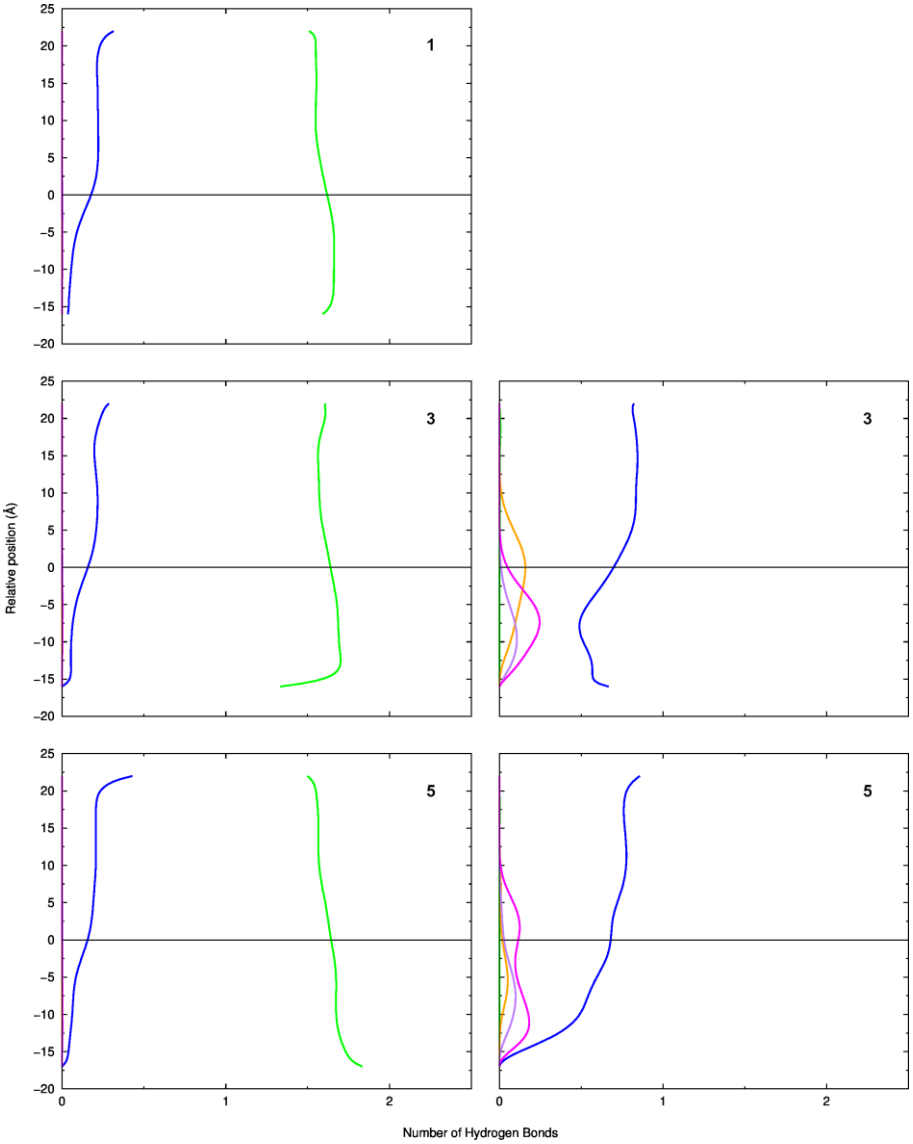

Figure III-9. Average number of thiourea (left) and acylhydrazone (right) hydrogen bonds vs. the relative position of the centre of mass of **1**, **3**, and **5**. Remaining details are given in **Figure III-5**.

Alike the passive diffusion simulations, the orientation of the complexes **1** and **3** in the 41 US simulation windows was also ascertained, and a heatmap of the α, β and γ angles of the complex along the *z* coordinate was built using sampling data from the last 50 ns of each window MD run, as depicted in **Figure III-10** and **Figure III-11**. These results are in complete agreement with the passive diffusion, evidencing the achievement of a well-defined orientation once the complex is found within the highly packed membrane medium, with frequent angle values comparable to those of the passive diffusion for receptors **1** and **3** (**Figure III-4**). Moreover, the interaction between **1** or **3** and the

phospholipids of the POPC membrane was also assessed *via* MM interaction energies (as detailed in ***III.2. Methods*** section) for the US simulations' sampling time. The interaction energies between the transporters and the phospholipids, as these permeate the membrane, presented in **Figure III-12** agree with those presented in **Table III-4** for the unrestrained passive diffusion, as the worse transporter **3** interacts with the phospholipids to a bigger extent, mostly through van der Waals interactions. The *ca* 17 kcal mol^{-1} difference between the US simulations and the respective unrestrained MD simulations is attributed to the association to the chloride in the complex, resulting in the displacement of more water molecules to the bilayer's inside, therefore reducing the interaction between the receptors and the phospholipids.

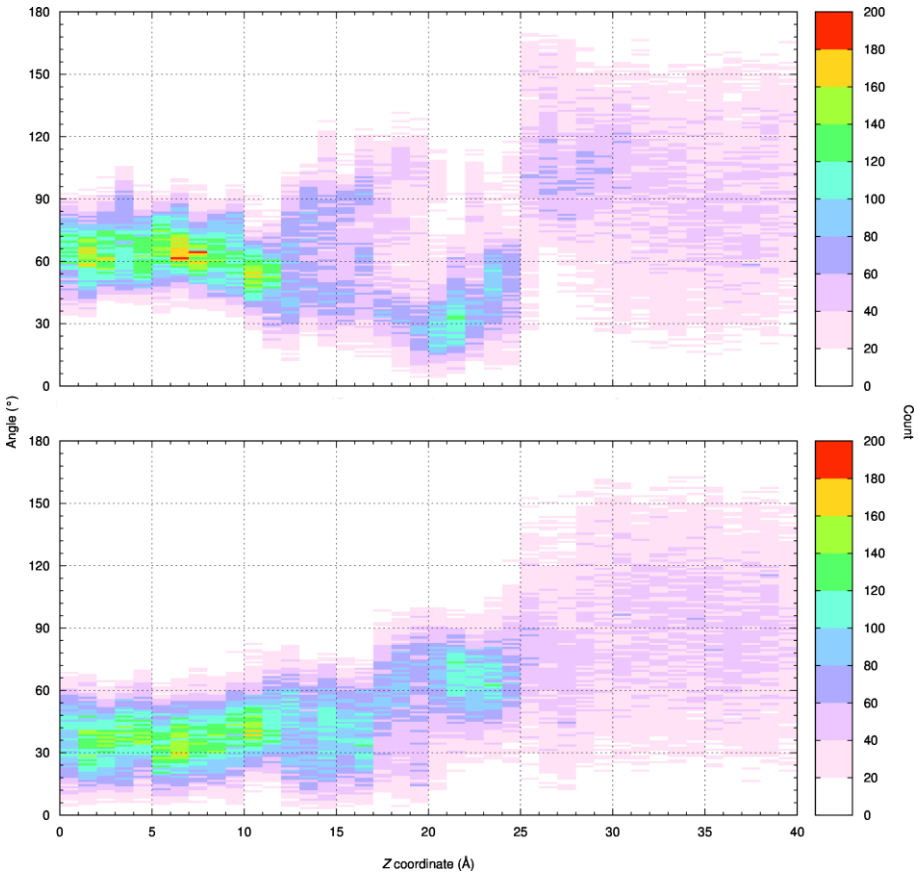

Figure III-10. 2D histogram created from the α (top) and β (bottom) angle values monitored along the *z* coordinate positions of complex **1**, throughout 41 independent US windows. The colour ranges from white (no occurrence) to red (200 occurrences).

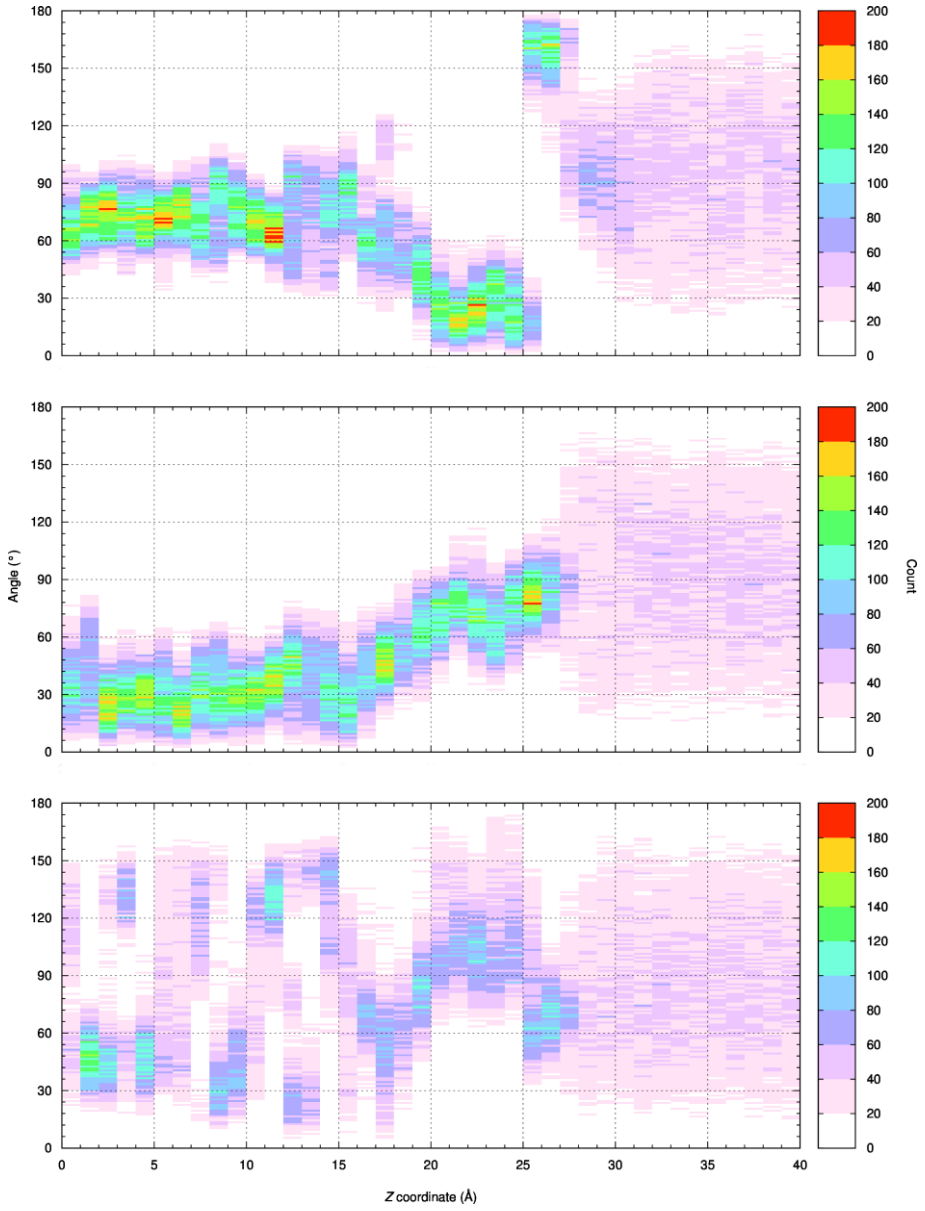

Figure III-11. 2D histogram created from the α (top), β (middle), and γ (bottom) angle values monitored along the *z* coordinate positions of complex **3**, throughout 41 independent US windows. The colour ranges from white (no occurrence) to red (200 occurrences).

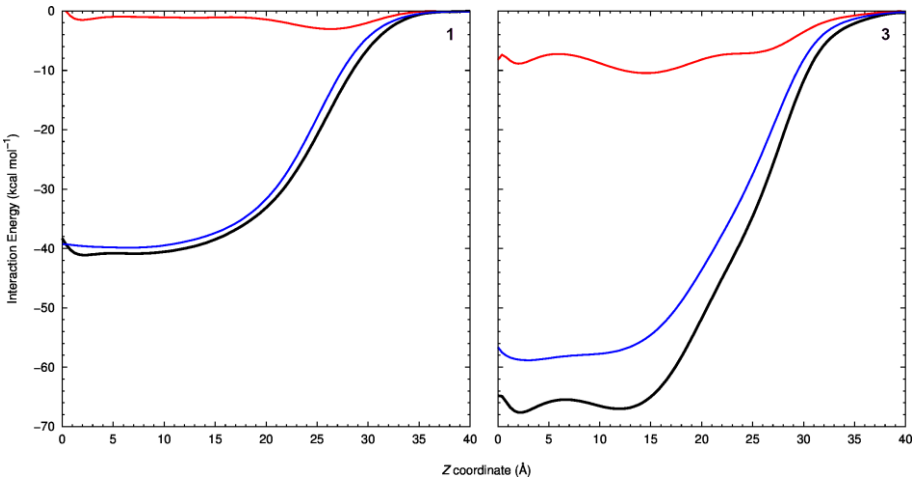

Figure III-12. Molecular Mechanics interaction energies (kcal mol^{-1}) from the 41 independent US simulation windows, between the phospholipids and complexes **1** and **3**, with the total energy (black), and van der Waals (blue) and electrostatic (red) contributions along the *z* coordinate.

The chloride transport ability of **1** and **3** was energetically characterised with the reconstruction of the PMF from their chloride complexes US MD simulations. The convergence and equilibration of the PMF profiles was established by evaluating the data in sequential intervals of 10 ns, until the different interval curves overlapped (**Figure III-13**). In contrast to the previously mentioned MM energy studies, that accounts for the receptor's interaction with the phospholipids, the PMF indicates the receptor's free energy variations as it surpasses the lipid/water interface and diffuses to the bilayer's core.

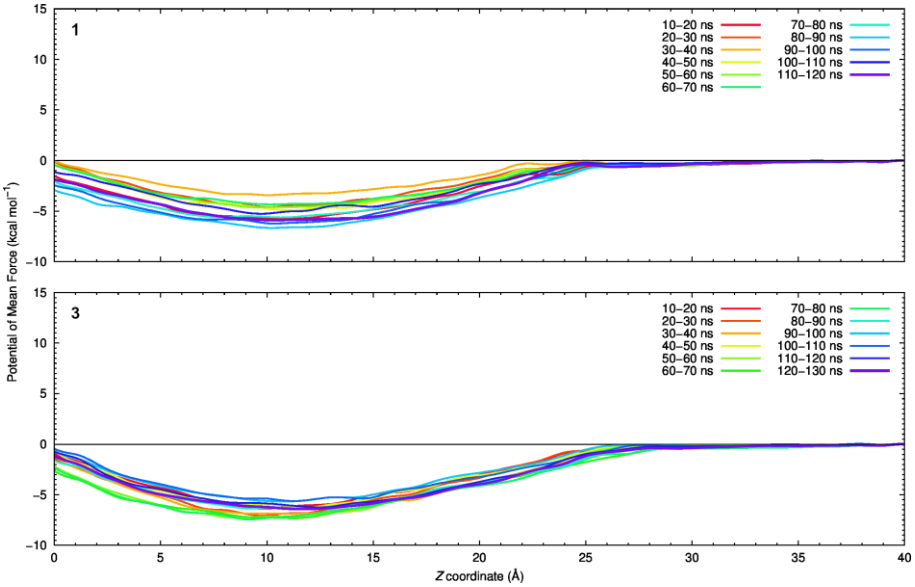

Figure III-13. The equilibration and convergence of the US simulation windows were evaluated in 10 ns intervals (coloured accordingly), of which the last 50 ns were used to calculate the PMF of complexes **1** and **3**.

The free energy profiles were computed using the vFEP method,[78] from the US simulations' sampling time (last 50 ns), and are plotted in **Figure III-14**, while (the individual profiles, plotted with the bootstrap errors calculated from 100 equal sized random data sets are presented in **Figure III-15**). As complexes **1** and **3** permeate the POPC bilayers, a drop occurs in the free energy profile until minima of -5.91 and -6.05 kcal mol^{-1} was achieved at z = 10.05 Å and z = 11.65 Å for complexes **1** and **3**, respectively (with the phosphate heads located at *ca.* 18 Å). Moreover, the free energy corresponding to the complex with the larger receptor (**3**) starts to decline slightly sooner than complex **1**. Between the energy minima of both complexes and the bilayer core (z = 0 Å) there is an increase in the free energy, indicating the energy barrier that must be surpassed for the complexes to cross the lipid tails towards the opposite leaflet. This energy barrier is *ca* 1.1 kcal mol^{-1} larger for the poor transporter **3** (-0.90 kcal mol^{-1}), in comparison to **1** (-2.02 kcal mol^{-1}).

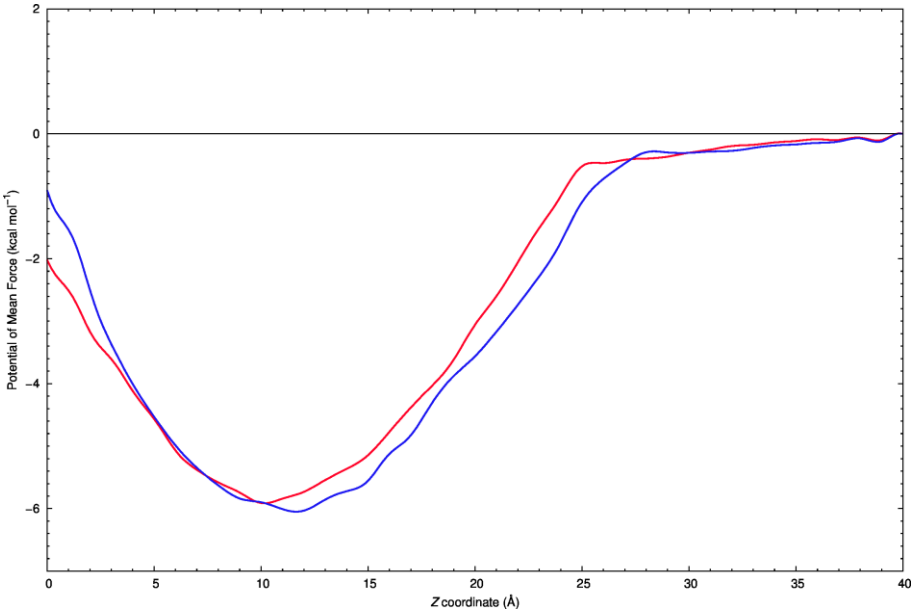

Figure III-14. PMF of complexes **1** (red) and **3** (blue) as a function of the *z* coordinate throughout the sampling period of 41 independent US simulation windows.

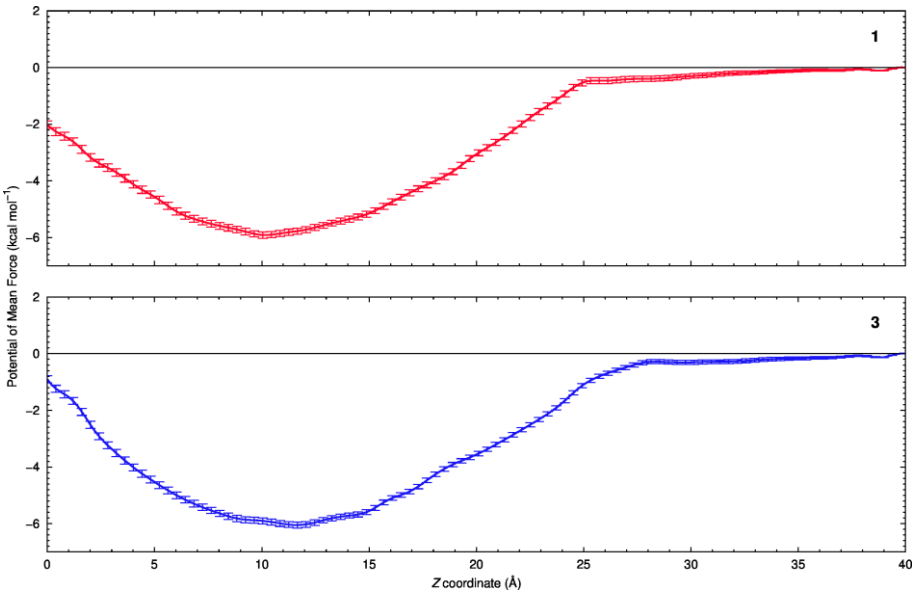

Figure III-15. PMF of complexes **1** and **3** as a function of the *z* coordinate throughout the sampling period of 41 independent US simulation windows. The error bars correspond to the bootstrap errors computed from 100 random data sets of equal size.

III.4. Conclusions

This chapter's results confirm that the addition of non-cooperative functional groups to the structure of anion receptors hinder its transport capabilities rather than the opposite. Receptors **3**, **5** and **6**, mono-thioureas functionalized with aryl- and acylhydrazone groups in the *meta* or *para* positions, yielded transport activities substantially lower when compared to the reference mono-thiourea **1**. The comprehensive membrane model MD simulations reported in this chapter show that the poor transport is caused by the presence of an additional binding unit (whether it is an acylhydrazone or a thiourea), which interacts strongly with the membrane. Moreover, the negligible transport activity of bis-thiourea **10** (compound with two binding units unable to bind to the same anion) compared to **1** supports the proposed hypothesis that a secondary non-cooperative binding site hinders the diffusion of the transporter-anion complex by interacting with the membrane. This also indicates that the detrimental effect of additional binding sites is not exclusive for hydrazone groups, but also applies to urea, thiourea, and, potentially, to other anion binding motifs.

Chapter IV.
Conclusions & Future Work

IV.1. Conclusions

The quantum calculations showed a superior binding affinity of the thiourea binding units for chloride. Additionally, receptors with two binding sites (**3**, **5**, **6**, and **10**) were found to recognize chloride in a non-cooperative independent manner.

MD simulations on transporters **1**-**10** in a POPC membrane model revealed that the molecules diffuse to the water/lipid interface, with all of them subsequently acquiring well-defined orientations, with the more lipophilic fluorinated aromatic ring found deeper in the membrane and the remaining aromatic rings closer to the water phase. While the thioureas' N−H binding motifs frequently point to the water phase, allowing for interactions with solvated anions, water molecules and phospholipid head groups, the acylhydrazone binding units present variable orientations, interacting with water molecules and with the phospholipids' phosphate and ester groups. Furthermore, it was possible to establish a relationship between the MM interaction energies of the different compounds and their transport activities. Typically, the poorest transporters also present the strongest interactions with the phospholipids, whereas the ones with moderate interaction MM energies with the POPC bilayer are among the best transporters. It was also demonstrated that the receptors **1**-**10** do not significantly impact the structural properties of the phospholipid bilayer.

From the constrained MD simulations, it was noticeable that the presence of the chloride in the complex shifted more water molecules to the membrane's core, pushing away the phospholipid tails and resulting in lower interaction energies than in the unconstrained simulations, although the same tendencies were observed. In the passive diffusion MD simulations of the chloride complexes, the orientation and hydrogen bond findings were in line with the results obtained in the passive diffusion MD simulations of the free receptors across POPC.

The free energy profiles of complexes **1** and **3** indicated that the larger size and secondary acylhydrazone binding site of the latter complex cause it to interact sooner with the phospholipids' head groups, in comparison to **1**, as well as a free energy minimum about 1 Å closer to the interface. Moreover, the better transporter (**1**) presented a slightly lower free energy barrier to overcome in order to cross the lipid tails to the opposite leaflet.

These *in silico* results strongly support the presented hypothesis, which proposes that the membrane interactions (both polar and apolar) of a moiety with a second anion binding site have negative effects on the transport activity of a thiourea derivative. It is also noticeable that, albeit less than the hydrogen bond donors, the second hydrogen bond acceptor groups have negative impacts on the transport activity. Furthermore, the commonly used logP values, along with anion binding constants or quantum descriptors, are not enough to assess the transport capability of a molecule, as they cannot predict its interaction with the membrane, given that both polar (such as acylhydrazones binding units – electrostatic interactions) and apolar groups (such as aromatic moieties – van der Waals interactions) contribute to the total interaction energy between the receptor and the membrane. Moreover, this work demonstrates that additional decorating and/or binding groups in synthetic anion transporters can greatly disturb their transport activity, which should be taken into consideration when designing new synthetic Channel Replacement Therapies that rely on the anion carrier mechanism.

Finally, the mechanisms behind chloride transport by transporters **1**-**10** were comprehensively studied, with the role of the acylhydrazone units properly clarified, it is safe to say that all the proposed objectives were successfully fulfilled.

IV.2. Future Work

All the work developed at the Molecular Modelling and Computational Biophysics Group resulted in the acquisition of crucial know-how, relating to the pioneering theoretical work that was reported on this dissertation and in the published article.[122]

The MD simulations methodologies and quantum descriptors used throughout this work can be employed in the future study of novel synthetic transporters. Indeed, new synthetic ion transporters can be idealised, having in consideration the drug design insights and experimental results obtained from this work, which states that additional binding units hinder the transport of anions if they are not cooperatively recognised. This multidisciplinary approach has once again proven to be adequate to tackle the rationalisation of the anion transport properties of a series of compounds.

References

1. Alberts, B.; Press, C. R. C., *Molecular biology of the cell*. 6th ed.; Garland Science: 2017.
2. Lodish, H. F., *Molecular cell biology*. 8th ed.; W.H. Freeman-Macmillan Learning: 2016.
3. Rhoades, R.; Bell, D. R.; Lippincott, W.; Wilkins, *Medical physiology : principles for clinical medicine*. 5th ed.; Wolters Kluwer Health/Lippincott Williams & Wilkins: Philadelphia, 2017.
4. Dodge, J. A.; Lewis, P. A.; Stanton, M.; Wilsher, J., Cystic fibrosis mortality and survival in the UK: 1947-2003. *Eur Respir J* **2007,** *29* (3), 522-6.
5. O'Sullivan, B. P.; Freedman, S. D., Cystic fibrosis. *The Lancet* **2009,** *373* (9678), 1891-1904.
6. *Cystic Fibrosis Foudation Patient Registry Annual Data Report*; 2019.
7. *European Cystic Fibrosis Society Patient Registry Annual Data Report* 2018.
8. Bell, S. C.; Mall, M. A.; Gutierrez, H.; Macek, M.; Madge, S.; Davies, J. C.; Burgel, P.-R.; Tullis, E.; Castaños, C.; Castellani, C.; Byrnes, C. A.; Cathcart, F.; Chotirmall, S. H.; Cosgriff, R.; Eichler, I.; Fajac, I.; Goss, C. H.; Drevinek, P.; Farrell, P. M.; Gravelle, A. M.; Havermans, T.; Mayer-Hamblett, N.; Kashirskaya, N.; Kerem, E.; Mathew, J. L.; McKone, E. F.; Naehrlich, L.; Nasr, S. Z.; Oates, G. R.; O'Neill, C.; Pypops, U.; Raraigh, K. S.; Rowe, S. M.; Southern, K. W.; Sivam, S.; Stephenson, A. L.; Zampoli, M.; Ratjen, F., The future of cystic fibrosis care: a global perspective. *The Lancet Respiratory Medicine* **2020,** *8* (1), 65-124.
9. Knowles, M. R.; Durie, P. R., What is cystic fibrosis? *N Engl J Med* **2002,** *347* (6), 439-42.
10. Amaral, M. D.; Kunzelmann, K., Molecular targeting of CFTR as a therapeutic approach to cystic fibrosis. *Trends Pharmacol Sci* **2007,** *28* (7), 334-41.
11. Planells-Cases, R.; Jentsch, T. J., Chloride channelopathies. *Biochim Biophys Acta* **2009,** *1792* (3), 173-89.
12. Christoph, R.; Michael, J. W., An Intrinsic Adenylate Kinase Activity Regulates Gating of the ABC Transporter CFTR. *Cell* **2003,** *115* (7), 837-850.
13. Csanády, L.; Vergani, P.; Gadsby, D. C., STRUCTURE, GATING, AND REGULATION OF THE CFTR ANION CHANNEL. *Physiol Rev* **2019,** *99* (1), 707-738.
14. Gentzsch, M.; Mall, M. A., Ion Channel Modulators in Cystic Fibrosis. *Chest* **2018,** *154* (2), 383-393.
15. Jih, K. Y.; Hwang, T. C., Vx-770 potentiates CFTR function by promoting decoupling between the gating cycle and ATP hydrolysis cycle. *Proc Natl Acad Sci U S A* **2013,** *110* (11), 4404-9.
16. Eckford, P. D.; Li, C.; Ramjeesingh, M.; Bear, C. E., Cystic fibrosis transmembrane conductance regulator (CFTR) potentiator VX-770 (ivacaftor) opens the defective channel gate of mutant CFTR in a phosphorylation-dependent but ATP-independent manner. *J Biol Chem* **2012,** *287* (44), 36639-49.
17. Davies, J. C.; Wainwright, C. E.; Canny, G. J.; Chilvers, M. A.; Howenstine, M. S.; Munck, A.; Mainz, J. G.; Rodriguez, S.; Li, H.; Yen, K.; Ordonez, C. L.; Ahrens, R.; Group, V. X. S., Efficacy and safety of ivacaftor in patients aged 6 to 11 years with cystic fibrosis with a G551D mutation. *Am J Respir Crit Care Med* **2013,** *187* (11), 1219-25.
18. Bessonova, L.; Volkova, N.; Higgins, M.; Bengtsson, L.; Tian, S.; Simard, C.; Konstan, M. W.; Sawicki, G. S.; Sewall, A.; Nyangoma, S.; Elbert, A.; Marshall, B. C.; Bilton, D., Data from the US and UK cystic fibrosis registries support disease modification by CFTR modulation with ivacaftor. *Thorax* **2018,** *73* (8), 731-740.
19. Flume, P. A.; Liou, T. G.; Borowitz, D. S.; Li, H.; Yen, K.; Ordonez, C. L.; Geller, D. E.; Group, V. X. S., Ivacaftor in subjects with cystic fibrosis who are homozygous for the F508del-CFTR mutation. *Chest* **2012,** *142* (3), 718-724.
20. Boyle, M. P.; Bell, S. C.; Konstan, M. W.; McColley, S. A.; Rowe, S. M.; Rietschel, E.; Huang, X.; Waltz, D.; Patel, N. R.; Rodman, D., A CFTR corrector (lumacaftor) and a CFTR potentiator (ivacaftor) for treatment of patients with cystic fibrosis who have a phe508del CFTR

mutation: a phase 2 randomised controlled trial. *The Lancet Respiratory Medicine* **2014,** *2* (7), 527-538.
21. Taylor-Cousar, J. L.; Munck, A.; McKone, E. F.; van der Ent, C. K.; Moeller, A.; Simard, C.; Wang, L. T.; Ingenito, E. P.; McKee, C.; Lu, Y.; Lekstrom-Himes, J.; Elborn, J. S., Tezacaftor-Ivacaftor in Patients with Cystic Fibrosis Homozygous for Phe508del. *N Engl J Med* **2017,** *377* (21), 2013-2023.
22. Mutyam, V.; Du, M.; Xue, X.; Keeling, K. M.; White, E. L.; Bostwick, J. R.; Rasmussen, L.; Liu, B.; Mazur, M.; Hong, J. S.; Falk Libby, E.; Liang, F.; Shang, H.; Mense, M.; Suto, M. J.; Bedwell, D. M.; Rowe, S. M., Discovery of Clinically Approved Agents That Promote Suppression of Cystic Fibrosis Transmembrane Conductance Regulator Nonsense Mutations. *Am J Respir Crit Care Med* **2016,** *194* (9), 1092-1103.
23. Davis, A. P.; Sheppard, D. N.; Smith, B. D., Development of synthetic membrane transporters for anions. *Chem. Soc. Rev.* **2007,** *36* (2), 348-57.
24. de Bolster, M. W. G., Glossary of terms used in bioinorganic chemistry (IUPAC Recommendations 1997). *Pure and Applied Chemistry* **1997,** *69* (6), 1251-1304.
25. Freedman, J. C., *Chapter 4 - Ionophores in Planar Lipid Bilayers*. Fourth Edition ed.; 2012; p 61-66.
26. Westley, J. W., Polyether Antibiotics: Versatile Carboxylic Acid Ionophores Produced by Streptomyces. *Advances in Applied Microbiology* **1977,** *22*, 177-223.
27. Vieira, P.; Miranda, M. Q.; Marques, I.; Carvalho, S.; Chen, L. J.; Howe, E. N. W.; Zhen, C.; Leung, C. Y.; Spooner, M. J.; Morgado, B.; da Cruz, E. S. O. A. B.; Moiteiro, C.; Gale, P. A.; Felix, V., Development of a Library of Thiophene-Based Drug-Like Lego Molecules: Evaluation of Their Anion Binding, Transport Properties, and Cytotoxicity. *Chemistry* **2020,** *26* (4), 888-899.
28. Davis, J. T.; Okunola, O.; Quesada, R., Recent advances in the transmembrane transport of anions. *Chemical Society Reviews* **2010,** *39* (10), 3843-3862.
29. Gokel, G. W.; Barkey, N., Transport of chloride ion through phospholipid bilayers mediated by synthetic ionophores. *New Journal of Chemistry* **2009,** *33* (5).
30. Gale, P. A., Anion receptor chemistry: highlights from 2008 and 2009. *Chemical Society Reviews* **2010,** *39* (10), 3746-3771.
31. Wenzel, M.; Light, M. E.; Davis, A. P.; Gale, P. A., Thiourea isosteres as anion receptors and transmembrane transporters. *Chem Commun (Camb)* **2011,** *47* (27), 7641-7643.
32. Wenzel, M.; Hiscock, J. R.; Gale, P. A., Anion receptor chemistry: highlights from 2010. *Chemical Society Reviews* **2012,** *41* (1), 480-520.
33. Gale, P. A.; Pérez-Tomás, R.; Quesada, R., Anion transporters and biological systems. *Acc Chem Res* **2013,** *46* (12), 2801-13.
34. Gale, P. A.; Busschaert, N.; Haynes, C. J. E.; Karagiannidis, L. E.; Kirby, I. L., Anion receptor chemistry: highlights from 2011 and 2012. *Chem. Soc. Rev.* **2014,** *43* (1), 205-241.
35. Busschaert, N.; Caltagirone, C.; Van Rossom, W.; Gale, P. A., Applications of Supramolecular Anion Recognition. *Chemical Reviews* **2015,** *115* (15), 8038-8155.
36. Gale, P. A.; Davis, J. T.; Quesada, R., Anion transport and supramolecular medicinal chemistry. *Chem Soc Rev* **2017,** *46* (9), 2497-2519.
37. Gale, P. A.; Howe, E. N. W.; Wu, X.; Spooner, M. J., Anion receptor chemistry: Highlights from 2016. *Coordination Chemistry Reviews* **2018,** *375*, 333-372.
38. Akhtar, N.; Biswas, O.; Manna, D., Biological applications of synthetic anion transporters. *Chemical Communications* **2020,** *56* (91), 14137-14153.
39. Chen, L.; Berry, S. N.; Wu, X.; Howe, E. N. W.; Gale, P. A., Advances in Anion Receptor Chemistry. *Chem* **2020,** *6* (1), 61-141.
40. Saha, T.; Gautam, A.; Mukherjee, A.; Lahiri, M.; Talukdar, P., Chloride Transport through Supramolecular Barrel-Rosette Ion Channels: Lipophilic Control and Apoptosis-Inducing Activity. *J Am Chem Soc* **2016,** *138* (50), 16443-16451.
41. Saha, P.; Madhavan, N., Macrocyclic Transmembrane Anion Transporters via a One-Pot Condensation Reaction. *Org Lett* **2020,** *22* (13), 5104-5108.

42. Gianotti, A.; Capurro, V.; Delpiano, L.; Mielczarek, M.; Garcia-Valverde, M.; Carreira-Barral, I.; Ludovico, A.; Fiore, M.; Baroni, D.; Moran, O.; Quesada, R.; Caci, E., Small Molecule Anion Carriers Correct Abnormal Airway Surface Liquid Properties in Cystic Fibrosis Airway Epithelia. *Int J Mol Sci* **2020,** *21* (4).
43. Bao, X.; Wu, X.; Berry, S. N.; Howe, E. N. W.; Chang, Y. T.; Gale, P. A., Fluorescent squaramides as anion receptors and transmembrane anion transporters. *Chem Commun (Camb)* **2018,** *54* (11), 1363-1366.
44. Marques, I.; Costa, P. M. R.; M, Q. M.; Busschaert, N.; Howe, E. N. W.; Clarke, H. J.; Haynes, C. J. E.; Kirby, I. L.; Rodilla, A. M.; Perez-Tomas, R.; Gale, P. A.; Felix, V., Full elucidation of the transmembrane anion transport mechanism of squaramides using in silico investigations. *Phys Chem Chem Phys* **2018,** *20* (32), 20796-20811.
45. Lang, C.; Mohite, A.; Deng, X.; Yang, F.; Dong, Z.; Xu, J.; Liu, J.; Keinan, E.; Reany, O., Semithiobambus[6]uril is a transmembrane anion transporter. *Chem Commun (Camb)* **2017,** *53* (54), 7557-7560.
46. McNally, B. A.; O'Neil, E. J.; Nguyen, A.; Smith, B. D., Membrane Transporters for Anions That Use a Relay Mechanism. *Journal of the American Chemical Society* **2008,** *130* (51), 17274-17275.
47. Wang, C.; Yang, H.; Xiang, Y.; Pang, S.; Bao, C.; Zhu, L., A Synthetic Phospholipid Derivative Mediates Ion Transport Across Lipid Bilayers. *Frontiers in Chemistry* **2021,** *9* (267).
48. Behr, J. P.; Kirch, M.; Lehn, J. M., Carrier-mediated transport through bulk liquid membranes: dependence of transport rates and selectivity on carrier properties in a diffusion-limited process. *Journal of the American Chemical Society* **2002,** *107* (1), 241-246.
49. Gokel, G. W.; Barkey, N., Transport of chloride ion through phospholipid bilayers mediated by synthetic ionophores. *New Journal of Chemistry* **2009,** *33* (5), 947-963.
50. Saggiomo, V.; Otto, S.; Marques, I.; Félix, V.; Torroba, T.; Quesada, R., The role of lipophilicity in transmembrane anion transport. *Chemical Communications* **2012,** *48* (43), 5274-5276.
51. Leach, A. R., *Molecular modelling : principles and applications*. 2nd ed.; 2009.
52. Jensen, F., *Introduction to Computational Chemistry*. John Wiley & Sons, Inc.: 2006.
53. Cramer, C. J., *Essentials of Computational Chemistry: Theories and Models*. Wiley, New York: 2002.
54. Feenstra, K. A.; Hess, B.; Berendsen, H. J., Improving efficiency of large time-scale molecular dynamics simulations of hydrogen-rich systems. *Journal of Computational Chemistry* **1999,** *20* (8), 786-798.
55. Jean-Paul, R.; Giovanni, C.; Herman, J. C. B., Numerical integration of the cartesian equations of motion of a system with constraints: molecular dynamics of n-alkanes. *Journal of Computational Physics* **1977,** *23* (3), 327-341.
56. Miyamoto, S.; Kollman, P. A., Settle: An analytical version of the SHAKE and RATTLE algorithm for rigid water models. *Journal of Computational Chemistry* **1992,** *13* (8), 952-962.
57. Hess, B.; Bekker, H.; Berendsen, H. J. C.; Fraaije, J. G. E. M., LINCS: A linear constraint solver for molecular simulations. *Journal of Computational Chemistry* **1997,** *18* (12), 1463-1472.
58. Wang, J.; Wolf, R. M.; Caldwell, J. W.; Kollman, P. A.; Case, D. A., Development and testing of a general amber force field. *Journal of Computational Chemistry* **2004,** *25* (9), 1157-1174.
59. Wang, J.; Wolf, R. M.; Caldwell, J. W.; Kollman, P. A.; Case, D. A., Development and testing of a general amber force field. *Journal of Computational Chemistry* **2005,** *26* (1), 114-114.
60. Wang, J., Development of the Second Generation of the General AMBER Force Field. 2017.
61. Singh, U. C.; Kollman, P. A., An approach to computing electrostatic charges for molecules. *Journal of Computational Chemistry* **1984,** *5* (2), 129-145.
62. Besler, B. H.; Merz Jr, K. M.; Kollman, P. A., Atomic charges derived from semiempirical methods. *Journal of Computational Chemistry* **1990,** *11* (4), 431-439.

63. Breneman, C. M.; Wiberg, K. B., Determining atom-centered monopoles from molecular electrostatic potentials. The need for high sampling density in formamide conformational analysis. *Journal of Computational Chemistry* **1990,** *11* (3), 361-373.
64. Bayly, C. I.; Cieplak, P.; Cornell, W.; Kollman, P. A., A well-behaved electrostatic potential based method using charge restraints for deriving atomic charges: the RESP model. *The Journal of Physical Chemistry* **1993,** *97* (40), 10269-10280.
65. Jakalian, A.; Bush, B. L.; Jack, D. B.; Bayly, C. I., Fast, efficient generation of high-quality atomic charges. AM1-BCC model: I. Method. *Journal of Computational Chemistry* **2000,** *21* (2), 132-146.
66. Jakalian, A.; Jack, D. B.; Bayly, C. I., Fast, efficient generation of high-quality atomic charges. AM1-BCC model: II. Parameterization and validation. *Journal of Computational Chemistry* **2002,** *23* (16), 1623-1641.
67. Chen, C.; Depa, P.; Maranas, J. K.; Garcia Sakai, V., Comparison of explicit atom, united atom, and coarse-grained simulations of poly (methyl methacrylate). *The Journal of Chemical Physics* **2008,** *128* (12), 124906.
68. Thomas, A. H.; Wolfgang, D., Polarizable force fields. *Current Opinion in Structural Biology* **2001,** *11* (2), 236-242.
69. Chowdhary, J.; Harder, E.; Lopes, P. E. M.; Huang, L.; Mackerell, A. D.; Roux, B., A Polarizable Force Field of Dipalmitoylphosphatidylcholine Based on the Classical Drude Model for Molecular Dynamics Simulations of Lipids. *The Journal of Physical Chemistry B* **2013,** *117* (31), 9142-9160.
70. Tsai, D., The virial theorem and stress calculation in molecular dynamics. *The Journal of Chemical Physics* **1979,** *70* (3), 1375-1382.
71. Andersen, H. C., Molecular dynamics simulations at constant pressure and/or temperature. *The Journal of Chemical Physics* **1980,** *72* (4), 2384-2393.
72. Bernardi, R. C.; Melo, M. C. R.; Schulten, K., Enhanced sampling techniques in molecular dynamics simulations of biological systems. *Biochim Biophys Acta* **2015,** *1850* (5), 872-877.
73. Kästner, J., Umbrella sampling. *Wiley Interdisciplinary Reviews: Computational Molecular Science* **2011,** *1* (6), 932-942.
74. Izrailev, S.; Stepaniants, S.; Isralewitz, B.; Kosztin, D.; Lu, H.; Molnar, F.; Wriggers, W.; Schulten, K., Steered molecular dynamics. In *Computational molecular dynamics: challenges, methods, ideas*, Springer: 1999; pp 39-65.
75. Barducci, A.; Bonomi, M.; Parrinello, M., Metadynamics. *Wiley Interdisciplinary Reviews: Computational Molecular Science* **2011,** *1* (5), 826-843.
76. Sugita, Y.; Okamoto, Y., Replica-exchange molecular dynamics method for protein folding. *Chemical physics letters* **1999,** *314* (1-2), 141-151.
77. Kumarasiri, M.; Baker, G. A.; Soudackov, A. V.; Hammes-Schiffer, S., Computational approach for ranking mutant enzymes according to catalytic reaction rates. *J Phys Chem B* **2009,** *113* (11), 3579-83.
78. Lee, T. S.; Radak, B. K.; Pabis, A.; York, D. M., A New Maximum Likelihood Approach for Free Energy Profile Construction from Molecular Simulations. *J Chem Theory Comput* **2013,** *9* (1), 153-164.
79. Giese, T. J.; Ekesan, S.; York, D. M., Extension of the Variational Free Energy Profile and Multistate Bennett Acceptance Ratio Methods for High-Dimensional Potential of Mean Force Profile Analysis. *J Phys Chem A* **2021,** *125* (19), 4216-4232.
80. Leonard, A. N.; Wang, E.; Monje-Galvan, V.; Klauda, J. B., Developing and Testing of Lipid Force Fields with Applications to Modeling Cellular Membranes. *Chemical Reviews* **2019,** *119* (9), 6227-6269.
81. Dickson, C. J.; Madej, B. D.; Skjevik, A. A.; Betz, R. M.; Teigen, K.; Gould, I. R.; Walker, R. C., Lipid14: The Amber Lipid Force Field. *Journal of Chemical Theory and Computation* **2014,** *10* (2), 865-879.
82. Klauda, J. B.; Venable, R. M.; Freites, J. A.; O'Connor, J. W.; Tobias, D. J.; Mondragon-Ramirez, C.; Vorobyov, I.; Mackerell, A. D.; Pastor, R. W., Update of the CHARMM

All-Atom Additive Force Field for Lipids: Validation on Six Lipid Types. *The Journal of Physical Chemistry B* **2010,** *114* (23), 7830-7843.
83. Dickson, C. J.; Rosso, L.; Betz, R. M.; Walker, R. C.; Gould, I. R., GAFFlipid: a General Amber Force Field for the accurate molecular dynamics simulation of phospholipid. *Soft Matter* **2012,** *8* (37), 9617-9627.
84. Jämbeck, J. P. M.; Lyubartsev, A. P., An Extension and Further Validation of an All-Atomistic Force Field for Biological Membranes. *Journal of Chemical Theory and Computation* **2012,** *8* (8), 2938-2948.
85. Jämbeck, J. P. M.; Lyubartsev, A. P., Another Piece of the Membrane Puzzle: Extending Slipids Further. *Journal of Chemical Theory and Computation* **2013,** *9* (1), 774-784.
86. Madej, B. D.; Gould, I. R.; Walker, R. C., A Parameterization of Cholesterol for Mixed Lipid Bilayer Simulation within the Amber Lipid14 Force Field. *The Journal of Physical Chemistry B* **2015,** *119* (38), 12424-12435.
87. Maciejewski, A.; Pasenkiewicz-Gierula, M.; Cramariuc, O.; Vattulainen, I.; Rog, T., Refined OPLS All-Atom Force Field for Saturated Phosphatidylcholine Bilayers at Full Hydration. *The Journal of Physical Chemistry B* **2014,** *118* (17), 4571-4581.
88. Kulig, W.; Pasenkiewicz-Gierula, M.; Róg, T., Topologies, structures and parameter files for lipid simulations in GROMACS with the OPLS-aa force field: DPPC, POPC, DOPC, PEPC, and cholesterol. *Data Brief* **2015,** *5*, 333-336.
89. Bhatnagar, N.; Kamath, G.; Potoff, J. J., Biomolecular Simulations with the Transferable Potentials for Phase Equilibria: Extension to Phospholipids. *The Journal of Physical Chemistry B* **2013,** *117* (34), 9910-9921.
90. Lee, S.; Tran, A.; Allsopp, M.; Lim, J. B.; Hénin, J.; Klauda, J. B., CHARMM36 United Atom Chain Model for Lipids and Surfactants. *The Journal of Physical Chemistry B* **2014,** *118* (2), 547-556.
91. Shinoda, W.; Devane, R.; Klein, M. L., Zwitterionic Lipid Assemblies: Molecular Dynamics Studies of Monolayers, Bilayers, and Vesicles Using a New Coarse Grain Force Field. *The Journal of Physical Chemistry B* **2010,** *114* (20), 6836-6849.
92. Arnarez, C.; Uusitalo, J. J.; Masman, M. F.; Ingólfsson, H. I.; De Jong, D. H.; Melo, M. N.; Periole, X.; De Vries, A. H.; Marrink, S. J., Dry Martini, a Coarse-Grained Force Field for Lipid Membrane Simulations with Implicit Solvent. *Journal of Chemical Theory and Computation* **2015,** *11* (1), 260-275.
93. Jójárt, B.; Martinek, T. A., Performance of the general amber force field in modeling aqueous POPC membrane bilayers. *J Comput Chem* **2007,** *28* (12), 2051-8.
94. Skjevik, Å. A.; Madej, B. D.; Dickson, C. J.; Lin, C.; Teigen, K.; Walker, R. C.; Gould, I. R., Simulation of lipid bilayer self-assembly using all-atom lipid force fields. *Physical Chemistry Chemical Physics* **2016,** *18* (15), 10573-10584.
95. Gould, I.; Skjevik, A.; Dickson, C.; Madej, B.; Walker, R., Lipid17: A comprehensive AMBER force field for the simulation of zwitterionic and anionic lipids. *Manuscript in preparation* **2018**.
96. Song, L. F.; Lee, T.-S.; Zhu, C.; York, D. M.; Merz, K. M., Using AMBER18 for Relative Free Energy Calculations. *Journal of Chemical Information and Modeling* **2019,** *59* (7), 3128-3135.
97. Salomon-Ferrer, R.; Case, D. A.; Walker, R. C., An overview of the Amber biomolecular simulation package. *WIREs Computational Molecular Science* **2013,** *3* (2), 198-210.
98. D.A. Case, H.M. Aktulga, K. Belfon, I.Y. Ben-Shalom, S.R. Brozell, D.S. Cerutti, T.E. Cheatham, III, G.A. Cisneros, V.W.D. Cruzeiro, T.A. Darden, R.E. Duke, G. Giambasu, M.K. Gilson, H. Gohlke, A.W. Goetz, R. Harris, S. Izadi, S.A. Izmailov, C. Jin, K. Kasavajhala, M.C. Kaymak, E. King, A. Kovalenko, T. Kurtzman, T.S. Lee, S. LeGrand, P. Li, C. Lin, J. Liu, T. Luchko, R. Luo, M. Machado, V. Man, M. Manathunga, K.M. Merz, Y. Miao, O. Mikhailovskii, G. Monard, H. Nguyen, K.A. O'Hearn, A. Onufriev, F. Pan, S. Pantano, R. Qi, A. Rahnamoun, D.R. Roe, A. Roitberg, C. Sagui, S. Schott-Verdugo, J. Shen, C.L. Simmerling, N.R. Skrynnikov,

J. Smith, J. Swails, R.C. Walker, J. Wang, H. Wei, R.M. Wolf, X. Wu, Y. Xue, D.M. York, S. Zhao, and P.A. Kollman (**2021**), Amber 2021, University of California, San Francisco.
99. Salomon-Ferrer, R.; Götz, A. W.; Poole, D.; Le Grand, S.; Walker, R. C., Routine Microsecond Molecular Dynamics Simulations with AMBER on GPUs. 2. Explicit Solvent Particle Mesh Ewald. *Journal of Chemical Theory and Computation* **2013,** *9* (9), 3878-3888.
100. Le Grand, S.; Götz, A. W.; Walker, R. C., SPFP: Speed without compromise—A mixed precision model for GPU accelerated molecular dynamics simulations. *Comput. Phys. Commun.* **2013,** *184* (2), 374-380.
101. Zheng, S. P.; Huang, L. B.; Sun, Z.; Barboiu, M., Self-Assembled Artificial Ion-Channels toward Natural Selection of Functions. *Angew Chem Int Ed Engl* **2021,** *60* (2), 566-597.
102. Busschaert, N.; Kirby, I. L.; Young, S.; Coles, S. J.; Horton, P. N.; Light, M. E.; Gale, P. A., Squaramides as potent transmembrane anion transporters. *Angew Chem Int Ed Engl* **2012,** *51* (18), 4426-30.
103. Spooner, M. J.; Gale, P. A., Anion transport across varying lipid membranes--the effect of lipophilicity. *Chem Commun (Camb)* **2015,** *51* (23), 4883-6.
104. Valkenier, H.; Haynes, C. J. E.; Herniman, J.; Gale, P. A.; Davis, A. P., Lipophilic balance – a new design principle for transmembrane anion carriers. *Chemical Science* **2014,** *5* (3).
105. Saggiomo, V.; Otto, S.; Marques, I.; Felix, V.; Torroba, T.; Quesada, R., The role of lipophilicity in transmembrane anion transport. *Chem Commun (Camb)* **2012,** *48* (43), 5274-6.
106. Wu, X.; Small, J. R.; Cataldo, A.; Withecombe, A. M.; Turner, P.; Gale, P. A., Voltage-Switchable HCl Transport Enabled by Lipid Headgroup-Transporter Interactions. *Angew Chem Int Ed Engl* **2019,** *58* (42), 15142-15147.
107. Dias, C. M.; Valkenier, H.; Davis, A. P., Anthracene Bisureas as Powerful and Accessible Anion Carriers. *Chemistry* **2018,** *24* (23), 6262-6268.
108. Valkenier, H.; Judd, L. W.; Li, H.; Hussain, S.; Sheppard, D. N.; Davis, A. P., Preorganized bis-thioureas as powerful anion carriers: chloride transport by single molecules in large unilamellar vesicles. *J Am Chem Soc* **2014,** *136* (35), 12507-12.
109. Ko, S. K.; Kim, S. K.; Share, A.; Lynch, V. M.; Park, J.; Namkung, W.; Van Rossom, W.; Busschaert, N.; Gale, P. A.; Sessler, J. L.; Shin, I., Synthetic ion transporters can induce apoptosis by facilitating chloride anion transport into cells. *Nat Chem* **2014,** *6* (10), 885-92.
110. Iglesias Hernandez, P.; Moreno, D.; Javier, A. A.; Torroba, T.; Perez-Tomas, R.; Quesada, R., Tambjamine alkaloids and related synthetic analogs: efficient transmembrane anion transporters. *Chem Commun (Camb)* **2012,** *48* (10), 1556-8.
111. Picci, G.; Carreira-Barral, I.; Alonso-Carrillo, D.; Sanz-González, D.; Fernández-López, P.; García-Valverde, M.; Caltagirone, C.; Quesada, R., Simple isophthalamides/dipicolineamides as active transmembrane anion transporters. *Supramolecular Chemistry* **2019,** *32* (2), 112-118.
112. Bak, K. M.; Chabuda, K.; Montes, H.; Quesada, R.; Chmielewski, M. J., 1,8-Diamidocarbazoles: an easily tuneable family of fluorescent anion sensors and transporters. *Org Biomol Chem* **2018,** *16* (28), 5188-5196.
113. Shinde, S. V.; Talukdar, P., An anion receptor that facilitates transmembrane proton-anion symport by deprotonating its sulfonamide N-H proton. *Chem Commun (Camb)* **2018,** *54* (73), 10351-10354.
114. Li, J.; Nowak, P.; Otto, S., Dynamic combinatorial libraries: from exploring molecular recognition to systems chemistry. *J Am Chem Soc* **2013,** *135* (25), 9222-39.
115. Beeren, S. R.; Sanders, J. K., Discovery of linear receptors for multiple dihydrogen phosphate ions using dynamic combinatorial chemistry. *J Am Chem Soc* **2011,** *133* (11), 3804-7.
116. Corbett, P. T.; Leclaire, J.; Vial, L.; West, K. R.; Wietor, J. L.; Sanders, J. K.; Otto, S., Dynamic combinatorial chemistry. *Chem Rev* **2006,** *106* (9), 3652-711.
117. Vantomme, G.; Jiang, S.; Lehn, J. M., Adaptation in constitutional dynamic libraries and networks, switching between orthogonal metalloselection and photoselection processes. *J Am Chem Soc* **2014,** *136* (26), 9509-18.
118. Kokan, Z.; Chmielewski, M. J., A Photoswitchable Heteroditopic Ion-Pair Receptor. *J Am Chem Soc* **2018,** *140* (47), 16010-16014.

119. Shao, B.; Aprahamian, I., Hydrazones as New Molecular Tools. *Chem* **2020,** *6* (9), 2162-2173.
120. Howe, E. N.; Busschaert, N.; Wu, X.; Berry, S. N.; Ho, J.; Light, M. E.; Czech, D. D.; Klein, H. A.; Kitchen, J. A.; Gale, P. A., pH-Regulated Nonelectrogenic Anion Transport by Phenylthiosemicarbazones. *J Am Chem Soc* **2016,** *138* (26), 8301-8.
121. Martínez-Crespo, L.; Halgreen, L.; Soares, M.; Marques, I.; Félix, V.; Valkenier, H., Hydrazones in anion transporters: The detrimental effect of a second binding site. *Organic and Biomolecular Chemistry* **2021**.
122. Martinez-Crespo, L.; Halgreen, L.; Soares, M.; Marques, I.; Felix, V.; Valkenier, H., Hydrazones in anion transporters: the detrimental effect of a second binding site. *Org Biomol Chem* **2021**.
123. Groom, C. R.; Bruno, I. J.; Lightfoot, M. P.; Ward, S. C., The Cambridge Structural Database. *Acta Crystallographica Section B* **2016,** *72* (2), 171-179.
124. Frisch, M. J.; Trucks, G. W.; Schlegel, H. B.; Scuseria, G. E.; Robb, M. A.; Cheeseman, J. R.; Scalmani, G.; Barone, V.; Petersson, G. A.; Nakatsuji, H.; Li, X.; Caricato, M.; Marenich, A. V.; Bloino, J.; Janesko, B. G.; Gomperts, R.; Mennucci, B.; Hratchian, H. P.; Ortiz, J. V.; Izmaylov, A. F.; Sonnenberg, J. L.; Williams; Ding, F.; Lipparini, F.; Egidi, F.; Goings, J.; Peng, B.; Petrone, A.; Henderson, T.; Ranasinghe, D.; Zakrzewski, V. G.; Gao, J.; Rega, N.; Zheng, G.; Liang, W.; Hada, M.; Ehara, M.; Toyota, K.; Fukuda, R.; Hasegawa, J.; Ishida, M.; Nakajima, T.; Honda, Y.; Kitao, O.; Nakai, H.; Vreven, T.; Throssell, K.; Montgomery Jr., J. A.; Peralta, J. E.; Ogliaro, F.; Bearpark, M. J.; Heyd, J. J.; Brothers, E. N.; Kudin, K. N.; Staroverov, V. N.; Keith, T. A.; Kobayashi, R.; Normand, J.; Raghavachari, K.; Rendell, A. P.; Burant, J. C.; Iyengar, S. S.; Tomasi, J.; Cossi, M.; Millam, J. M.; Klene, M.; Adamo, C.; Cammi, R.; Ochterski, J. W.; Martin, R. L.; Morokuma, K.; Farkas, O.; Foresman, J. B.; Fox, D. J. *Gaussian 16 Rev. C.01*, Wallingford, CT, 2016.
125. Grimme, S.; Antony, J.; Ehrlich, S.; Krieg, H., A consistent and accurate ab initio parametrization of density functional dispersion correction (DFT-D) for the 94 elements H-Pu. *J Chem Phys* **2010,** *132* (15), 154104.
126. Barone, V.; Cossi, M., Quantum Calculation of Molecular Energies and Energy Gradients in Solution by a Conductor Solvent Model. *The Journal of Physical Chemistry A* **1998,** *102* (11), 1995-2001.
127. Cossi, M.; Rega, N.; Scalmani, G.; Barone, V., Energies, structures, and electronic properties of molecules in solution with the C-PCM solvation model. *J Comput Chem* **2003,** *24* (6), 669-81.
128. Lu, T.; Chen, F., Multiwfn: A multifunctional wavefunction analyzer. *Journal of Computational Chemistry* **2012,** *33* (5), 580-592.
129. Bader, R. F., Atoms in molecules. *Accounts of Chemical Research* **1985,** *18* (1), 9-15.
130. Weinhold, F., Natural bond critical point analysis: Quantitative relationships between natural bond orbital-based and QTAIM-based topological descriptors of chemical bonding. *Journal of Computational Chemistry* **2012,** *33* (30), 2440-2449.
131. Glendening, E. D.; Landis, C. R.; Weinhold, F., Natural bond orbital methods. *WIREs Computational Molecular Science* **2012,** *2* (1), 1-42.
132. Glendening, E. D.; Landis, C. R.; Weinhold, F., NBO 6.0: natural bond orbital analysis program. *J Comput Chem* **2013,** *34* (16), 1429-37.
133. Reed, A. E.; Curtiss, L. A.; Weinhold, F., Intermolecular interactions from a natural bond orbital, donor-acceptor viewpoint. *Chemical Reviews* **1988,** *88* (6), 899-926.
134. Wang, J.; Wang, W.; Kollman, P. A.; Case, D. A., Automatic atom type and bond type perception in molecular mechanical calculations. *J Mol Graph Model* **2006,** *25* (2), 247-60.
135. Xue, M.; Liu, S.-X., 2',2'-Dibenzylideneisophthalohydrazide methanol solvate. *Acta Crystallographica Section E* **2006,** *62* (2), o759-o761.
136. Taha, M.; Baharudin, M. S.; Zaki, H. M.; Yamin, B. M.; Naz, H., Crystal structure of (E)-N'-benzylidene-2-methoxybenzohydrazide. *Acta Crystallographica Section E* **2014,** *70* (9), o1071-o1072.

137. Li, X.; Qiao, J.; Chee, S. W.; Xu, H.-S.; Zhao, X.; Choi, H. S.; Yu, W.; Quek, S. Y.; Mirsaidov, U.; Loh, K. P., Rapid, Scalable Construction of Highly Crystalline Acylhydrazone Two-Dimensional Covalent Organic Frameworks via Dipole-Induced Antiparallel Stacking. *Journal of the American Chemical Society* **2020,** *142* (10), 4932-4943.
138. Rodrigues, R. F. N.; Almeida, L. R.; Santos, F. G. d.; Carvalho, P. S., Jr.; Souza, W. C. d.; Moreira, K. S.; Aquino, G. L. B. d.; Valverde, C.; Napolitano, H. B.; Baseia, B., Solid state characterization and theoretical study of non-linear optical properties of a Fluoro-N-Acylhydrazide derivative. *PLOS ONE* **2017,** *12* (4), e0175859.
139. Kümmerle, A. E.; Raimundo, J. M.; Leal, C. M.; da Silva, G. S.; Balliano, T. L.; Pereira, M. A.; de Simone, C. A.; Sudo, R. T.; Zapata-Sudo, G.; Fraga, C. A. M.; Barreiro, E. J., Studies towards the identification of putative bioactive conformation of potent vasodilator arylidene N-acylhydrazone derivatives. *European Journal of Medicinal Chemistry* **2009,** *44* (10), 4004-4009.
140. Tributino, J. L. M.; Duarte, C. D.; Corrêa, R. S.; Doriguetto, A. C.; Ellena, J.; Romeiro, N. C.; Castro, N. G.; Miranda, A. L. P.; Barreiro, E. J.; Fraga, C. A. M., Novel 6-methanesulfonamide-3,4-methylenedioxyphenyl-N-acylhydrazones: Orally effective anti-inflammatory drug candidates. *Bioorganic & Medicinal Chemistry* **2009,** *17* (3), 1125-1131.
141. Muthukumar, P.; Surya, M.; Pannipara, M.; Al-Sehemi, A. G.; Moon, D.; Philip Anthony, S., Easily Accessible Schiff Base ESIPT Molecules with Tunable Solid State Fluorescence: Mechanofluorochromism and Highly Selective Co2+ Fluorescence Sensing. *ChemistrySelect* **2020,** *5* (11), 3295-3302.
142. Li, Y.; Huang, W.; Yong, J.; Huang, S.; Li, Y.; Liu, Y.; Wu, D., Aggregation-induced ratiometric emission and mechanochromic luminescence in a pyrene-benzohydrazonate conjugate. *New Journal of Chemistry* **2018,** *42* (15), 12644-12648.
143. Martínez, L.; Andrade, R.; Birgin, E. G.; Martínez, J. M., PACKMOL: a package for building initial configurations for molecular dynamics simulations. *J Comput Chem* **2009,** *30* (13), 2157-64.
144. Jorgensen, W. L.; Chandrasekhar, J.; Madura, J. D.; Impey, R. W.; Klein, M. L., Comparison of simple potential functions for simulating liquid water. *The Journal of Chemical Physics* **1983,** *79* (2), 926-935.
145. Li, P.; Song, L. F.; Merz, K. M., Systematic Parameterization of Monovalent Ions Employing the Nonbonded Model. *Journal of Chemical Theory and Computation* **2015,** *11* (4), 1645-1657.
146. Darden, T.; York, D.; Pedersen, L., Particle mesh Ewald: An N·log(N) method for Ewald sums in large systems. *The Journal of Chemical Physics* **1993,** *98* (12), 10089-10092.
147. Loncharich, R. J.; Brooks, B. R.; Pastor, R. W., Langevin dynamics of peptides: the frictional dependence of isomerization rates of N-acetylalanyl-N'-methylamide. *Biopolymers* **1992,** *32* (5), 523-35.
148. Berendsen, H. J. C.; Postma, J. P. M.; Gunsteren, W. F. v.; DiNola, A.; Haak, J. R., Molecular dynamics with coupling to an external bath. *The Journal of Chemical Physics* **1984,** *81* (8), 3684-3690.
149. Ryckaert, J.-P.; Ciccotti, G.; Berendsen, H. J. C., Numerical integration of the cartesian equations of motion of a system with constraints: molecular dynamics of n-alkanes. *Journal of Computational Physics* **1977,** *23* (3), 327-341.
150. Roe, D. R.; Cheatham, T. E., 3rd, PTRAJ and CPPTRAJ: Software for Processing and Analysis of Molecular Dynamics Trajectory Data. *J Chem Theory Comput* **2013,** *9* (7), 3084-95.

Appendix

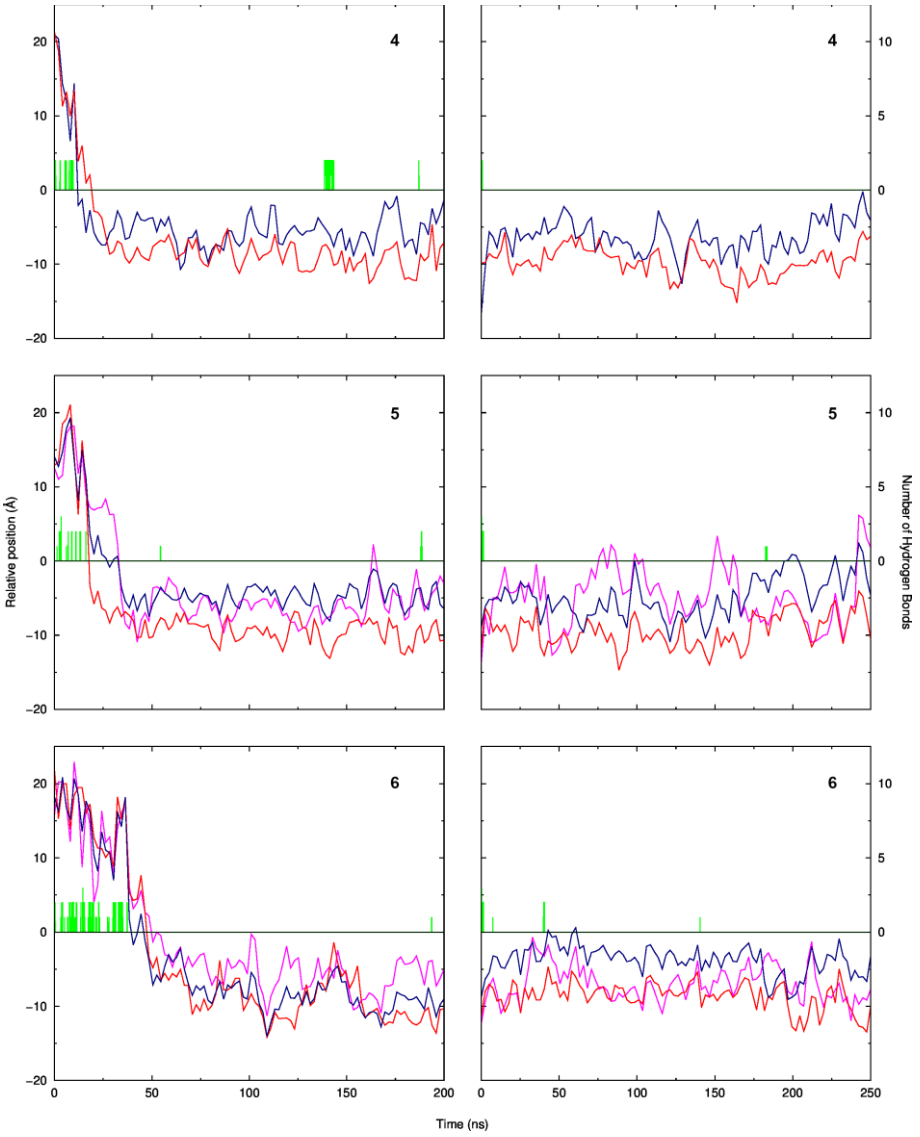

Figure A1. Evolution of the relative position of the **A**, **B** and **C** (red, blue and magenta lines, respectively) reference points in illustrative MD runs in the ***𝒜*** (left) and ***ℬ*** (right) scenarios. Remaining details are given in **Figure III-3**.

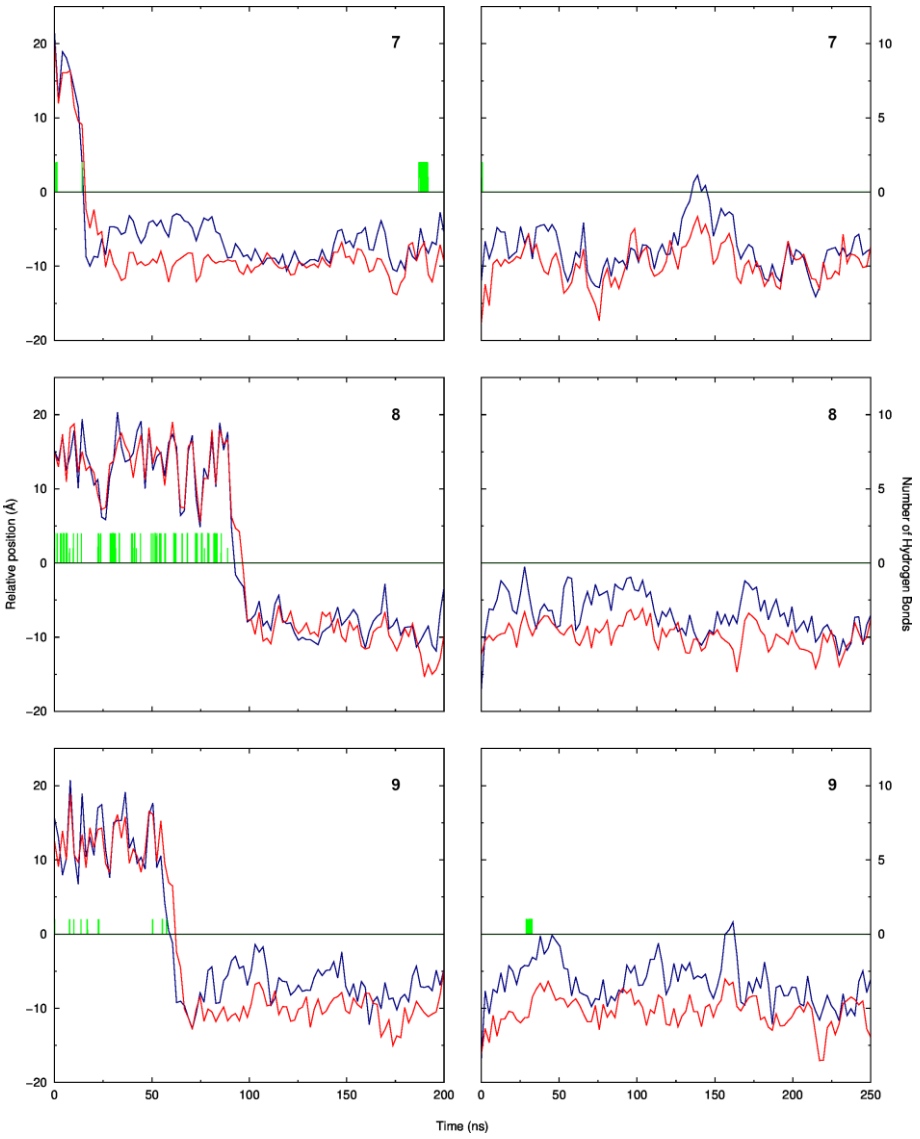

Figure A2. Evolution of the relative position of the **A**, and **B** (red and blue lines, respectively) reference points in illustrative MD runs in the ***𝒜*** (left) and ***ℬ*** (right) scenarios. Remaining details are given in **Figure III-3**.

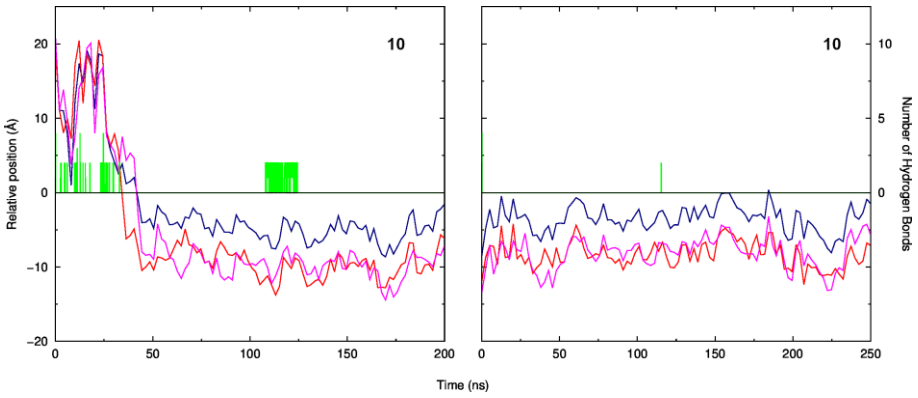

Figure A3. Evolution of the relative position of the **A**, **B** and **C** (red, blue and magenta lines, respectively) reference points in illustrative MD runs in the ***𝒜*** (left) and ***ℬ*** (right) scenarios. Remaining details are given in **Figure III-3**.

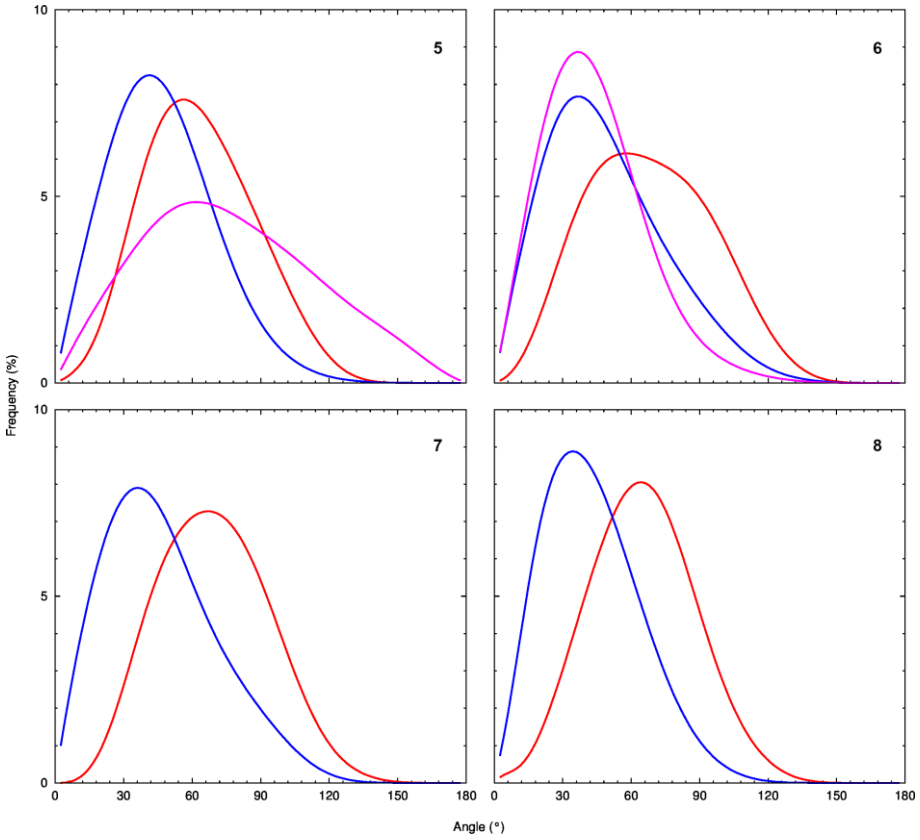

Figure A4. Frequency profiles assessed during the sampling period of the MD simulations of **5**-**8**. Remaining details are given in **Figure III-4**.

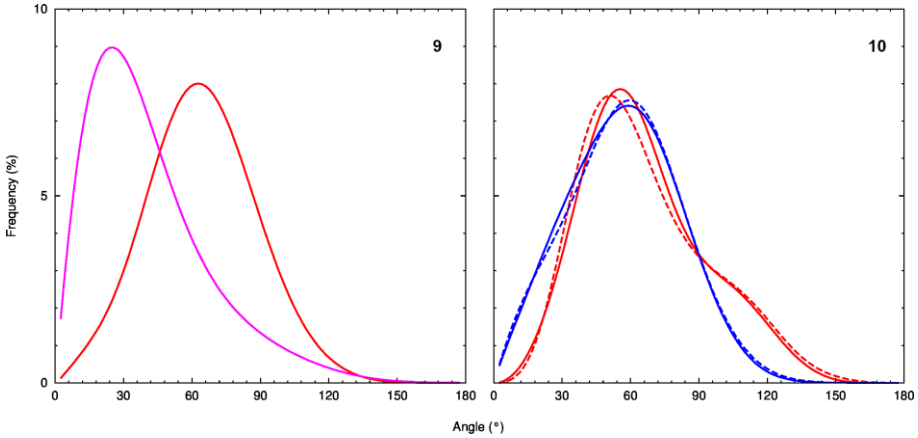

Figure A5. Frequency profiles assessed during the sampling period of the MD simulations of **9** and **10** (solid lines for a 3,5-bis(trifluoromethyl)phenyl thiourea moiety and dashed lines for the other one). Remaining details are given in **Figure III-4**.

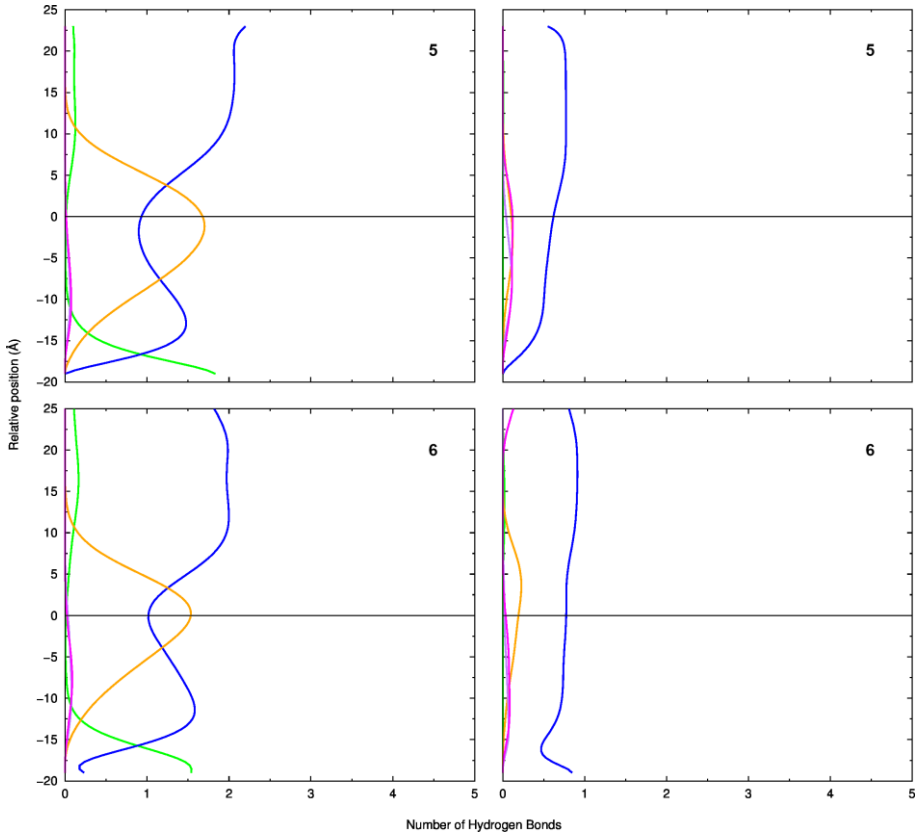

Figure A6. Average number of thiourea (left) and acylhydrazone (right) hydrogen bonds vs. the relative position of the centre of mass of **5** and **6**. Remaining details are given in **Figure III-5**.

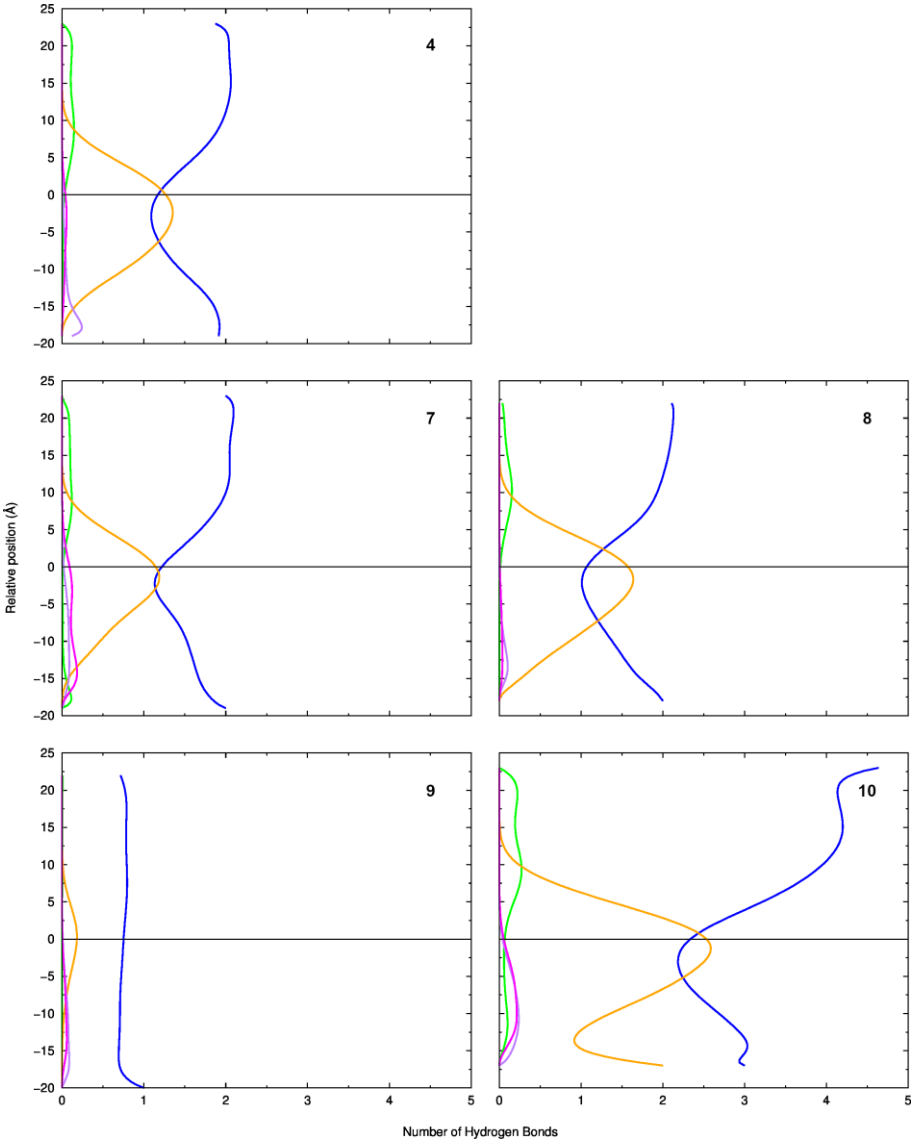

Figure A7. Average number of thiourea hydrogen bonds vs. the relative position of the centre of mass of **4**, **7**, **8**, **9** (acylhydrazone motif), and **10**. Remaining details are given in **Figure III-5**.

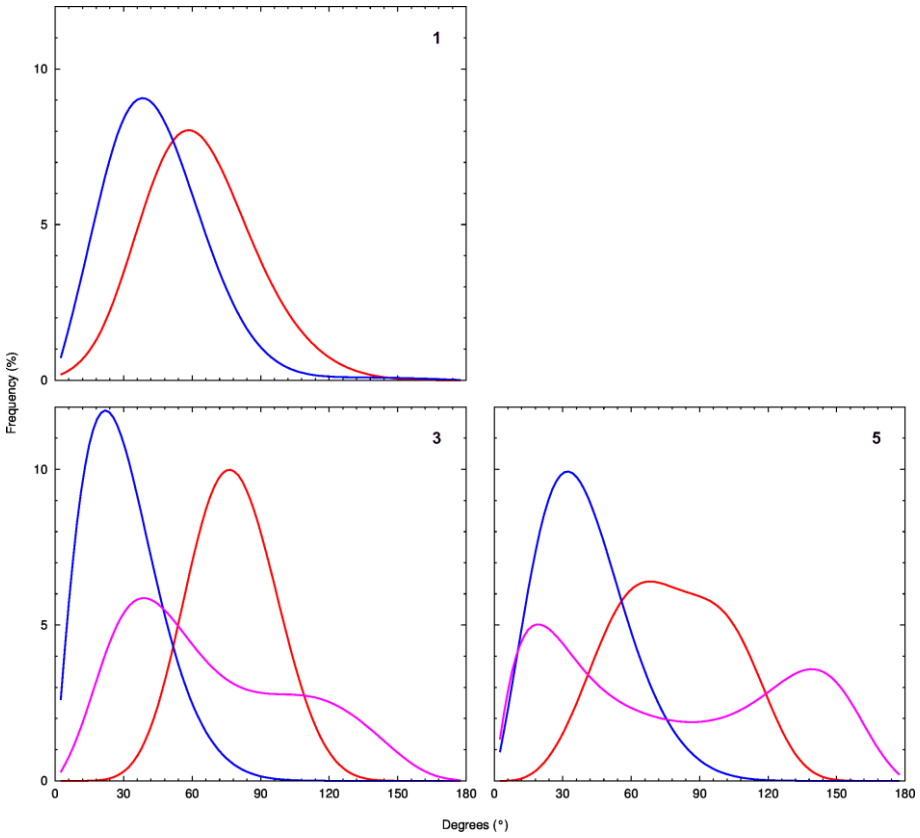

Figure A8. Frequency profiles assessed during the sampling period of the constrained MD simulations of **1**, **3**, and **5**. Remaining details are given in **Figure III-4**.